

**NEW APPROACHES TO INTERFACE RENEWABLE ENERGY SYSTEMS TO  
ELECTRIC UTILITY VIA HIGHER FREQUENCY TRANSFORMER  
ISOLATION**

A Dissertation

by

**SALWAN SAMIR SABRY**

Submitted to the Office of Graduate and Professional Studies of  
Texas A&M University  
in partial fulfillment of the requirements for the degree of

**DOCTOR OF PHILOSOPHY**

Chair of Committee,	Prasad N. Enjeti
Committee Members,	Shankar P. Bhattacharyya
	Chanan Singh
	Parabir Daripa
Head of Department,	Miroslav M. Begovic

August 2020

Major Subject: Electrical Engineering

Copyright 2020 Salwan Samir Sabry

## **ABSTRACT**

In this dissertation, several new approaches to interface the renewable energy resources to a utility grid are explored. It is shown a DC collection grid is preferred due to its simplicity, low cost in terms of structure and low losses.

In the first study, a medium voltage DC collection grid photovoltaic PV power plant using 12-pulse SCR converter and line frequency phase-shift transformer is presented. The proposed concept includes a new hybrid step-up DC-DC converter to boost the PV plant voltage to the medium voltage scale. The features of this topology are simple, bidirectional power flow, and reliable due to the absence of the DC link capacitor. The key point to improve the power density of power electronics converters is to minimize the magnetic elements inductor/transformer, and eliminate DC link capacitor if it is possible.

Responding to this key point, the second study proposes a medium voltage DC collection grid for large-scale PV power plant using 12-pulse SCR converter and employing an integrated medium frequency (720 Hz) solid-state transformer. The advantages of this topology are simple, easy to control, higher power density, eliminating the need of DC link capacitor, and bidirectional power flow capability.

To improve the reliability, efficiency and power density for the second study further, an open delta phase-shift medium frequency solid-state transformer is proposed. The analysis and simulation results show that the open delta concept has the same quality performance as the second approach.

In the final study, a tractive bidirectional power flow current source converter using selective harmonics elimination SHE pulse width modulation PWM technique is proposed. This approach is employing a high frequency (20 kHz) integrated solid-state transformer for galvanic isolation. The analysis shows a very good input current quality by removing the low order harmonics e.g. (5<sup>th</sup>, 7<sup>th</sup>, 11<sup>th</sup>, 13<sup>th</sup>). Bidirectional power flow is allowable to use this approach for either renewable energy harvesting or electrical vehicle EV charging system.

In general, the results of this dissertation show that the presented topologies have beneficial features in terms of bidirectional power flow, simplicity, high reliability, good input current quality, and high power density compared to the conventional approaches.

## DEDICATION

بسم الله الرحمن الرحيم

الى

امى الغالية

ابى

زوجتى

اولادى

*In the Name of God, Most Merciful*

*To*

*My Mother*

*My Dad*

*My Wife*

*My Kids*

## **ACKNOWLEDGEMENTS**

I would like to express my sincere gratitude to my advisor Prof. Prasad N. Enjeti, for the continuous and valuable support of my Ph.D. study. I want to thank him for his patience, motivation, and immense knowledge. His guidance helped me in every aspect of my research. I cannot find enough words to thank him for the valuable mentorship and support.

Besides my advisor, I would like to thank my committee members Prof. Shankar P. Bhattacharyya, Prof. Chanan Singh, and Prof. Parabir Daripa, for their time and guidance. Their technical feedback and recommendations improved my work outcome.

I would like to extend my thanks to Texas A&M ECEN department, especially John Tyler, Katharine Bryan, Melissa Sheldon, and Annie Bruner for their valuable support.

I want to express my heartfelt thanks to my colleagues and friends at the PQ Lab team members.

Last but not least, I would like to gift every single accomplishment to my God, my parents, my wife, and my kids who gave me unconditional love and support to be the person I am today.

## **CONTRIBUTORS AND FUNDING SOURCES**

The work in this dissertation was supervised by the dissertation committee, including Dr. Prasad Enjeti, Dr. Shankar P. Bhattacharyya, and Dr. Chanan Singh from the Electrical and Computer Engineering Department, and Dr. Parabir Daripa from the Mathematics Department.

My graduate studies were funded by the Iraqi Ministry of Higher Education and Scientific Research. I also had the opportunity to fund my graduate studies through a teaching assistantship. I would like to thank Dr. John Tyler for giving me this opportunity to work for his principles of electrical engineering course for non-major students. The last semester of my graduate studies was supported by my advisor, Dr. Enjeti.

## TABLE OF CONTENTS

	Page
ABSTRACT .....	ii
DEDICATION .....	iv
ACKNOWLEDGEMENTS .....	v
CONTRIBUTORS AND FUNDING SOURCES.....	vi
TABLE OF CONTENTS .....	vii
LIST OF FIGURES.....	x
LIST OF TABLES .....	xviii
1. INTRODUCTION.....	1
1.1. High Power Switching Devices.....	1
1.1.1. Silicon Control Rectifier SCR.....	2
1.2. Introduction to AC and DC Collection Grid .....	4
1.3. Large Scale PV Plant.....	7
1.4. Power Density .....	8
1.5. Research Objective.....	12
1.6. Dissertation Outline.....	14
2. MEDIUM VOLTAGE DC COLLECTION GRID CONCEPT FOR LARGE- SCALE PV POWER PLANT USING MULTI-PULSE LINE FREQUENCY SCR CONVERTER AND HYBRID STEP-UP DC-DC CONVERTER.....	16
2.1. Introduction .....	16
2.2. Proposed Medium Voltage DC Collection Grid for Large-Scale PV Power Plant Using Multi-Pulse SCR Converter and Hybrid Step-up DC-DC Converter.....	18
2.2.1. Proposed Hybrid Step-up DC-DC Converter .....	18
2.2.2. 12-pulse SCR Converter.....	30
2.2.3. Phase-Shift Line Frequency (50/60) Hz Transformer .....	30
2.3. Simulation Results for the Proposed Topology .....	31
2.4. Conclusion.....	37

3. MEDIUM VOLTAGE DC COLLECTION GRID FOR LARGE-SCALE PV POWER PLANT WITH SCR CONVERTER AND INTEGRATED MEDIUM FREQUENCY SOLID-STATE TRANSFORMER (SST) FOR UTILITY INTERFACE .....	38
3.1. Introduction .....	39
3.2. Proposed Medium Voltage DC Collection Grid for Large-Scale PV Power Plant with SCR Converter and Medium Frequency Solid-State Transformer .....	40
3.2.1. Bidirectional AC-AC Converter.....	40
3.2.2. Medium Frequency Zig-Zag Phase-Shift Transformer .....	45
3.2.3. 12-pulse SCR Converter.....	47
3.3. Input Current Analysis .....	48
3.4. Design Example .....	52
3.5. Simulation Results.....	56
3.5.1. Semiconductors Power Losses Evaluation.....	57
3.6. Experimental Results.....	62
3.7. Open Delta Scheme for 12-Pulse SCR Converter with Medium Frequency Integrated Solid-State Transformer.....	72
3.7.1. Open Delta Phase-Shift Transformer Phasor Diagram .....	72
3.7.2. Open Delta Simulation Results .....	75
3.8. Conclusion.....	80
4. HIGH FREQUENCY INTEGRATED SOLID-STATE TRANSFORMER (SST) FOR UTILITY INTERFACE OF SOLAR PV / BATTERY ENERGY STORAGE SYSTEMS .....	82
4.1. Introduction .....	83
4.2. Selective Harmonics Elimination Pulse Width Modulation SHE PWM .....	87
4.3. Proposed High Frequency Integrated Solid-State Transformer with Selective Harmonics Elimination Technique for Utility Interface .....	91
4.3.1. Bidirectional AC-AC Converter.....	91
4.3.2. High Frequency Transformer .....	94
4.3.3. Three Phase Current Source Converter CSC Using Selective Harmonics Elimination SHE Pulse Width Modulation PWM.....	95
4.4. Input Current Analysis .....	100
4.5. Design Example .....	103
4.6. Simulation Results.....	104
4.7. Experimental Results.....	112
4.8. Conclusion.....	118
5. SUMMARY .....	120
5.1. Conclusion.....	120
5.2. Future Works.....	122



REFERENCES.....	124
-----------------	-----

## LIST OF FIGURES

	Page
Figure 1-1 Semiconductor power devices ratings versus switching frequency and their applications.....	1
Figure 1-2 High power semiconductor devices (a) SCR, (b) Diode, (c) SCR's characteristics, (d) diode's characteristics. ....	4
Figure 1-3 SCR turn on and turn off switching characteristics.....	5
Figure 1-4 Schematic diagram of large-scale PV power plant. (a) AC collection grid, (b) DC collection Grid.....	6
Figure 1-5 Price unit/ MWh for both wind and solar according to Lazard Levelized cos of energy analysis. Reprinted from [15].....	7
Figure 1-6 Utility scale PV plant in Arizona AGUA CALIENTE 290 MW, AC connection 500 kV in 2010. Reprinted from [10].....	8
Figure 1-7 Power density of power electronics converter.....	9
Figure 1-8 Volume breakdown of employed components for different switching frequency. $V_C$ is the total capacitors volume, $V_L$ is the total inductors volume and $V_{sink}$ is the volume of required heatsinks for 10 kW non-isolated DC-AC inverter with boost converter. Reprinted with the permission from © 2013 IEEE [16].....	10
Figure 1-9 Volume achieved by different transformer designs with different operating frequencies. All scaled to 1MW power rating. Reprinted with the permission from © 2010 IEEE [17].....	11
Figure 2-1 Evolution of large-scale PV power plant, (a) AC collection grid for large-scale PV power plant, (b) DC collection grid for large-scale PV power plant (c) Proposed medium voltage DC collection grid for large-scale PV power plant with multi-Pulse SCR converter and hybrid step-up DC-DC converter.....	17
Figure 2-2 Presented 12-pulse SCR converter using proposed hybrid step-up DC-DC converter and line frequency phase-shift transformer.....	19
Figure 2-3 Proposed hybrid step-up DC-DC converter. ....	20

Figure 2-4 (a) Boost converter circuit diagram, (b) $V_{L1}$ and $I_{L1}$ , (c) equivalent circuit when $S_1$ is turned on, (d) equivalent circuit when $S_1$ is a turned off. ....	21
Figure 2-5 Boost converter ( $V_{O1} / V_S$ ) versus the duty ration $D_1$ for ideal and non-ideal converter. ....	24
Figure 2-6 (a) Buck-boost converter circuit diagram, (b) $V_{L2}$ and $I_{L2}$ , (c) equivalent circuit when $S_3$ is turned on, (d) equivalent circuit when $S_3$ is turned off.....	27
Figure 2-7 Buck-boost converter ( $- V_{O2} / V_S$ ) versus the duty ration $D_2$ for ideal and non-ideal converter. ....	28
Figure 2-8 Multi-secondary windings phase-shift transformer for multi-pulse SCR converter (a) 12-pulse SCR converter, (b) 18-pulse SCR converter, (c) 24-pulse SCR converter. ....	31
Figure 2-9 IV and PV characteristics for different sun irradiance levels for the designed PV farm 1.5 kV, 0.5 MW. Array type: American Solar Wholesale ASW-260M; 35 series modules; 55 parallel strings. ....	32
Figure 2-10 PV plant voltage $V_{PV}=1.5$ kV, proposed hybrid step-up DC-DC converter voltage $V_{Boost}=6$ kV, and PV plant current $I_{PV}=380$ A. ....	34
Figure 2-11 First six-pulse SCR converter voltage ( $V_{dc1}$ , $V_{dc1-Ave}$ ), second six-pulse SCR converter voltage ( $V_{dc2}$ , $V_{dc2-Ave}$ ), 12-pulse SCR converter voltage ( $V_{dc12-pulse}$ , $V_{dc12-pulse-Ave}$ ).....	34
Figure 2-12 Phase “a” secondary side transformer current ( $i_{a-Secondary}$ ), tertiary side transformer current ( $i_{a-Tertiary}$ ), and overall unfiltered input primary current ( $i_a$ ). ....	35
Figure 2-13 Utility voltages ( $V_{ab}$ , $V_{bc}$ , $V_{ca}$ ) along with unfiltered utility input currents ( $i_a$ , $i_b$ , $i_c$ ). Note the currents have been multiplied by 5 for better resolution. ....	35
Figure 2-14 FFT analysis of phase “a” secondary transformer current ( $i_{a-Secondary}$ ). ....	36
Figure 2-15 FFT analysis of phase “a” unfiltered primary utility current ( $i_a$ ).....	36
Figure 3-1 Evolution of multi-pulse SCR converter for large-scale wind turbine farm and PV plant converter (a) 12-pulse SCR to interface wind farms to a utility grid using line frequency transformer isolation. Adapted from [31], (b) conventional PV power plant with a line commutated 12-Pulse SCR converter. Adapted from [30], (c) block diagram of the proposed medium voltage DC collection grid for large-scale PV power plant with	

12-pulse SCR converter and integrated solid-state transformer (see Figure 3-2 for circuit topology). Reprinted with the permission from © 2019 IEEE [36].	41
Figure 3-2 Proposed topology of the medium voltage DC collection grid for large-scale PV power plant with SCR converter and integrated medium frequency 720 Hz solid-state transformer. Reprinted with the permission from © 2019 IEEE [36].	42
Figure 3-3 Functional operation of bidirectional AC-AC converter (Figure 3-2), (a) $V_{an}$ line to neutral input voltage 60 Hz, (b) bridge rectifier switching function $SW_{Rec}$ , (c) Medium frequency 720 Hz square wave 50% duty cycle, (d) AC-AC converter switching function $SW_{AC-AC}$ , (e) phase “a” AC-AC output voltage $V_{an}$ MF. Reprinted with the permission from © 2019 IEEE [36].	43
Figure 3-4 FFT spectrum analysis for the phase “a” AC-AC converter output voltage $V_{an}$ MF.	45
Figure 3-5 Phasor diagram of three phase zig-zag phase-shift transformer that has on group star primary windings and two sets of secondary windings to create phase-shift ( $-15^0$ , $+15^0$ ) with respect to the input primary side voltages. Reprinted with the permission from © 2019 IEEE [36].	47
Figure 3-6 Phase “a” unfiltered input current $i_{Ua}$ analysis for the proposed topology in Figure 3-2.	49
Figure 3-7 IV and PV characteristics for different sun irradiance levels for the designed PV farm 1.5 kV, 150 kW, and 100 A. Array type: American Solar Wholesale ASW-260M; 40 series modules; 15 parallel strings.	53
Figure 3-8 Primary input voltages, currents for the medium frequency phase-shifted solid-state transformer SST ( $V_{AP}$ , $I_{ap}$ ), ( $V_{BP}$ , $I_{bp}$ ), and ( $V_{CP}$ , $I_{cp}$ ). Note that the voltages are scaled down by 10 for better resolution.	59
Figure 3-9 FFT analysis for phase “a” primary voltage of the medium frequency solid-state transformer $V_{AP}$ .	59
Figure 3-10 ( $V_{PV}$ , $I_{PV}$ ), ( $V_{dc1}$ , $V_{dc1}$ Average), ( $V_{dc2}$ , $V_{dc2}$ Average), ( $V_{dc12-pulse}$ , $V_{dc12-pulse}$ Average). Note $V_{PV}$ is scaled down by 0.5 for better resolution.	60
Figure 3-11 Utility input voltages and unfiltered input currents ( $V_{an}$ , $i_{Ua}$ ), ( $V_{bn}$ , $i_{Ub}$ ), ( $V_{cn}$ , $i_{Uc}$ ). Note that the voltages are scaled down by 10 for better resolution.	61

Figure 3-12 FFT frequency spectrum for the overall unfiltered input current $i_{Ua}$ . (5 <sup>th</sup> , 7 <sup>th</sup> , 17 <sup>th</sup> and 19 <sup>th</sup> ) harmonics have been eliminated using the 12-pulse operation. ....	61
Figure 3-13 Semiconductor losses break down for the presented topology in Figure 3-2. The overall switching and conduction losses are less than (3%) of the total power.. ....	62
Figure 3-14 Prototype scale down 1 kW for the proposed topology in Figure 3-2.....	63
Figure 3-15 SCR's gate drive circuit using surface mount components.....	64
Figure 3-16 Voltage sensors board for the three phase input utility voltages ( $V_{an}$ , $V_{bn}$ , $V_{cn}$ ). ....	64
Figure 3-17 Physical medium frequency zig-zag transformer with dimensions (32 cm $\times$ 24 cm $\times$ 5 cm), 7 KVA M19 Silicon steel core material used for the experimental results. (a) front view, (b) side view. ....	65
Figure 3-18 Experimental results for medium frequency transformer primary voltages. Ch1: Phase "a" primary voltage $V_{AP}$ , Ch2: Phase "b" primary voltage $V_{PB}$ , Ch3: Phase "c" primary voltage $V_{CP}$ . Note: they are shafted by $120^0$ to each other.....	67
Figure 3-19 Experimental results. Ch. 1: Primary voltage $V_{AP}$ ; Ch. M: $V_{AP}$ FFT analysis shows the dominant frequency component appears around 720 Hz enabling the medium frequency operation.....	67
Figure 3-20 Experimental results. Ch.1 Line to Line voltage of the secondary side $V_{AB-Sec}$ ; Ch.2 Line to Line of the tertiary side $V_{AB-Ter}$ ; Ch.3 DC output voltage for the 12-pulse converter $V_{dc12-pulse}$ when ( $\alpha=0^0$ ) for rectification mode operation. ....	68
Figure 3-21 Experimental results. Ch.1 Anode cathode voltage $V_{AK}$ for $T_1$ ; Ch.2 Anode current $I_A$ for $T_1$ (see Figure 3-2).....	68
Figure 3-22 Experimental results. Ch. 1: Input line to neutral voltage $V_{an}$ ; Ch. 3: Unfiltered input current $i_{Ua}$ ; Ch. M: $i_{Ua}$ FFT spectrum analysis. (5 <sup>th</sup> , 7 <sup>th</sup> , 17 <sup>th</sup> and 19 <sup>th</sup> are eliminated due to the 12-pulse operation. ....	69
Figure 3-23 Experimental results. Ch.1: DC output voltage for the first six-pulse SCR converter $V_{dc1}=108$ V; Ch.2 DC output voltage for the second six-pulse SCR converter $V_{dc1}=110$ V; Ch. 3: DC output voltage for the 12-pulse converter $V_{dc12-Pulse}=231$ V. The firing angle ( $\alpha=0^0$ ).....	69

Figure 3-24 Experimental results. Ch.1: Transformer primary voltage $V_{AP}$ ; Ch.2: DC output voltage for the first six-pulse SCR converter $V_{dc1}=75.6$ V; Ch. 3: DC output voltage for the 12-pulse converter $V_{dc12-Pulse}=176$ V. The firing angle ( $\alpha=30^0$ ). .....	70
Figure 3-25 Experimental results. Ch.1: Transformer primary voltage $V_{AP}$ ; Ch.2: DC output voltage for the first six-pulse SCR converter $V_{dc1}=68.8$ V; Ch. 3: DC output voltage for the 12-pulse converter $V_{dc12-Pulse}=137$ V. The firing angle ( $\alpha=60^0$ ). .....	70
Figure 3-26 Experimental results. Ch.1: Input line to neutral voltage $V_{an}$ ; Ch.3: Unfiltered input current $i_{Ua}$ ; Ch. 2: DC voltage supply= $177$ V; Ch. 4: DC output voltage for the 12-pulse converter $V_{dc12-Pulse}= -146$ V. The firing angle ( $\alpha=140^0$ ). .....	71
Figure 3-27 Proposed medium frequency open delta solid-state transformer for 12-pulse SCR converter and the proposed hybrid step-up DC-DC converter. ....	73
Figure 3-28 Phasor diagram of the proposed open delta phase-shift transformer to create a ( $30^0$ ) phase-shift between the secondary and tertiary sides. Each phase has one primary winding and six secondary windings (see Figure 3-27).....	74
Figure 3-29 $V_{PV}=1.5$ kV PV plant voltage, hybrid step-up DC-DC converter output voltage= $6$ kV, $I_{PV}=380$ A PV plant current. ....	77
Figure 3-30 Output voltage of first six-pulse ( $V_{dc1}$ , $V_{dc1-Ave}$ ), output voltage of second six-pulse ( $V_{dc2}$ , $V_{dc2-Ave}$ ), output voltage of the 12- pulse ( $V_{dc12-pulse}$ , $V_{dc12pulse-Ave}$ ). .....	77
Figure 3-31 Primary voltages and currents for the open delta phase-shift solid-state transformer ( $V_{ab-P}$ , $i_{a-P}\times 3$ ), ( $V_{bc-P}$ , $i_{b-P}\times 3$ ). Note the input currents have been multiplied by 3 for better resolution.....	78
Figure 3-32 Secondary voltages and currents for the open delta phase-shift solid-state transformer ( $V_{ab-Sec}$ , $i_{a-Sec}\times 3$ ), ( $V_{bc-Sec}$ , $i_{b-Sec}\times 3$ ), ( $V_{ca-Sec}$ , $i_{c-Sec}\times 3$ ). Note the secondary currents have been multiplied by 3 for better resolution. ....	78
Figure 3-33 Tertiary voltages and currents for the open delta phase-shift solid-state transformer ( $V_{ab-Ter}$ , $i_{a-Ter}\times 3$ ), ( $V_{bc-Ter}$ , $i_{b-Ter}\times 3$ ), ( $V_{ca-Ter}$ , $i_{c-Ter}\times 3$ ). Note the tertiary currents have been multiplied by 3 for better resolution.....	79
Figure 3-34 Utility input voltages and currents ( $V_{ab}$ , $i_{Ua}\times 3$ ), ( $V_{bc}$ , $i_{Ub}\times 3$ ), ( $V_{ca}$ , $i_{Uc}\times 3$ ). Note the input utility currents have been multiplied by 3 for better resolution. ....	79

Figure 3-35 FFT analysis for phase “a” utility input current $i_{Ua}$ .....	80
Figure 4-1 Conventional solar PV grid-tied with line frequency (50/60) Hz transformer.....	84
Figure 4-2 Three phase grid-tied current source converter. ....	85
Figure 4-3 Configuration of three phase solid-state transformer that has three stages rectifier, dual active bridge DAB and inverter stage. Adapted from [51]. ....	86
Figure 4-4 Configuration of three phase soft-switching solid-state transformer. Adapted from [52]. ....	87
Figure 4-5 Proposed topology of bidirectional power flow current source converter using high frequency integrated solid-state transformer SST for utility interface of solar PV / battery energy storage systems. Reprinted with the permission from © 2020 IEEE [48].....	88
Figure 4-6 Line to neutral switching pattern for one cycle that has three angles ( $\alpha_1$ , $\alpha_2$ , $\alpha_3$ ) to eliminate the ( $5^{th}, 7^{th}$ ) harmonics and control the fundamental amplitude ( $a_1$ ). Reprinted with the permission from © 2020 IEEE [48]. ....	89
Figure 4-7 AC-AC converter switching functions (a) line to neutral input voltage $V_{an}$ (b) line frequency switching function for the rectifier bridge $S_{Rec}$ , (c) high frequency switching function for the inverter bridge $S_{Inv}$ , (d) switching function for the overall AC-AC converter $SW_{AC-AC}$ , (e) phase “a” high frequency output voltage AC-AC converter $V_{AP}$ . ....	93
Figure 4-8 Five limbs high frequency transformer, it has two exterior limbs to carry the unbalanced flux lines and three interior limbs for the main flux lines. Reprinted with the permission from © 2020 IEEE [48]. ....	96
Figure 4-9 Line to neutral bipolar switching functions ( $S_1$ , $S_2$ , $S_3$ ) to eliminate the ( $5^{th}, 7^{th}, 11^{th}, 13^{th}$ ), ( $\alpha_1 = 7.89^0$ , $\alpha_2 = 22.54^0$ , $\alpha_3 = 25.64^0$ , $\alpha_4 = 76.93^0$ , $\alpha_5 = 77.91^0$ ). Fundamental amplitude value is ( $a_1=1.15$ ) (see Table 4-1). ....	98
Figure 4-10 FFT analysis of line to neutral bipolar switching functions ( $S_1$ , $S_2$ , $S_3$ ). The eliminated harmonics are ( $5^{th}, 7^{th}, 11^{th}, 13^{th}$ ). Note that the tripled harmonics are there. ....	98
Figure 4-11 Line to line unipolar switching functions ( $S_a$ , $S_b$ , $S_c$ ) to eliminate the ( $5^{th}, 7^{th}, 11^{th}, 13^{th}$ ) and all tripled harmonics (see equations 4.13-4.15). ....	99

Figure 4-12 FFT analysis of the line to line unipolar switching function ( $S_a, S_b, S_c$ ) to eliminate the ( $5^{th}, 7^{th}, 11^{th}, 13^{th}$ ) harmonics. Note that there are no tripled harmonics.....	99
Figure 4-13 IV and PV characteristics for one-panel according to the Solarex data sheet for full sun irradiance level.....	104
Figure 4-14 IV and PV characteristics for the designed PV farm 1.5 kV, 120 kW for different sun irradiance levels.....	105
Figure 4-15 Simulation results for the proposed converter (Figure 4-5): High frequency transformer primary voltages $V_{AP}, V_{BP}, V_{CP}$ . Note the voltages have been scaled down by 2 for better resolution.....	109
Figure 4-16 Frequency spectrum for high frequency transformer primary voltages $V_{AP}, V_{BP}, V_{CP}$ . Note the dominant frequency is around 20 kHz. ....	109
Figure 4-17 (a) Simulation results for the proposed converter (Figure 4-5): (a) ( $V_{an}, i_{ua}$ ), (b) $I_A = I_{Q1} - I_{Q4}$ , (c) $I_{Q1}$ , (d) $I_{Q4}$ . Note $V_{an}$ is scaled down by 10 for better resolution. ....	110
Figure 4-18 (a) Simulation results for the proposed converter: (a) ( $V_{an}, i_{ua}$ ), (b) ( $0.1 \times V_{PV}, I_{PV}$ ), (c) $V_{rec}$ , (d) free-wheeling case pulses for the three phase current source converter. Note $V_{an}$ and $V_{PV}$ are scaled down for better resolution. ....	110
Figure 4-19 Simulation results for the proposed converter ( $V_{an}, i_{Ua}$ ), ( $V_{bn}, i_{Ub}$ ), ( $V_{cn}, i_{Uc}$ ). Note the input voltages are scaled down by 10 for better resolution. ....	111
Figure 4-20 FFT analysis of the unfiltered input currents ( $i_{Ua}, i_{Ub}, i_{Uc}$ ). ( $5^{th}, 7^{th}, 11^{th}, 13^{th}$ ) harmonics have been eliminated. Note that the first dominant harmonic is the $17^{th}$ (1020 Hz). ....	111
Figure 4-21 Experimental set up for the proposed topology in Figure 4-5.....	112
Figure 4-22 Five limbs high frequency 20kHz transformer. Wire type Foil 22, 15 KVA, FERROXCUBE 3C94, core material used for the experimental set up. ....	113
Figure 4-23 Experimental results of microcontroller signals. Ch1: Line to neutral input voltage $V_{an}$ , (Ch2&Ch3): Phase “a” unipolar switching function $S_a$ , Ch3: Phase “a” switching function for the AC-AC converter $SW_{AC-AC}$ .....	114



Figure 4-24 Experimental results of microcontroller signals. Ch1:Line to neutral input voltage $V_{an}$ , Ch2: Pulses for Q1, Ch4: Pulse for Q4, Ch3: Positive half cycle for unipolar switching function $S_a$ . .....	114
Figure 4-25 Experimental results for Physical dead time=(0.56 u sec). Ch.2: Gating signal for Q <sub>1</sub> , Ch.3: Gating signal for Q <sub>4</sub> . .....	115
Figure 4-26 Experimental results for high frequency 20 kHz transformer input voltages. Ch.1: $V_{AP}$ , Ch.2: $V_{BP}$ , Ch.3: $V_{CP}$ . Note that they are shifted by 120 degree for three phase operation. ....	115
Figure 4-27 Experimental results. Ch.2: Phase “b” input primary voltage $V_{BP}$ , Ch.M: Frequency spectrum analysis for $V_{BP}$ . Note the dominant frequency is around 20 kHz. ....	116
Figure 4-28 Experimental results for the rectification mode operation. Ch.1: Line to neutral input voltage $V_{an}$ , Ch.2: $V_{rec}$ , Ch. 3: Overall phase “a” unfiltered current $i_{Ua}$ . Note that the power goes from the AC to the DC side.....	116
Figure 4-29 Experimental results for the inversion mode operation. Ch.1: Line to neutral input voltage $V_{an}$ , Ch. 2: $V_{rect}$ , Ch.3: Overall phase “a” unfiltered current $i_{Ua}$ ; Note that $V_{rect}$ is negative and the power goes from the DC to the AC side. ....	117
Figure 4-30 Medium frequency transformer 720 Hz (M19 Silicon steel core material, 7 KVA), High Frequency transformer 20 kHz (FERROXCUBE 3C94 Ferrite core material, 15 KVA). ....	119

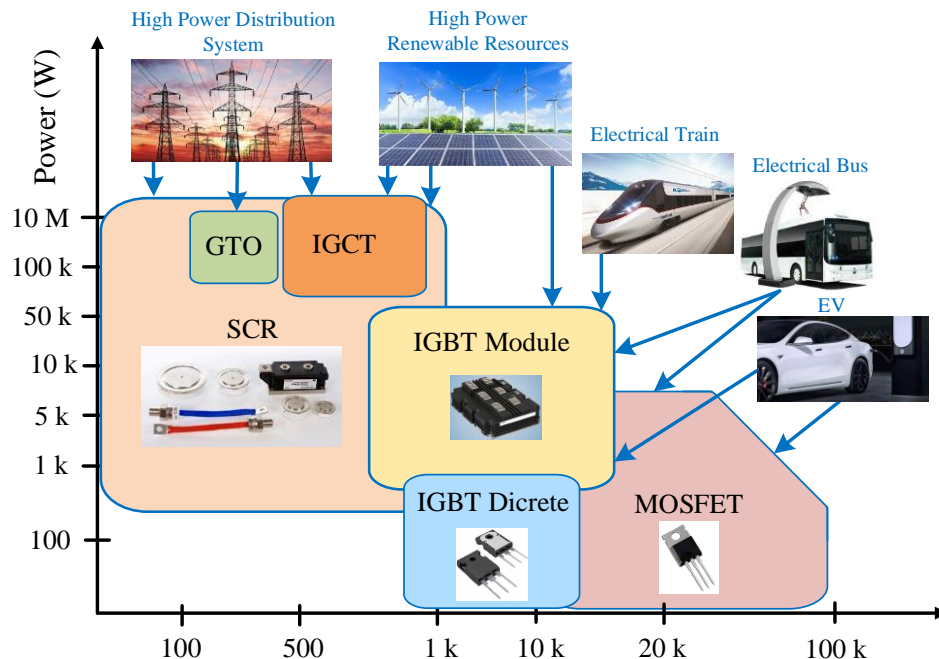
## LIST OF TABLES

	Page
Table 1-1 High power switching devices for different manufacturers in terms of their voltage, current ratings capability, and their applications.....	2
Table 2-1 Voltage ratings for ( $S_1, S_2, S_3, S_4$ ) of the proposed hybrid step-up DC-DC converter.....	29
Table 2-2 Design example parameters for 12-pulse SCR converter using the proposed hybrid step-up DC-DC converter.....	33
Table 3-1 Medium frequency transformer ratings for the design example of the presented topology in Figure 3-2.....	54
Table 3-2 Semiconductor device ratings for the design example of the presented topology in Figure 3-2. ....	55
Table 3-3 Simulation parameters for the design example of the proposed topology in Figure 3-2. ....	57
Table 3-4 Simulation parameters for the design example of the proposed open delta concept in Figure 3-27. ....	75
Table 4-1 Switching angles for line to neutral selective harmonic elimination for different objective functions including control the fundamental amplitude ( $a_1$ ).....	90
Table 4-2 Solarex one-panel parameters. ....	104
Table 4-3 Semiconductor device ratings for the desing example of the presented topology in Figure 4-5. ....	106
Table 4-4 High frequency transformer ratings for the design example of the presented topology in Figure 4-5.....	107
Table 4-5 Simulation parameters for the design example of the proposed topology in Figure 4-5. ....	107

# 1. INTRODUCTION

## 1.1. High Power Switching Devices


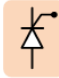



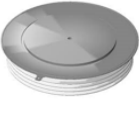




In the middle of 1980, when the gate turn-off thyristor GTO 4500V was commercially available, the high power converter and medium voltage scale started. The GTO was the standard for the medium voltage scale until the insulated gate bipolar transistor IGBT and integrated gate commutated thyristor IGCT come to the picture in the late 1990s [1]. These switching devices have been used widely in the medium voltage power electronics converters due to their reliability and superior switching characteristics in terms of low power losses and easy to control [2]. Figure 1-1 shows semiconductor power device ratings versus their switching frequency and applications.



**Figure 1-1 Semiconductor power devices ratings versus switching frequency and their applications.**

Mainly, there are two types of switching devices for high power converters: Thyristors and Transistors [3]. The first group involves silicon control rectifier SCR, gate turn-off thyristor GTO, and integrated gate commutated thyristor IGCT. The transistors include insulated gate bipolar transistor IGBT and injection enhanced gate transistor IEGT. Other switches have not gained significant attention in high power application such as power MOSFET, emitter turn off thyristor ETO [3]. Table 1-1 shows different high power switching devices in terms of their voltage, current ratings capability.

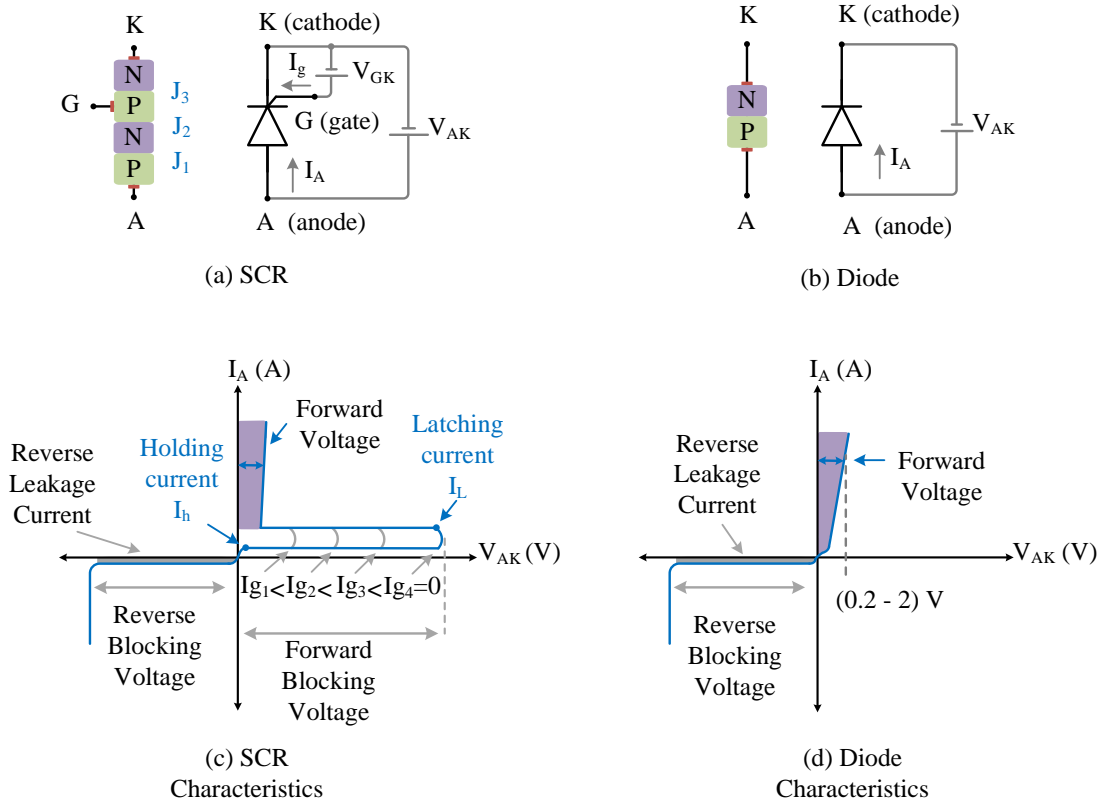
**Table 1-1 High power switching devices for different manufacturers in terms of their voltage, current ratings capability, and their applications.**

Name	Diode	SCR	GTO	IGCT	IGBT
Symbol					
Figure					
Max Voltage, Current	Wescode 3.6 kV, 1.4 kA	Semikron 2.7 kV, 1.2 kA	ABB 4.5 kV, 4 kA	ABB 5.0 kV, 1.1 kA	Infineon 6.5 kV, 0.75 kA
Applications	Multi-pulse MV Rectifier	Multi-pulse MV converter	PWM CSC 3L NPC	MV PWM CSC 5L NPC	MV 2L VSC 5L NPC

**1.1.1. Silicon Control Rectifier SCR**

Silicon control rectifier SCR is an essential switch in the high power converter applications especially in high voltage direct current HVDC, because it is reliable and

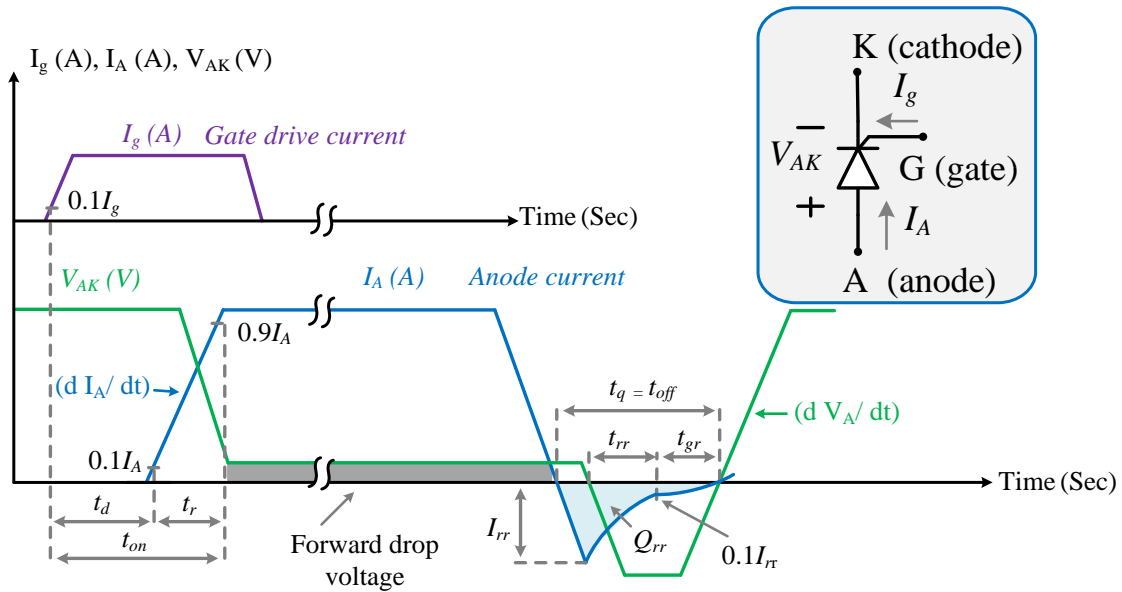
robust. Some SCR switches can carry up to 4500 A with blocking voltage capability up to 8500 V [3,5]. Figure 1-2 shows the structure of a power diode, and SCR switch. The diode has two terminals anode (A) and the cathode (K). However, the SCR has three terminals anode (A), cathode (K), and the gate (G). Once the gating signal is applied to SCR, the layers between junction (J2) and junction (J3) becomes negative (N), and SCR becomes a PN- junction device same as a diode. SCR works similarly like a diode, but the starting of conduction can be controlled using the gating signal. Figure 1-2 (c) demonstrates the gating signal. It can be considered as a control diode because if there is no gating signal ( $i_g=0$ ), it can behave as an open circuit, as shown in Figure 1-2 (c). If the voltage across SCR  $V_{AK}$  increases, there is small leakage current flows, but if this voltage reaches the breakdown limit, the switch will breakdown either in the forward or reverse direction (see Figure 1-2 (c)). If the gating signal is applied, the  $V_{AK}$  dramatically decreases, and it works like a diode.  $I_L$  is the latching current, which is the minimum anode current  $I_A$  that is required to switch SCR on. Once anode current  $I_A$  reaches  $I_L$ , the gating signal can be removed ( $I_g=0$ ), and SCR will be on as long as the anode current  $I_A$  is bigger than or equal to the holding current  $I_h$ , which is the minimum anode current to keep the SCR on [4,6]. Figure 1-3 explains SCR's on-off switching characteristics. The transition from off state to on state requires ( $t_{on} = t_d + t_r$ ),  $t_d$  is the delay time and  $t_r$  is the rise time. The transition from on state to the forward blocking state is called the commutation transition or turn off time ( $t_q = t_{rr} + t_{gr}$ ),  $t_{rr}$  is the reverse recovery time and  $t_{gr}$  is the gate recovery time. SCR has four layers and three junctions.



**Figure 1-2 High power semiconductor devices (a) SCR, (b) Diode, (c) SCR's characteristics, (d) diode's characteristics.**

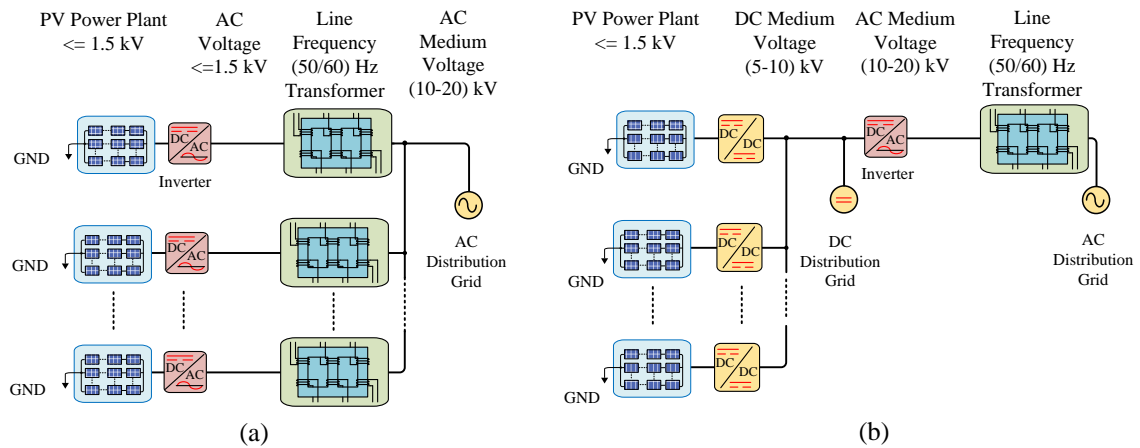
## 1.2. Introduction to AC and DC Collection Grid

In general, for large-scale renewable energy solar/wind turbine resources, these resources can be harvested using either AC collection grid or DC collection grid [7,8,18,19]. Figure 1-4 shows the schematic diagram of the AC collection grid and DC collection grid. The disadvantages of the AC collection grid include the required of large size line frequency filters and step-up line frequency (50/60) transformer. Moreover, the AC collection grid uses many distributed DC-AC inverters, which results to decrease



**Figure 1-3 SCR turn on and turn off switching characteristics.**

stability, reliability, and increases losses of the system [9]. However, the DC collection grid is another option to harvest the large-scale renewable energy resources. It composes one central inverter interfaced with the utility grid via line frequency transformer, as shown in Figure 1-4 (b). Another feature of the DC collection grid is the absence of reactive power in the DC side cables. Many research approaches show that increasing the PV plant DC voltage system from 1000V to 1500V has the advantages of improving efficiency, decreasing size, complexity, and losses. [10,11,12]. According to the First Solar in 2016 [10], the new architecture of 1500V medium voltage direct current MV DC PV power plant removes the DC combiner boxes and enables the use of DC-DC converters. The output voltages of these DC-DC converters can be easily boosted to multiple string voltage levels, which is 1500V. The higher DC voltage decreases current and results to travel long distances to the nearest substation [13].



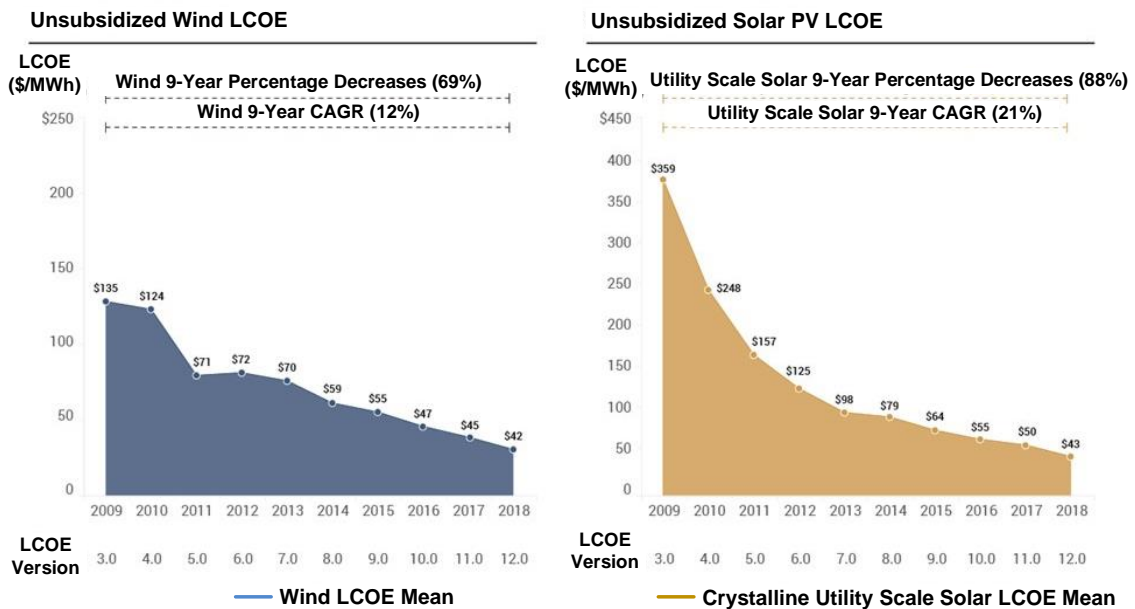
**Figure 1-4 Schematic diagram of large-scale PV power plant. (a) AC collection grid, (b) DC collection Grid.**

Using the medium voltage DC collection grid eliminates the PV array field inverters, transformers, AC equipment cabling systems from the PV plant side, which reduces the cost of installation, and reduces labor in the field. Furthermore, the MV DC collection grid is ready to accept the battery storage systems. Finally, the MV DC grid enables the use of one central inverter for the grid-tied via line frequency transformer [12,13]. However, the central inverter's switches IGBT/ MOSFET have limitations to handle high power. Comparing MV DC collection architecture with the pre-existing AC collection grid, the DC collection one can achieve a reasonable cost structure. In response to these points, this dissertation proposes a medium voltage DC collection grid for large-scale PV power plants using multi-pulse SCR converter and zig-zag phase-shift transformer. In order to overcome the limitations of handling high power in the medium voltage scale. SCR switches can be used because they are more reliable, robust, and less expensive compared to IGBT/MOSFET, according to [14].



### 1.3. Large Scale PV Plant

For large scale PV plant, the solar/wind electricity cost is less than the conventional generation according to [10,15]. The reasons behind dropping the solar price are the reduction of the module cost and the balance of system BOS. The BOS involves the cost of the inverter, structure, labor, design, and engineering. According to the cost of energy analysis at Lazard Levelized website, the solar/wind price per MWh is decreased [15]. In 2017, Arizona utility company signed a contract to buy electricity from a 100 MW PV plant (0.3 cents/ kWh). In 2017 in Austin, Texas, the price went down to about (2.5 cents/ kWh) for 150 MW of solar farm. Figure 1-5 shows the dropping of price unit per MWh for large-scale PV plant and wind turbine from 2009 till 2018.



**Figure 1-5 Price unit/ MWh for both wind and solar according to Lazard Levelized cos of energy analysis. Reprinted from [15].**



**Figure 1-6 Utility scale PV plant in Arizona AGUA CALIENTE 290 MW, AC connection 500 kV in 2010. Reprinted from [10].**

Figure 1-6 shows a typical PV plant 290 MW in Arizona. It composes PV panels, power conversion to convert the DC power to AC power and substation to aggregate the total power to send it to the transmission grid. According to the First solar, 1500V DC PV plant is more beneficial than 1000V DC PV plant because the higher voltage means low losses, smaller number of conversions, smaller number of connections (wiring) [10].

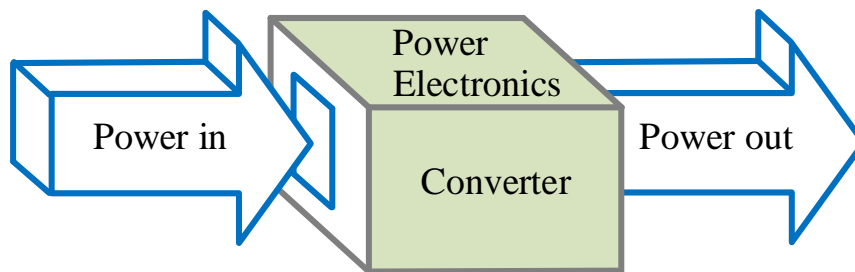
#### **1.4. Power Density**

In this dissertation, the power density of a power electronics converter is defined as the ratio of total power process through a converter (watt) to the total volume occupied by that power converter in ( $\text{dm}^3$ ) as given by (1.1) and shown in Figure 1-7. It is desired to have a high power density for power electronics converters, especially for high power

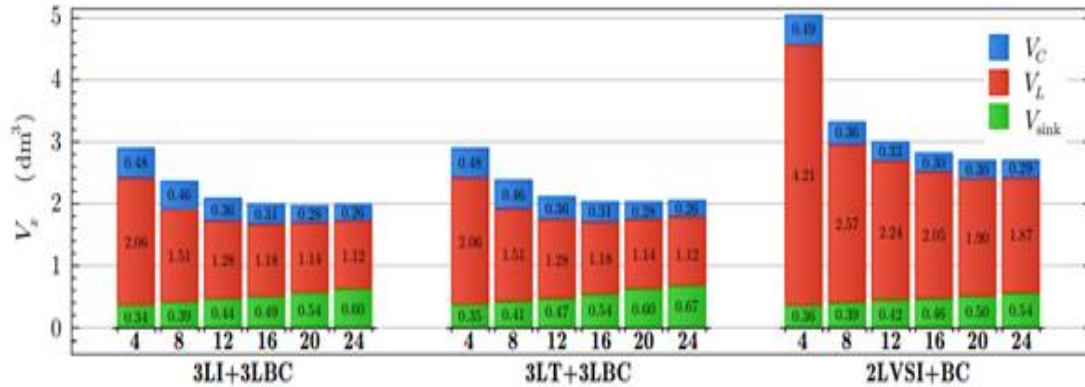
grid-tied systems, because it reduces the cost in terms of installation and maintenance. Having high power density means a small footprint of power electronics converters.

$$\text{Power Density} = \frac{\text{Total power process (w)}}{\text{Total volume occupied (dm)}^3} \quad (1.1)$$

The power electronics converter's components that have the highest impact on the power density are the magnetic components such as inductors/transformers, total capacitors, including EMI filters and DC-link capacitors and the cooling system (heatsinks). Figure 1-8 shows the volume breakdown of power electronic converter components for non-isolated 10 kW DC-AC inverter [16].  $V_L$  is the total volume occupied by inductors,  $V_C$  is the total volume occupied by capacitors and  $V_{\text{Sink}}$  is the total volume occupied by heat sinks. For 4 kHz, the total volume occupied for a two-level voltage source inverter with a boost converter (2LVSI+BC) is (5.06 L) ( $1L=1 \text{ dm}^3$ ).



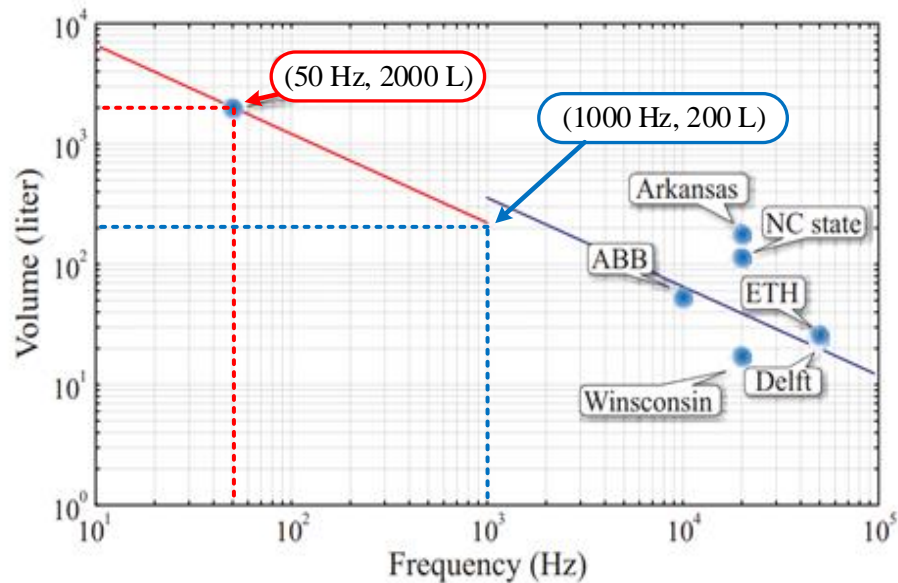
**Figure 1-7 Power density of power electronics converter.**



**Figure 1-8 Volume breakdown of employed components for different switching frequency.  $V_C$  is the total capacitors volume,  $V_L$  is the total inductors volume and  $V_{sink}$  is the volume of required heatsinks for 10 kW non-isolated DC-AC inverter with boost converter. Reprinted with the permission from © 2013 IEEE [16].**

The volume break down as follows: the inductors volume is occupied about 4.21 L, the DC capacitors volume is occupied 0.49 L and the heat sinks volume is occupied 0.36 L.

The study shows increasing the switching frequency operation will decrease the volume occupied of the converter. For example, if the switching frequency increases to 24 kHz, the total volume occupied for the same inverter would go down to 2.7 L. Furthermore, it shows other converters break down components volume occupied for different switching frequency operations. If the galvanic isolation has to be considered to this study, it will occupy about 75% of the total volume of the overall converter for 10 kVA. It can be seen that galvanic isolation, such as transformer, has a direct impact on the power density of the power electronics converters. It is clear that (70-80) % of the volume is occupied by the magnetic components. The second occupied volume is the DC-link capacitors. Therefore, it is necessary to design power electronics converters that could have less.



**Figure 1-9 Volume achieved by different transformer designs with different operating frequencies. All scaled to 1MW power rating. Reprinted with the permission from © 2010 IEEE [17].**

footprint of magnetic components and reduce/eliminate the use of DC-link capacitors if it is possible. According to [17], one of the best ideas to increase the power density of the power electronics converter by increasing the frequency of a transformer or inductor. At high frequency, a transformer's core can carry the same amount of flux lines at a smaller cross-section area. Figure 1-9 [17] demonstrates that if the transformer core's frequency is increased from 50 Hz to 1 kHz the volume of 1MVA silicone steel (Si) core transformer can be reduced from 2000 L to 200 L, respectively. The inverse relation between operating frequency and magnetic core area is given by (1.2).  $E_{rms}$  is the induced voltage of winding,  $N$  is number of turns in the winding,  $A$  is cross section area of core in ( $m^2$ ),  $B_{max}$  refers to the peak magnetic flux density (Tesla),  $f$  is transformer's core frequency. In order to

maintain the transformer efficiency high, the magnetic core material has to be selected properly because at high frequency transformer core losses should be considered.

$$A = \frac{E_{\text{rms}}}{\sqrt{2} \cdot \pi \cdot f \cdot N \cdot B_{\text{max}}} \quad (1.2)$$

### 1.5. Research Objective

The main objective of this dissertation is to design, simulate, analyze, and construct new approaches to interface the renewable energy resources solar/wind turbine to the electrical utility using an integrated solid-state transformer. The proposed topologies are simple and have the same performance as the conventional approaches. However, using a solid-state transformer would improve the power density of the proposed approaches. Simulation results along with experimental results on a scale down laboratory prototype demonstrate the feasibility of the proposed concepts. In this dissertation, four different bidirectional power flow converters are proposed.

For the first topology, a medium voltage DC collection grid using a multi-pulse SCR converter and line frequency transformer is proposed. A new hybrid step-up DC-DC converter is proposed along with this concept. It can boost up a 1.5 kV DC PV plant to the medium voltage range 6 kV DC.

In the second presented topology, a medium voltage DC collection grid for large-scale PV power plant using SCR converter and employing a medium frequency 720 Hz integrated solid-state transformer. The features of this topology are; simple, easy to

control, eliminates the need for a DC-link, low numbers of power conversion stages, the proposed system allows for bidirectional power flow for interfacing battery energy system to the utility grid.

In the third presented topology, a medium frequency integrated solid-state transformer using open delta scheme connection is proposed. The open delta concept increases the reliability of the multi-pulse SCR converter and improves the efficiency further.

In the final approach, a unique bidirectional power flow current source converter using selective harmonics elimination SHE pulse width modulation PWM is presented. This topology is employing a high frequency 20 kHz integrated solid-state transformer for galvanic isolation. The input utility current is designed to have high quality by removing the low order harmonics, e.g. (5th,7th,11th, and 13th). Bidirectional power flow is achieved in this topology to use it for PV power harvesting or electric vehicle EV charging stations. Furthermore, the DC-link capacitor is removed to result in more reliability and power density.

Mathematical analysis and design example for each topology are presented. The zig-zag medium frequency transformer and high frequency transformer is designed and simulated using MATLAB Simulink and PSIM software to validate the proposed concepts. Furthermore, experimental results on scale down laboratory prototypes are presented to verify the proposed approaches.

## **1.6. Dissertation Outline**

The dissertation has five sections. Section 1 presents high power switching devices, for example, SCR, power diode, IGBT, MOSFET, and IGCT. Mainly, it is focusing on SCR switch characteristics. The difference between the AC and DC collection grid is discussed. Moreover, a large-scale PV plant with some real examples are illustrated. The power density of power electronics converters concept is discussed too.

In section 2, a medium voltage DC collection grid with multi-pulse SCR converter and line frequency phase-shift transformer is explained. A hybrid step-up DC-DC converter is proposed to boost up 1.5 kV DC PV plant to 6 kV DC. The math analysis and design example for the hybrid DC-DC converter are discussed in details.

In section 3, a medium voltage DC collection grid for a large-scale 12-pulse SCR converter and medium frequency integrated solid-state transformer SST is proposed. This section explains how to design a phase-shift medium frequency zig-zag multi-windings transformer. The design example for a medium voltage DC collection grid is introduced to interface with 1.5 kV, 150 kW PV plant to a utility grid. Simulation results using MATLAB/ Simulink and scaled-down laboratory prototype are presented to validate the proposed concept.

In section 4, a bidirectional current source converter is introduced using selective harmonic elimination SHE pulse width modulation PWM. A high frequency 20 kHz ferrite core solid-state transformer is designed and used for galvanic isolation for the proposed concept to further improve the power density. Low order harmonics are eliminated from the unfiltered input currents using the SHE PWM technique. This proposed concept has



some advantages. For example, it could work as an inverter to interface a PV farm to the utility grid, or it could work as a rectifier converter for electric vehicle charging station. The DC-link capacitor is removed to increase the reliability of the converter. Complete design example, simulation results using PSIM software along with a scale down laboratory prototype are presented to verify the proposed concept.

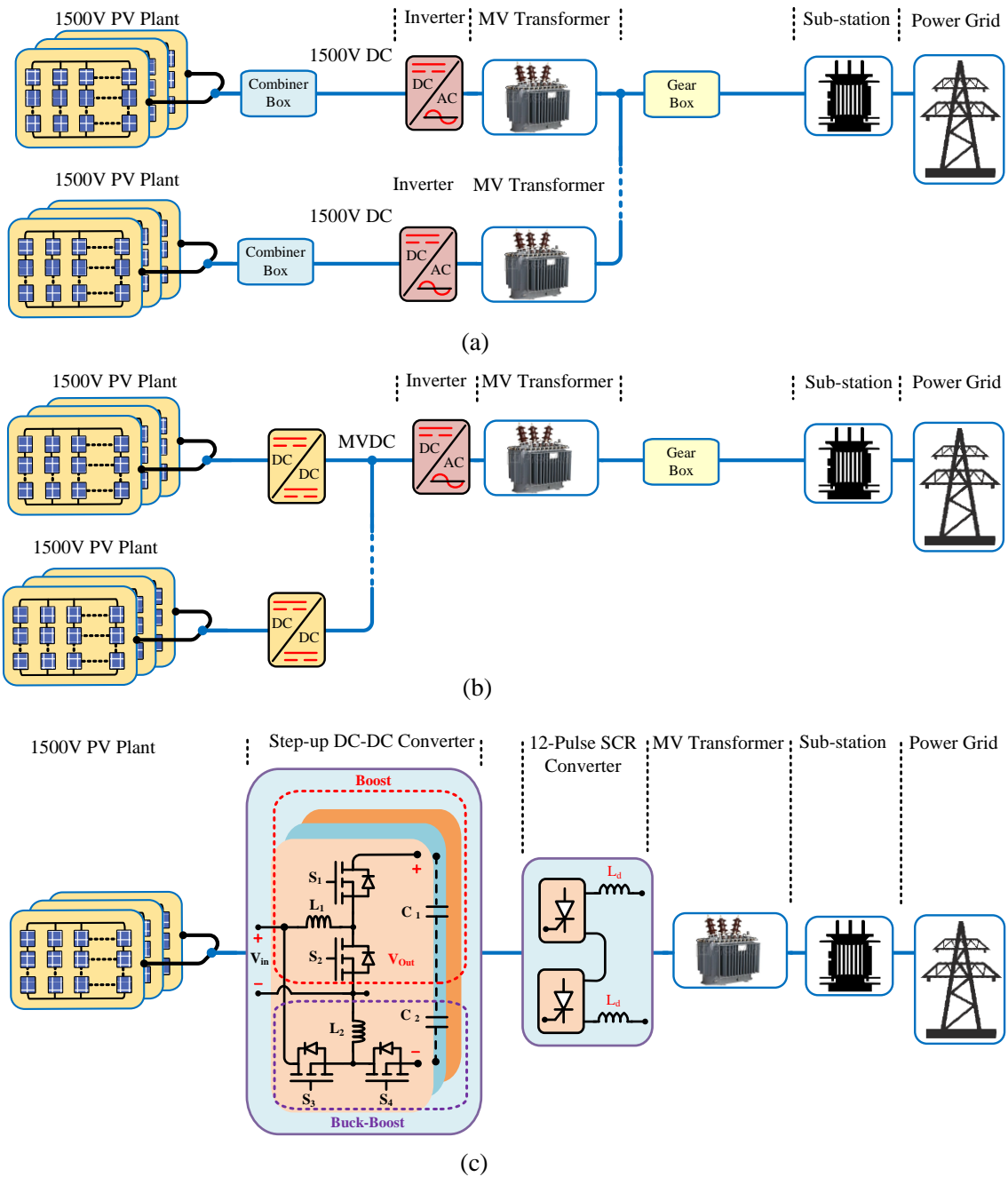
In section 5 of this dissertation, brief summary for each topology is discussed. Furthermore, possible future studies regarding the use of integrated solid-state transformers to interface renewable energy resources are suggested.

## **2. MEDIUM VOLTAGE DC COLLECTION GRID CONCEPT FOR LARGE - SCALE PV POWER PLANT USING MULTI-PULSE LINE FREQUENCY SCR CONVERTER AND HYBRID STEP-UP DC-DC CONVERTER**

In this section, a medium voltage MV DC collection grid for large-scale PV farm with multi-pulse line commutated SCR converter and hybrid step-up DC-DC converter is proposed to interface a MV utility grid. DC PV farm is the first processed via a step-up DC-DC converter, and then a 12-pulse SCR converter interfaced with the utility grid via line frequency (50/60) Hz phase-shifted transformer. The function of the hybrid DC-DC converter is to boost a 1.5 kV DC PV farm voltage to 6 kV DC. The analysis shows a good quality of the line input current due to the multi-pulse operation. The proposed approach is a current source converter. It is simple, robust and allows bidirectional power flow in case of a battery charging system. Simulation results are presented to validate the proposed concept.

### **2.1. Introduction**

A Typical photovoltaic PV farm grid-tied medium voltage employs DC-DC Converter and three phase inverter. The inverter has such a limitation in terms of handling high power due to the constraint of the semiconductor switches. Multi-pulse SCR converters have been widely used for large-scale renewable energy applications solar /wind turbines [20,21, 22]. This section proposes a MV DC collection grid for large-scale PV plant using 12-pulse SCR converter and hybrid step-up DC-DC converter. Figure 2-1 shows the evolutionary schematics for interfacing PV plant to a utility grid.



**Figure 2-1 Evolution of large-scale PV power plant, (a) AC collection grid for large-scale PV power plant, (b) DC collection grid for large-scale PV power plant (c) Proposed medium voltage DC collection grid for large-scale PV power plant with 12-Pulse SCR converter and hybrid step-up DC-DC converter.**

The presented concept has the following advantages:

- 1) The proposed system is robust current fed.
- 2) Bidirectional power flow can be achieved by adjusting the firing angle ( $\alpha$ ).
- 3) Boosting up the DC voltage to the medium voltage scale 6 kV using the proposed hybrid step-up DC-DC converter.
- 4) Low order harmonics (5<sup>th</sup>, 7<sup>th</sup>) have been eliminated from the line input current due to 12-pulse operation.

## **2.2. Proposed Medium Voltage DC Collection Grid for Large-Scale PV Power Plant Using Multi-Pulse SCR Converter and Hybrid Step-up DC-DC Converter**

The proposed 12-pulse SCR converter using the hybrid step-up DC-DC converter and line frequency (50/60) Hz phase-shift transformer is shown in Figure 2-2. The presented topology involves three parts: step-up DC-DC converter, 12-pulse SCR converter, and phase-shift line frequency (50/60) Hz transformer.

### **2.2.1. Proposed Hybrid Step-up DC-DC Converter**

The proposed hybrid step-up DC-DC converter is shown in Figure 2-3. It composes two parts; the first one is a boost converter at the top half, and the second one is a buck-boost converter at the bottom half.  $V_s$  is the common input voltage for both converters.  $V_{C1}$  is the boost output voltage, and  $V_{C2}$  is the buck-boost output voltage. In order to do the analysis for this hybrid converter, there would be some assumptions as follows:

- Assuming that the converter is working at the continuous conduction mode (CCM)

Which implies the inductors currents (  $I_{L1min}$ ,  $I_{L2min}$  ) are always greater than zero.

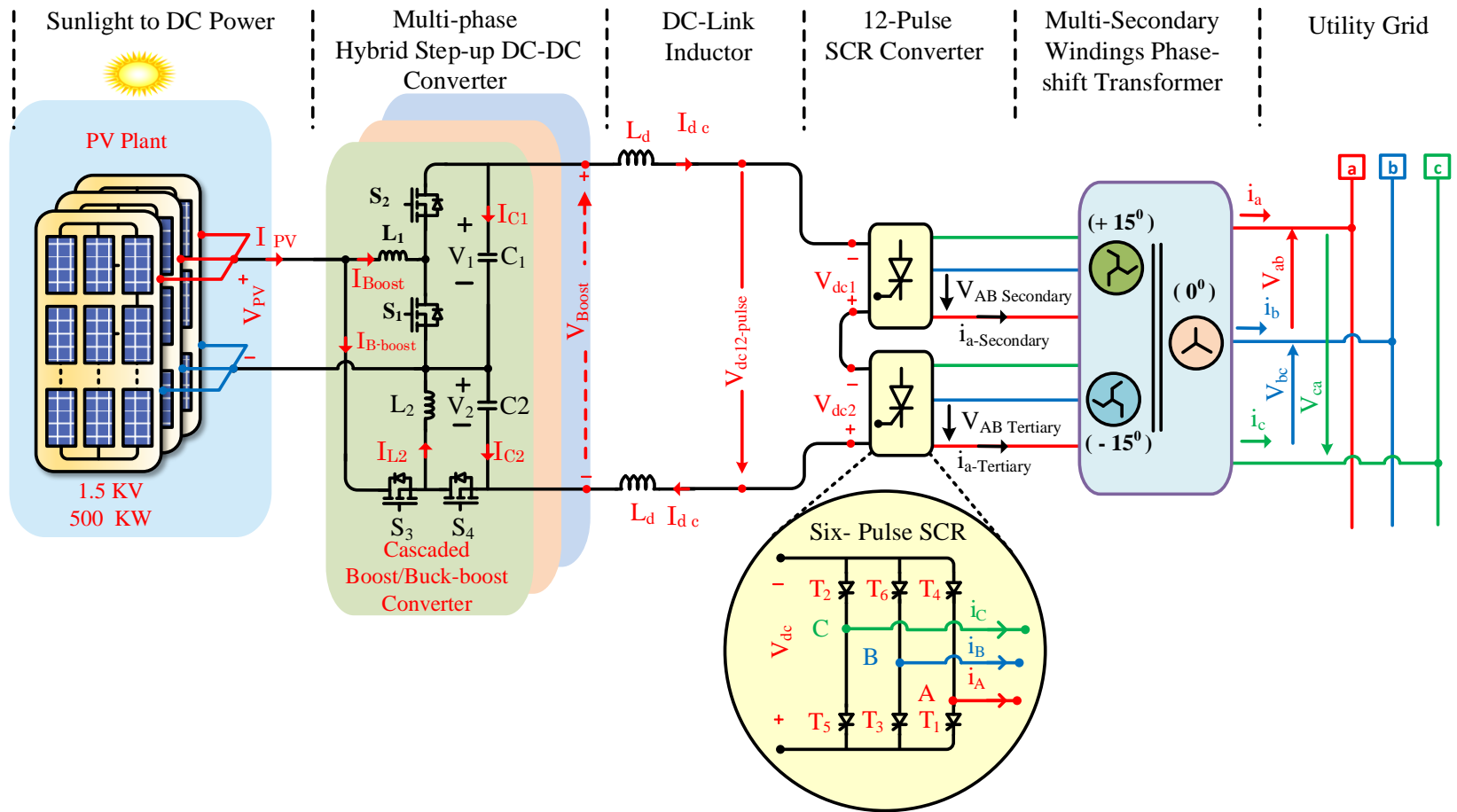
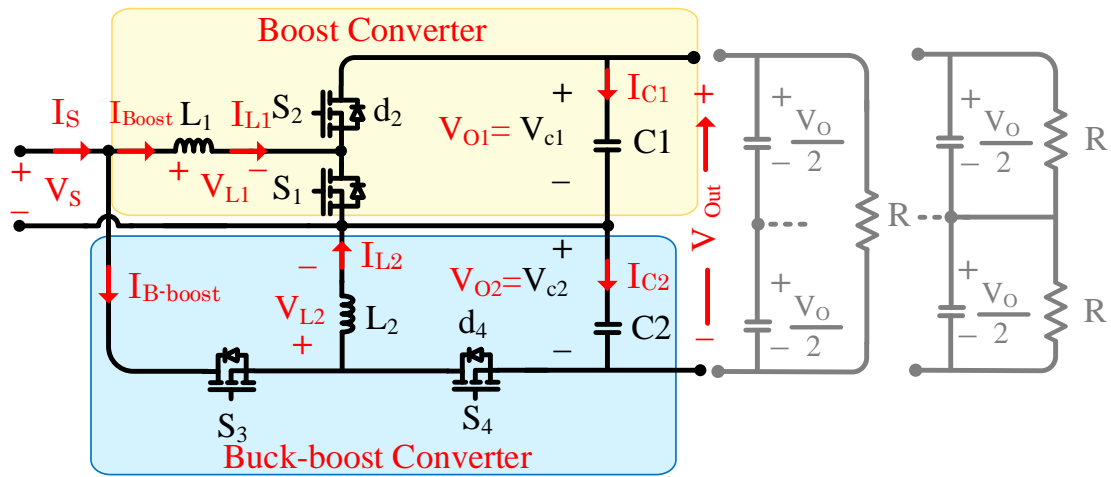


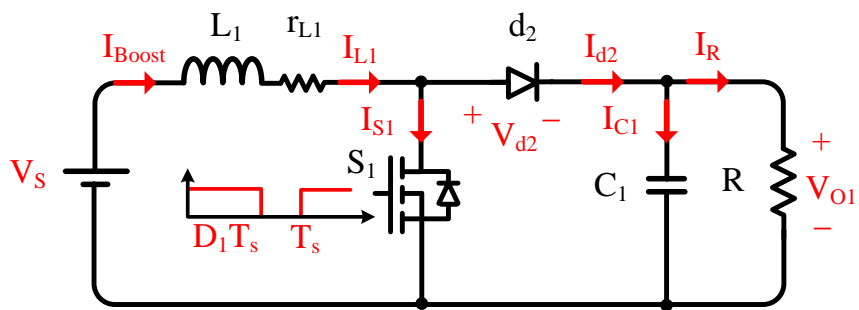
Figure 2-2 Presented 12-pulse SCR converter using proposed hybrid step-up DC-DC converter and line frequency phase-shift transformer.



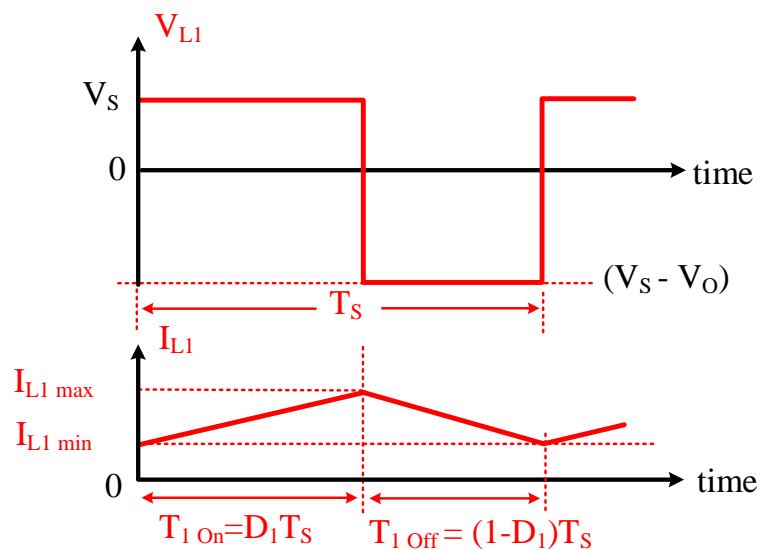
**Figure 2-3 Proposed hybrid step-up DC-DC converter.**

- The converter works at the steady state condition, which means the average inductors voltages ( $V_{L1}, V_{L2}$ ) will be zero and the average capacitors currents ( $I_{C1}, I_{C2}$ ) will be zero too.
- All the components are ideal  $r_L = 0, R_{ds} = 0$ .  $r_L$  is the inductor's internal resistor,  $R_{ds}$  is the MOSFET's on-state resistor. In other words, the input power is equal to the output power.
- Switching transient is neglected.

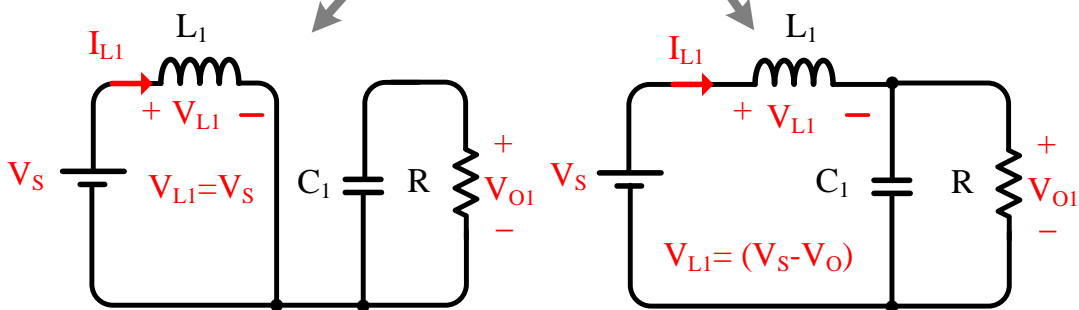
For the boost converter analysis, Figure 2-4 shows the equivalent circuit diagram depending on the status of switch  $S_1$ . There will be two modes. Mode1 when  $S_1$  is turned on for the interval  $(0 < t < D_1 \cdot T_s)$ .  $D_1$  is the duty ratio, which is the on-time interval divided by the period  $T_s$  as given by (2.1).



(a)



(b)



(c)

(d)

Figure 2-4 (a) Boost converter circuit diagram, (b)  $V_{L1}$  and  $I_{L1}$ , (c) equivalent circuit when  $S_1$  is turned on, (d) equivalent circuit when  $S_1$  is turned off.

$f_s$  is the switching frequency. The complementary duty ratio  $D_1'$  is given by (2.3) [4]. the equivalent circuit diagram for this mode is shown in Figure 2-4 (b, c).

$$D_1 = \frac{T_{1\text{ On}}}{T_s} \quad (2.1)$$

$$T_s = \frac{1}{f_s} \quad (2.2)$$

$$D_1' = 1 - D_1 \quad (2.3)$$

In this mode, the inductor voltage  $V_{L1}$  and diode voltage  $V_{d2}$  are given by (2.4), (2.5) respectively. The boost converter input current source  $I_{\text{Boost}}$  is given by (2.6) [4].

$$V_{L1} = V_s \quad (2.4)$$

$$V_{d2} = -V_{O1} \quad (2.5)$$

$$I_{\text{Boost}} = I_{L1} \quad (2.6)$$

The switch  $S_1$  and the diode  $d_2$  should be able to handle the output voltage  $V_{O1}$ . In the second mode Figure 2-4 (b, d),  $S_1$  is turned off for the interval ( $D_1 \cdot T_s < t < T_s$ ). The diode  $d_2$  is forward bias and its current is given by (2.7) for any given time. Under the steady state condition, the capacitor average current  $i_{C1\text{ ave}}$  is zero. Therefore, the average diode current  $i_{d2\text{ ave}}$  is going to be the same as the load average current  $i_{R\text{ ave}}$  as given by (2.9).

$$I_{d2} = i_{C1} + i_R \quad (2.7)$$



$$I_{d2 \text{ ave}} = i_{C1 \text{ ave}} + i_{R \text{ ave}} \quad (2.8)$$

$$i_{d2 \text{ ave}} = i_{R \text{ ave}} \quad (2.9)$$

For continuous conduction mode, the minimum value for  $L_{1\text{min}}$  is given by (2.10) [4].

$$L_{1\text{min}} = \frac{D_1 (1 - D_1)^2 \times R}{2f_s} \quad (2.10)$$

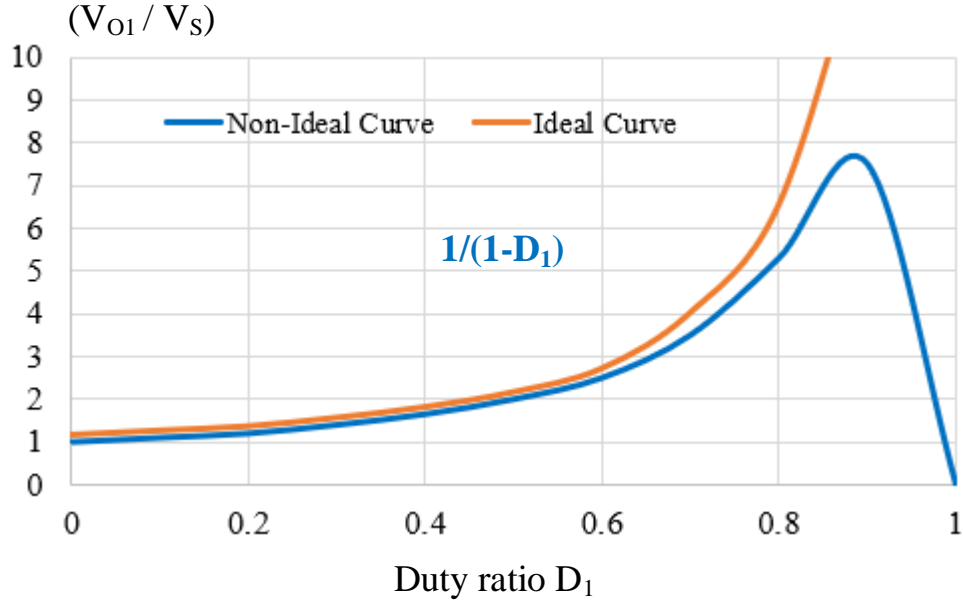
The capacitor  $C_1$  value in terms of output voltage ripple ( $\frac{\Delta V_{O1}}{V_{O1}}$ ) is given by (2.11) [24].

$$C_1 = \frac{D_1}{R \left( \frac{\Delta V_{O1}}{V_{O1}} \right) f_s} \quad (2.11)$$

The ideal boost converter voltage gain is given by (2.12) [23, 24].

$$\frac{V_{O1}}{V_S} = \frac{1}{1 - D_1} = \frac{1}{D_1'} \quad (2.12)$$

For non-ideal boost converter involving the series on-state resistor of the switch  $R_{ds1}$  and inductor's internal resistor  $r_{L1}$ , the voltage gain is given by (2.13) [24].  $R$  is the load resistor. Figure 2-5 illustrates the boost converter relationship between the normalized voltage gain ( $\frac{V_{O1}}{V_S}$ ) and duty ratio  $D_1$ . The Figure shows the ideal and practical voltage gain curves. The non-ideal one due to  $R_{ds1}$ ,  $r_{L1}$ , and the voltage drop across the diode  $V_{d2}$ . These parameters will affect the voltage conversion ratio. The allowable range of  $D_1$  is between (0.2 - 0.8) for the non-ideal case. When  $D_1=1$ , there is no power transfer because of  $V_{O1} = 0$  volt.



**Figure 2-5 Boost converter ( $V_{O1} / V_s$ ) versus the duty ratio  $D_1$  for ideal and non-ideal converter.**

$$\frac{V_{O1}}{V_s} = \left[ \frac{1}{D_1'} \times \frac{1}{1 + \frac{r_{L1} + D_1 \times R_{ds1}}{R \times (D_1')^2}} \right] \quad (2.13)$$

The second part of the proposed hybrid step-up DC-DC converter in Figure 2-3 is the buck-boost converter, as illustrated in Figure 2-6 (a). In this converter, the output voltage can be either bigger or smaller than the input voltage. The duty ratio for the buck-boost converter  $D_2$  is given by (2.14)[4]. The on time interval and off time interval are given by (2.15-2.16), respectively.

$$D_2 = \frac{T_{2\text{on}}}{T_s} \quad (2.14)$$

$$\text{On time interval} = T_{2 \text{ on}} = D_2 \times T_s \quad (2.15)$$

$$\text{Off time interval} = T_{2 \text{ off}} = (1 - D_2) \times T_s = D_2' \times T_s \quad (2.16)$$

This converter also has two operation modes depending on the status of  $S_3$ . Mode 1 when  $S_3$  is turned on for the interval ( $0 < t < D_2 \cdot T_s$ ). The equivalent circuit diagram is shown in Figure 2-6 (b, c). In this mode, the diode  $d_4$  will be reverse bias by voltage ( $V_S + V_{O2}$ ). In the second mode,  $S_3$  is turned off for the interval time ( $D_2 \cdot T_s < t < T_s$ ). Since  $I_{L2}$  is already has been built with a positive value, it will force a path to the capacitor  $C_2$  and R load through the diode  $d_4$ . The minimum value of  $L_{2\text{min}}$  for the continuous conduction current is given by (2.17) [24].

$$L_{2\text{min}} = \frac{(1 - D_2)^2 \times R}{2f_s} \quad (2.17)$$

Where  $f_s$  is the switching frequency. The output voltage ripple for the buck-boost converter is given by (2.18). The ideal voltage gain of buck-boost converter is given by (2.19). For no-ideal converter, the voltage gain equation is given by (2.20) [24].

$$\frac{\Delta V_{O2}}{V_{O2}} = \frac{D_2}{R \times C_2 \times f_s} \quad (2.18)$$

$$\frac{V_{O2}}{V_S} = - \left( \frac{D_2}{1 - D_2} \right) \quad (2.19)$$

$$\frac{V_{O2}}{V_S} = - \left[ \frac{D_2}{D_2'} \times \frac{1}{1 + \frac{r_{L2} + D_2 \times R_{ds3}}{R \times (D_2')^2}} \right] \quad (2.20)$$

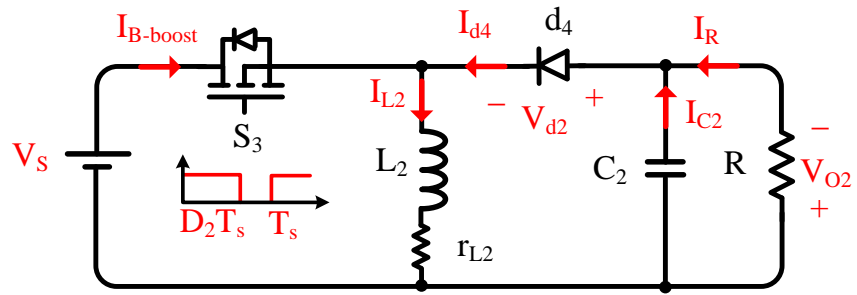
The valid range of  $D_2$  is between ( $0 < D_2 < 1$ ). For ( $D_2 < 0.5$ ), the converter is working in the bucking mode, while if ( $D_2 > 0.5$ ), the converter is working in the boosting mode. Figure 2-7 demonstrates the normalized voltage gain ( $\frac{-V_{O2}}{V_S}$ ) versus duty ratio  $D_2$ . There are an ideal and non-ideal curve. The non-ideal one is due to the non-ideal components such as  $S_3$ ,  $L_2$ , and the diode  $d_4$ . At low duty ratio  $D_2$ , both curves are almost identical. However, for  $D_2 > 0.85$ , the practical voltage transformed curve begins to deviate. For  $D_2 = 1$ , there is no power transfer.

For the proposed hybrid step-up DC-DC converter, the voltage gain is going to be the sum of both converter voltages ( $V_{O1} + V_{O2}$ ) assuming the converter is working in the continuous conduction mode, non-ideal case. For the upper converter (boos), according to equation (2.13), the output voltage for this upper converter is given by (2.21).

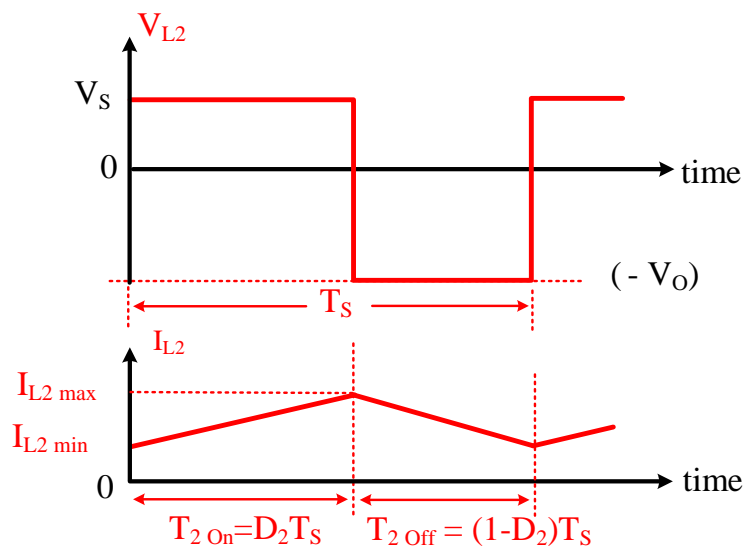
$$V_{O1} = \frac{V_O}{2} = \left[ \frac{V_S}{D_1'} \times \frac{1}{1 + \frac{r_{L1} + D_1 \times R_{ds1}}{R \times (D_1')^2}} \right] \quad (2.21)$$

For the bottom converter (buck-boost), according to equation (2.20), the output voltage for this bottom converter is given by (2.22).

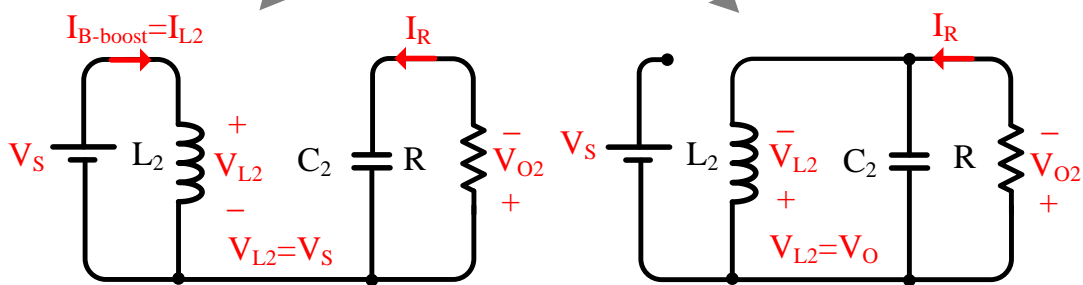
$$V_{O2} = \frac{V_O}{2} = -V_S \left[ \frac{D_2}{D_2'} \times \frac{1}{1 + \frac{r_{L2} + D_2 \times R_{ds3}}{R \times (D_2')^2}} \right] \quad (2.22)$$



(a)



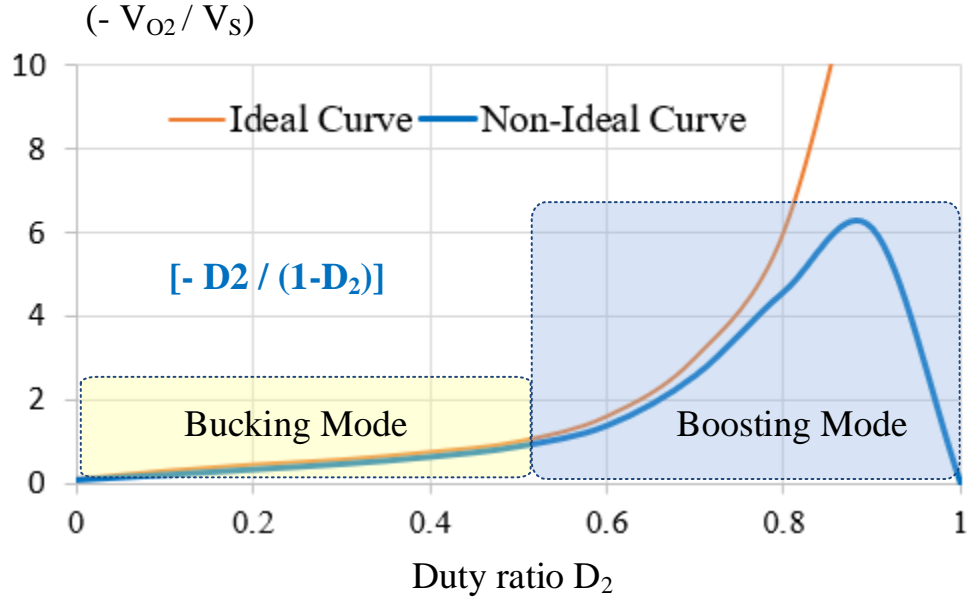
(b)



(c)

(d)

Figure 2-6 (a) Buck-boost converter circuit diagram, (b)  $V_{L2}$  and  $I_{L2}$ , (c) equivalent circuit when  $S_3$  is turned on, (d) equivalent circuit when  $S_3$  is turned off.



**Figure 2-7 Buck-boost converter ( $-V_{O2}/V_S$ ) versus the duty ratio  $D_2$  for ideal and non-ideal converter.**

In order to get the overall voltages for both upper and bottom converter, equation (2.21) and (2.22) should be added up as given by (2.23).

$$V_O = V_S \left[ \frac{1}{D_1'} \times \frac{1}{1 + \frac{r_{L1} + D_1 \times R_{ds1}}{R \times (D_1')^2}} \right] + V_S \left[ \frac{D_2}{D_2'} \times \frac{1}{1 + \frac{r_{L2} + D_2 \times R_{ds3}}{R \times (D_2')^2}} \right] \quad (2.23)$$

Therefore, the non-ideal overall voltage gain for the proposed hybrid step-up DC-DC converter is given by (2.24). Table 2-1 explains the switches ( $S_1, S_2, S_3, S_4$ ) voltage ratings. ( $S_1, S_2$ ) maybe not gated at all since they already have the body diode to conduct current, or they can be used for the synchronous operation to reduce the power losses.

$$\frac{V_o}{V_s} = \left[ \frac{1}{D_1'} \times \frac{1}{1 + \frac{r_{L1} + D_1 \times R_{ds1}}{R \times (D_1')^2}} \right] + \left[ \frac{D_2}{D_2'} \times \frac{1}{1 + \frac{r_{L2} + D_2 \times R_{ds3}}{R \times (D_2')^2}} \right] \quad (2.24)$$

Since all the switches have body diode (anti-parallel diode), then for the same input and output voltage polarities the current bidirectional, hence the power bidirectional, which means this converter has bidirectional power flow capability.

**Table 2-1 Voltage ratings for (S<sub>1</sub>, S<sub>2</sub>, S<sub>3</sub>, S<sub>4</sub>) of the proposed hybrid step-up DC-DC converter.**

Upper converter (boos) S <sub>1</sub> , S <sub>2</sub> voltage ratings			
Switch	Status	Blocking voltage for V <sub>S1</sub>	Blocking voltage for V <sub>S1</sub>
S <sub>1</sub>	ON	-	$\frac{V_o}{2}$
S <sub>2</sub>	OFF		
S <sub>1</sub>	OFF	$\frac{V_o}{2}$	-
S <sub>2</sub>	ON		
Lower converter (buck-boos) S <sub>3</sub> , S <sub>4</sub> voltage ratings			
Switch	Status	Blocking voltage for V <sub>S3</sub>	Blocking voltage for V <sub>S4</sub>
S <sub>3</sub>	ON	-	$V_s + \frac{V_o}{2}$
S <sub>4</sub>	OFF		
S <sub>3</sub>	OFF	$V_s + \frac{V_o}{2}$	-
S <sub>4</sub>	ON		

### 2.2.2. 12-pulse SCR Converter

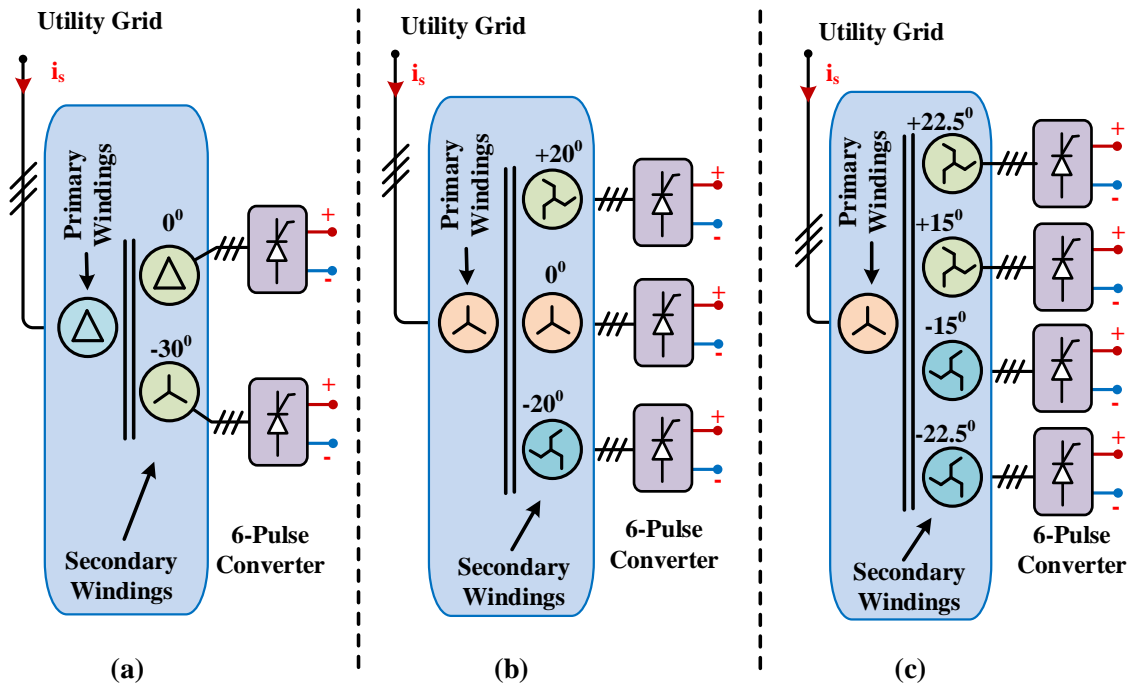
Figure 2-2 demonstrates the 12-pulse scheme of the SCR converter using a zig-zag phase-shift transformer. The input current harmonics depend on the number of pulses. For the six-pulse SCR converter, the input utility current quality is poor because it contains low order harmonics, e.g. (5<sup>th</sup>, 7<sup>th</sup>). For the 12-pulse converter, the input utility current has better quality than the six-pulse converter due to the elimination of the aforementioned harmonics. Generally, the higher the number of pulses, the better input current quality as given by (2.25). Where N is an integer number, P is the number of pulses, and h is the harmonics order. Usually, 12-pulse, 18-pulse converter is widely used in the industrial for the motor drive applications [25].

$$h = N \times P \pm 1 \quad (2.25)$$

### 2.2.3. Phase-shift Line Frequency (50/60) Hz Transformer

In the multi-pulse converter, a proper net phase-shift should be generated for each six-pulse, and that could be created using a multi secondary windings phase-shift transformer. For a 12-pulse converter, there should be a (30<sup>o</sup>) phase-shift between the secondary and tertiary sides, as shown in Figure 2-2. For the 18-pulse converter, the net phase-shift for the secondary sides should be as follows (-20<sup>o</sup>, 0<sup>o</sup>, +20<sup>o</sup>) with respect to the primary side. In the case of 24-pulse converter, the secondary sides transformer should have (-22.5<sup>o</sup>, -15<sup>o</sup>, +15<sup>o</sup>, +22.5<sup>o</sup>) with respect to the primary side, as shown in Figure (2-8). The higher the number of pulses, the better input current quality ( $i_s$ ) (see Figure 2-8).



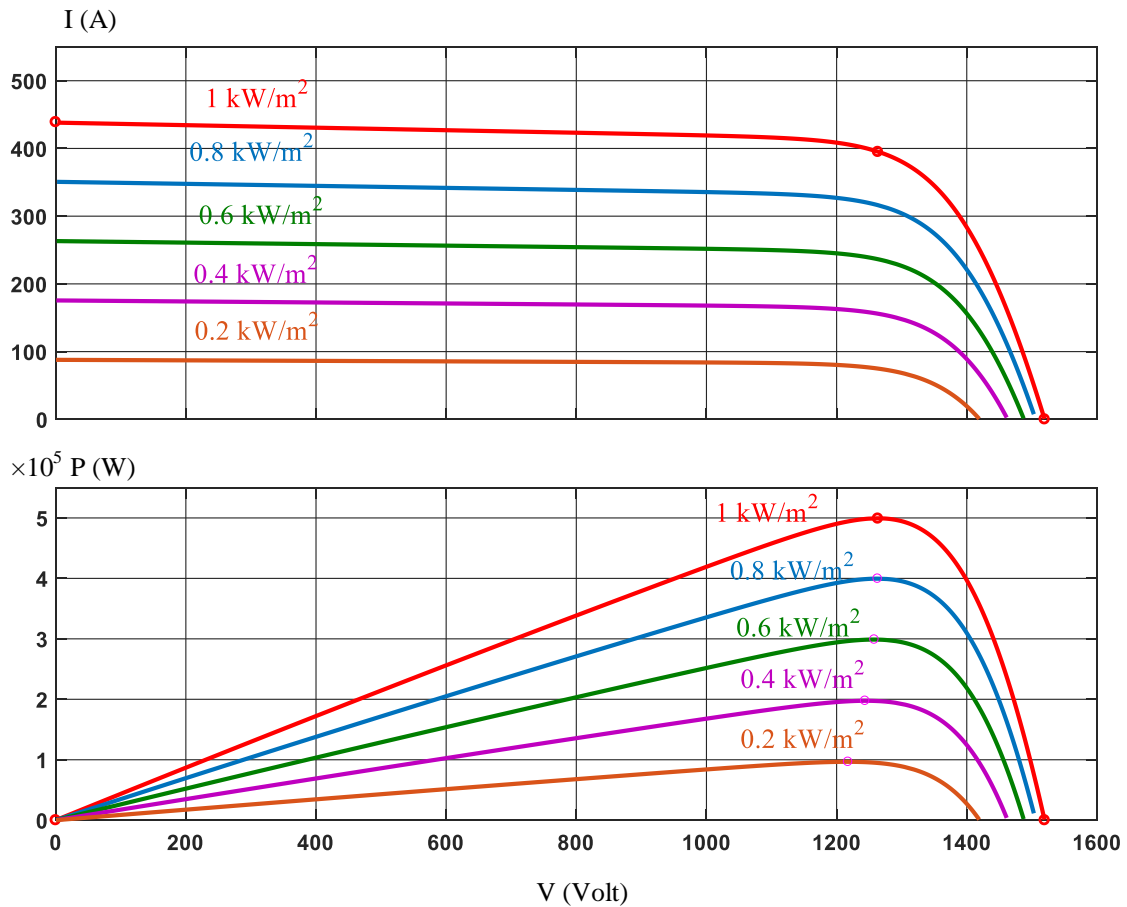


**Figure 2-8 Multi-secondary windings phase-shift transformer for multi-pulse SCR converter (a) 12-pulse SCR converter, (b) 18-pulse SCR converter, (c) 24-pulse SCR converter.**

However, increasing the number of pulses would be required a bigger transformer, which results to increase the cost and reduce the power density of the overall converter.

### 2.3. Simulation Results for the Proposed Topology

The parameters of the presented topology in Figure 2-2 are listed in Table 2-2. A study designed example would be discussed in details using MATLAB software to verify the presented concept. Utility grid voltage  $V_{LL,rms}=2.85$  kV. For the PV farm, an American Solar Wholesale ASW-260M PV panel model is selected involving 35 series panels and



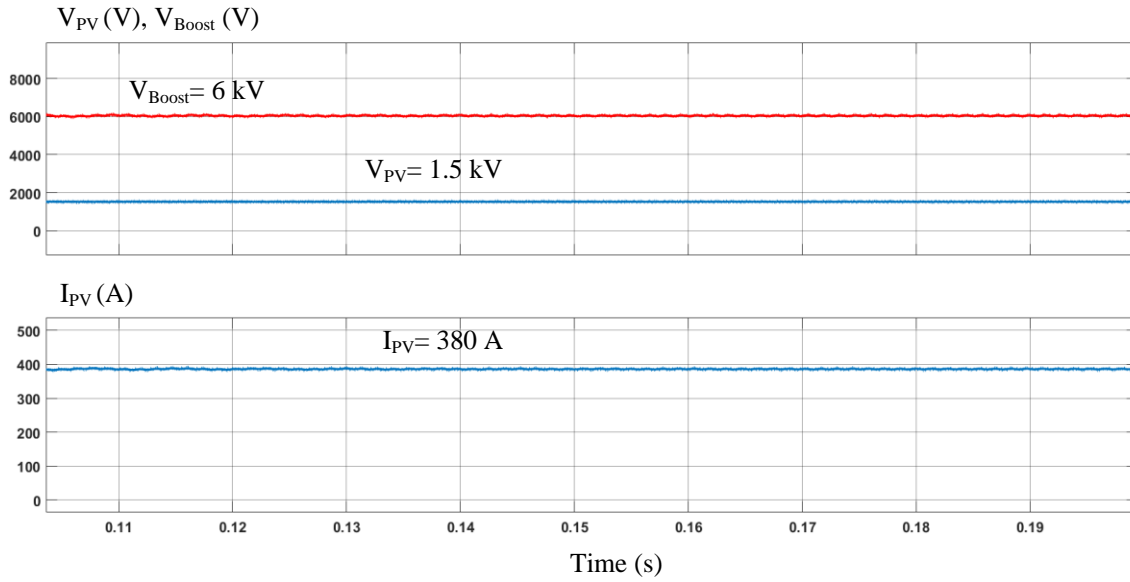
**Figure 2-9 IV and PV characteristics for different sun irradiance levels for the designed PV farm 1.5 kV, 0.5 MW. Array type: American Solar Wholesale ASW-260M; 35 series modules; 55 parallel strings.**

55 parallel strings to build 0.5 MW, 1.5 kV PV plant. The IV and PV characteristics are shown in Figure 2-9. For simplicity, a 12-pulse SCR converter is chosen with a firing angle ( $\alpha = 165^\circ$ ). Figure 2-10 shows the voltage of  $V_{PV}$  farm, the output voltage of the hybrid step-up DC-DC converter  $V_{Boost}$  and current  $I_{PV}$ . The output voltage for each six-pulse ( $V_{dc1}$ ,  $V_{dc2}$ ), and 12-pulse ( $V_{dc12-pulse}$ ) are shown in Figure 2-11. Figure 2-12 shows phase “a” secondary current ( $i_{a-Secondary}$ ), tertiary current ( $i_{a-Tertiary}$ ) and primary current of

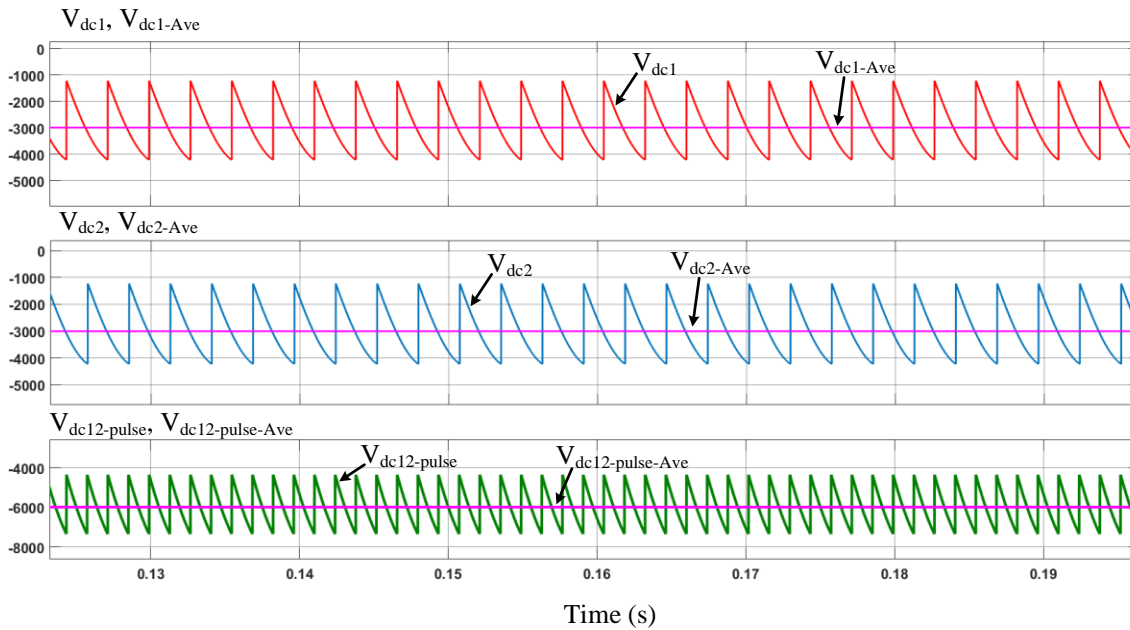
the multi-windings zig-zag transformer ( $i_a$ ). Figure 2-13 demonstrates the utility voltages ( $V_{ab}$ ,  $V_{bc}$ ,  $V_{ca}$ ) along with the overall unfiltered input currents ( $i_a$ ,  $i_b$ ,  $i_c$ ). It is evident that this topology working in the inversion mode since the input utility voltages and currents are out of phase, which means the power flows from the PV farm side to the utility grid side. The FFT analysis for the ( $i_{a-Secondary}$ ) is illustrated in Figure 2-14. As expected, the secondary current side ( $i_{a-Secondary}$ ) has the low order harmonics ( $5^{th}$ ,  $7^{th}$ ) for one of the six-pulse SCR converter. However, the overall unfiltered input current ( $i_a$ ) does not have these low order harmonics, as shown in Figure (2-15). Furthermore, the ( $17^{th}$ ,  $19^{th}$ ) are eliminated too.

**Table 2-2 Design example parameters for 12-pulse SCR converter using the proposed hybrid step-up DC-DC converter.**

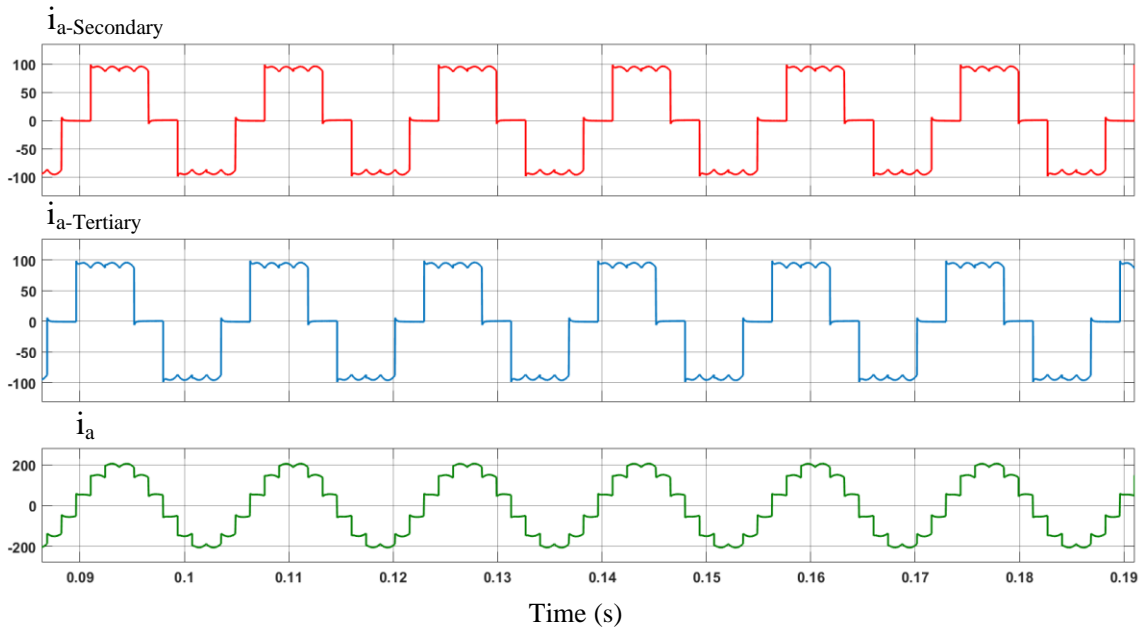
PV Plant parameters	
Module type	American Solae Wholesale ASW-260
Number of series panels=35	Number of parallel strings=55
PV Generated power=0.5 MW	$V_{PV} = 1.5$ kV
Utility grid voltage= 2.85 kV	Utility grid frequency=60 Hz
SCR parameters for 12-pulse converter	
SCR switching frequency= 60 Hz	$\alpha = 165^\circ$ , $L_d=15$ mH
Hybrid step-up DC-DC converter	
$C_1=100$ uF, $L_1=150$ uH	$C_2=100$ uF, $L_2=150$ uH
$V_{in}=1500$ V	$V_{out}=6000$ V
Switching frequency 10 kHz	$D_1=0.5$ , $D_2=0.667$



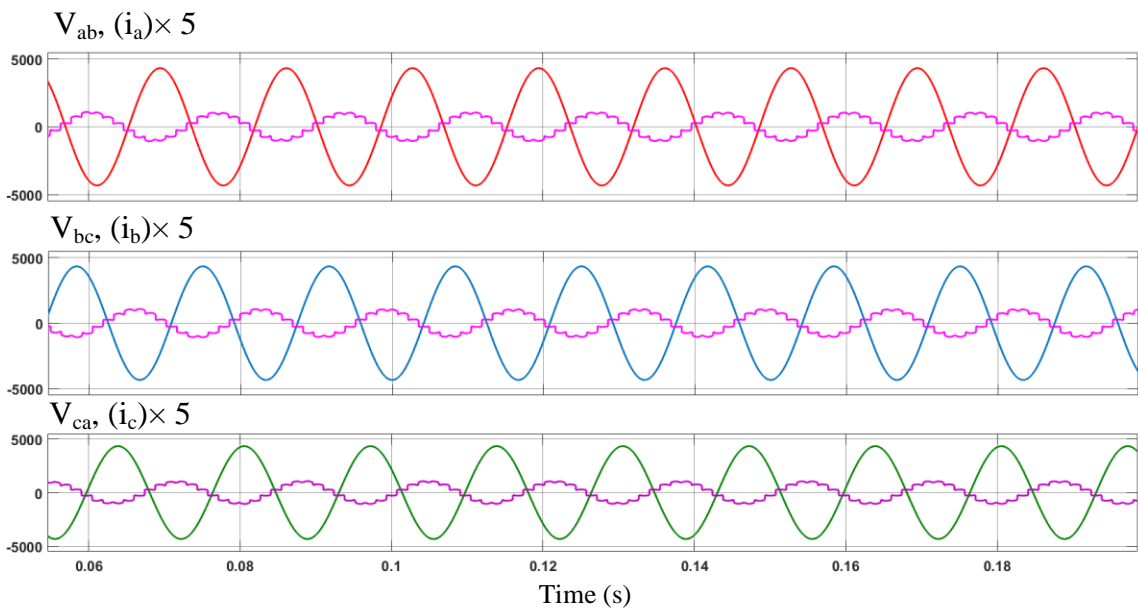
**Figure 2-10 PV plant voltage  $V_{PV}=1.5 \text{ kV}$ , proposed hybrid step-up DC-DC converter voltage  $V_{Boost}=6 \text{ kV}$ , and PV plant current  $I_{PV}=380 \text{ A}$ .**



**Figure 2-11 First six-pulse SCR converter voltage ( $V_{dc1}, V_{dc1-Ave}$ ), second six-pulse SCR converter voltage ( $V_{dc2}, V_{dc2-Ave}$ ), 12-pulse SCR converter voltage ( $V_{dc12-pulse}, V_{dc12-pulse-Ave}$ )**



**Figure 2-12** Phase “a” secondary side transformer current ( $i_{a\text{-Secondary}}$ ), tertiary side transformer current ( $i_{a\text{-Tertiary}}$ ), and overall unfiltered input primary current ( $i_a$ ).



**Figure 2-13** Utility voltages ( $V_{ab}$ ,  $V_{bc}$ ,  $V_{ca}$ ) along with unfiltered utility input currents ( $i_a$ ,  $i_b$ ,  $i_c$ ). Note the currents have been multiplied by 5 for better resolution.

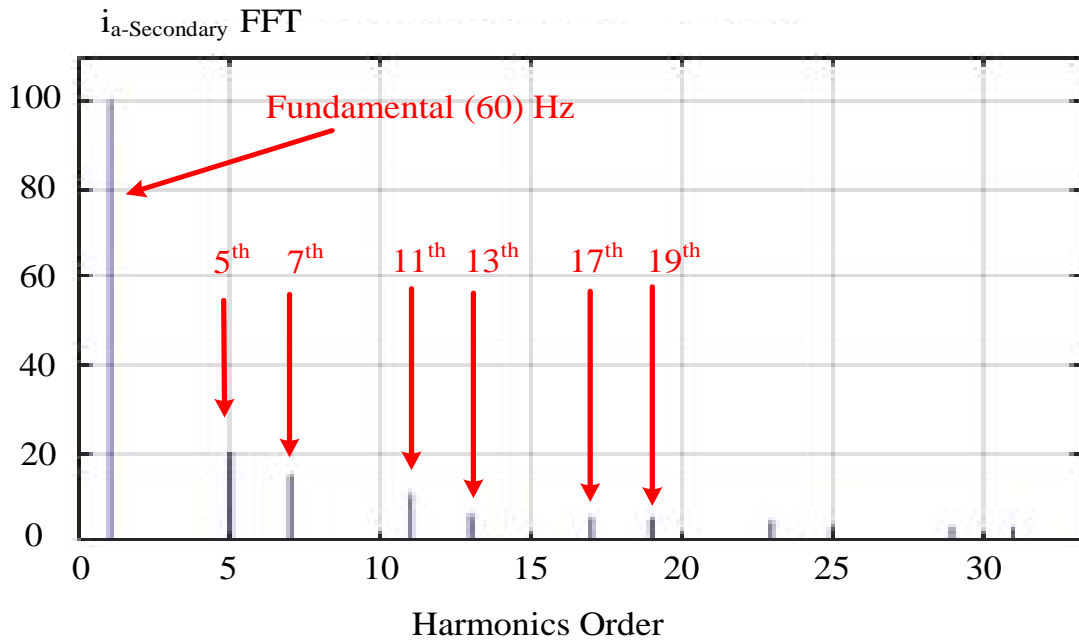


Figure 2-14 FFT analysis of phase “a” secondary transformer current ( $i_{a\text{-Secondary}}$ ).

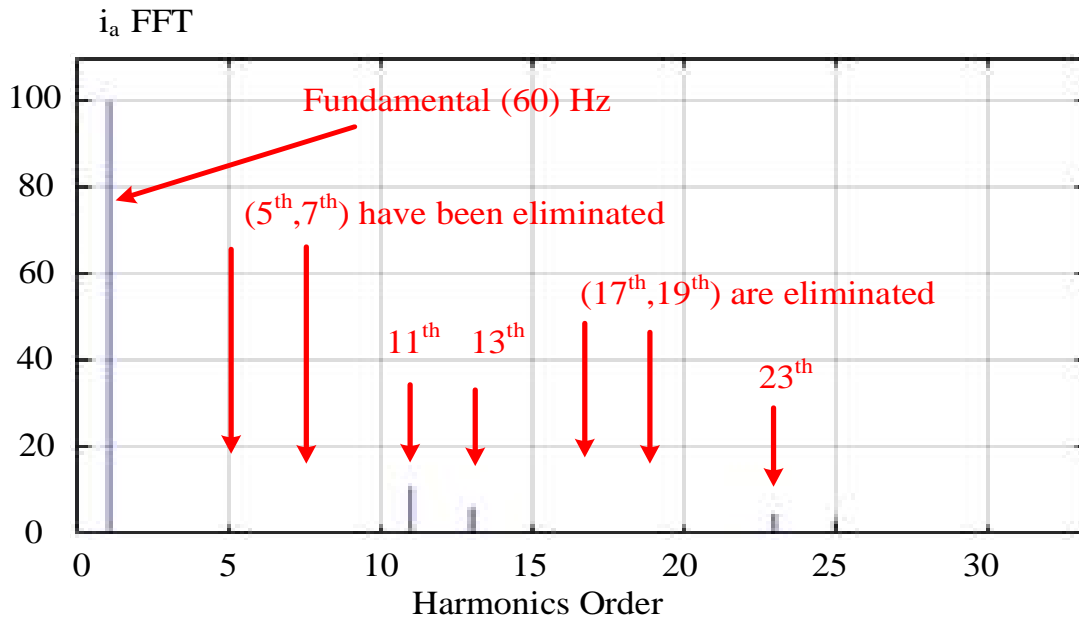


Figure 2-15 FFT analysis of phase “a” unfiltered primary utility current ( $i_a$ ).

## 2.4. Conclusion

This section proposes a medium voltage DC collection grid for large-scale PV power plant using 12-pulse SCR converter and phase-shift line frequency zig-zag transformer. A new hybrid step-up DC-DC converter is proposed to boost the 1500V DC PV plant to 6000V. A detailed design example, simulation results using MATLAB, demonstrate the 12-pulse operation achieving high input power quality by eliminating the low order harmonics of the input utility current, e.g. (5<sup>th</sup>,7<sup>th</sup>). The advantages of the proposed concept are overcoming the limitation of handling high power by using the SCR converter, bidirectional power flow capability, and the output voltage can be regulated by adjusting the firing angle ( $\alpha$ ).

### **3. MEDIUM VOLTAGE DC COLLECTION GRID FOR LARGE-SCALE PV POWER PLANT WITH SCR CONVERTER AND INTEGRATED MEDIUM FREQUENCY SOLID-STATE TRANSFORMER (SST) FOR UTILITY INTERFACE\***

This section proposes a medium voltage MV DC collection grid concept for large-scale PV power plant with a line commutated 12-pulse SCR converter and integrated solid-state transformer SST for utility interface. DC power from the PV power plant section is first processed via a line commutated 12-pulse converter employing an inverter grade SCR's is interfaced to SST powered by a higher frequency AC-AC converter. The objective of this topology is having the SST operate at a medium frequency (360Hz or 720Hz), to reduce the transformer size/weight to 1/3<sup>rd</sup> to 1/5<sup>th</sup>. It is shown due to 12-pulse operation a high-quality utility line current can be achieved with the cancellation of 5<sup>th</sup> and 7<sup>th</sup> harmonic currents. The proposed approach is a robust current fed system, that improves power density, and it is simple to control with an integrated solid-state transformer. Simulation results presented on an example 150 kW PV power plant to validate the concept. Experimental results for a scale down laboratory type 1kW system are also discussed.

---

\* Part of this section is reprinted with permission from:  
©2019 IEEE. S. Sabry, E. I. Pool-Mazun and P. Enjeti, "A Medium Voltage DC Collection Grid for Large Scale PV Power Plant with SCR Converter and Integrated Solid-State Transformer (SST)," 2019 *IEEE Energy Conversion Congress and Exposition (ECCE)*, Baltimore, MD, USA, 2019, pp. 5824-5831.



### 3.1. Introduction

Countries around the globe are accelerating their deployment of renewable energy technologies. In 2014 renewable energy resources provided 23% of global power generation. It is predicted that by 2030 it will increase to 45% according to the International Renewable Energy Agency (IRENA) [26]. The DC collection grid concept has additional benefits than the AC collection [16,27]. In addition to a reduction in size and improvement in efficiency, the DC collection grid also enables the integration of energy storage systems [20,28,29]. Multi-pulse line frequency commutated SCR converters have been widely used for interfacing renewable energy for wind turbine farms [31,32] and solar PV plants (see Figure 3-1) [30]. These systems have been shown to be robust for high power applications [33,34,35]. However, the main disadvantage of these systems is the use of a line frequency (50/60) Hz bulky transformer that has a large footprint for utility interface. In response to these concerns, this section proposes a 12-pulse SCR converter with an integrated medium frequency solid-state transformer. It is shown that by employing inverter grade SCRs and advanced modulation techniques, a transformer operating frequency of 360/720Hz can be realized, reducing the transformer size with simultaneous better control. The advantages of the proposed approach are summarized below:

- 1) The proposed system is current fed, eliminates the need for a dc-link capacitor and the resulting system is more robust.
- 2) The proposed integrated solid-state transformer SST employs lower number of power conversion stages than conventional approaches, contributes to better power density.

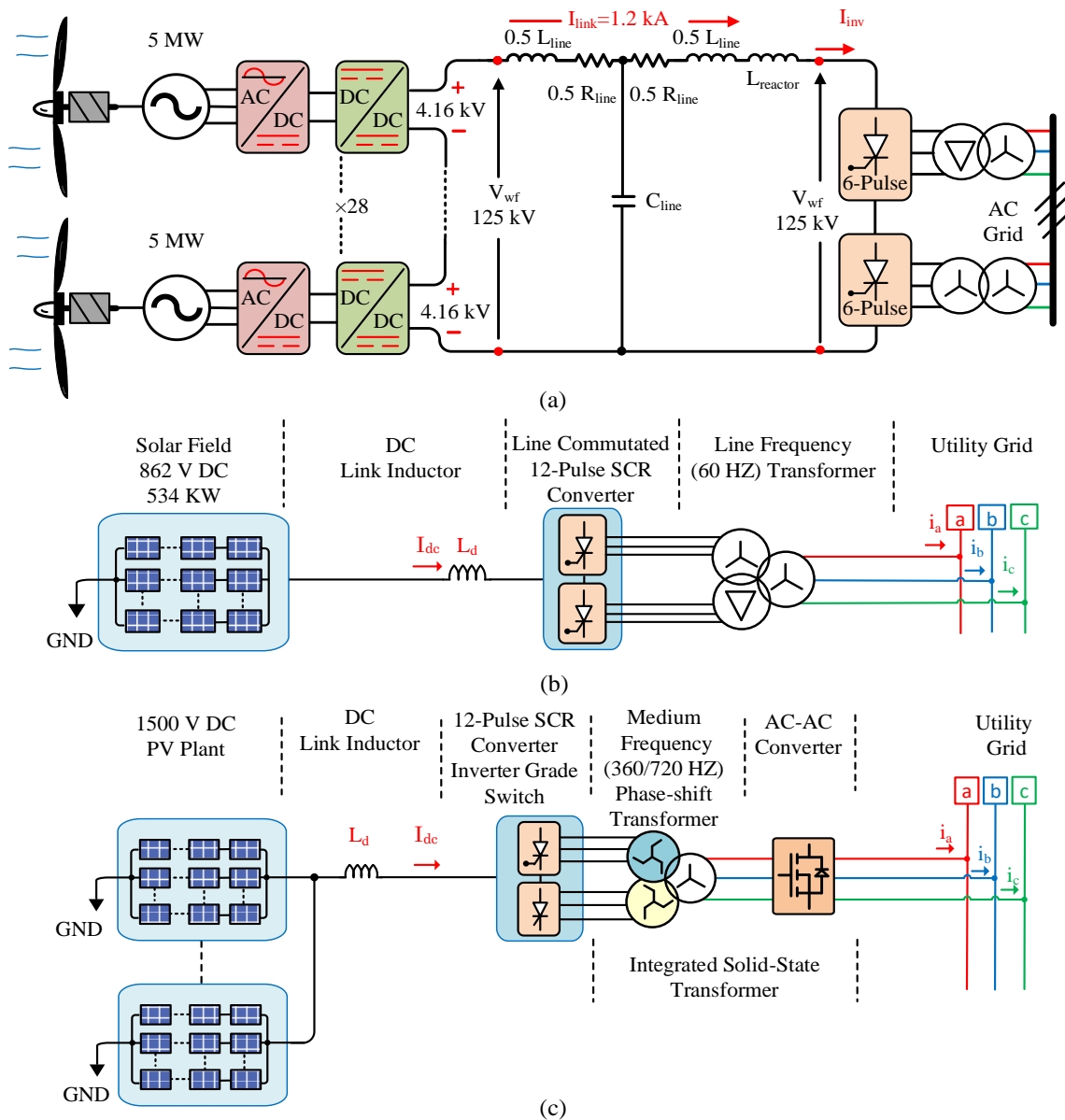
- 3) Lower order harmonics are shown to be eliminated due to 12-pulse operation resulting to improve power quality of the input utility current.
- 4) The presence of AC-AC converter on the AC side is shown to add flexibility to control the input power flow.
- 5) Finally, the proposed system allows for bidirectional power flow and can be easily adapted for interfacing battery energy storage systems to utility.

### **3.2. Proposed Medium Voltage DC Collection Grid for Large-Scale PV Power Plant with SCR Converter and Medium Frequency Solid-State Transformer**

The proposed medium voltage DC collection grid with SCR converter and solid-state transformer is demonstrated in Figure 3-2. The presented topology involves three parts: bidirectional AC-AC converter, medium frequency zig-zag transformer, and 12-pulse SCR converter.

#### **3.2.1. Bidirectional AC-AC Converter**

Figure 3-2 shows the per phase indirect bidirectional AC-AC converter. Each one composes a single phase bridge rectifier, small film capacitor (weak dc-link 10 uF), and full bridge inverter (since the power can be flow in both directions). The input voltage of each converter is line to neutral 60 Hz, and the output voltage is modulated with a medium frequency 720 Hz square wave 50% duty cycle. The mathematical analysis is demonstrated for the phase “a”. The line to neutral 60 Hz input voltage is shown



**Figure 3-1 Evolution of multi-pulse SCR converter for large-scale wind turbine farm and PV plant converter (a) 12-pulse SCR to interface wind farms to a utility grid using line frequency transformer isolation. Adapted from [31], (b) conventional PV power plant with a line commutated 12-Pulse SCR converter. Adapted from [30], (c) block diagram of the proposed medium voltage DC collection grid for large-scale PV power plant with multi-pulse SCR converter and integrated solid-state transformer (see Figure 3-2 for circuit topology). Reprinted with the permission from © 2019 IEEE [36].**

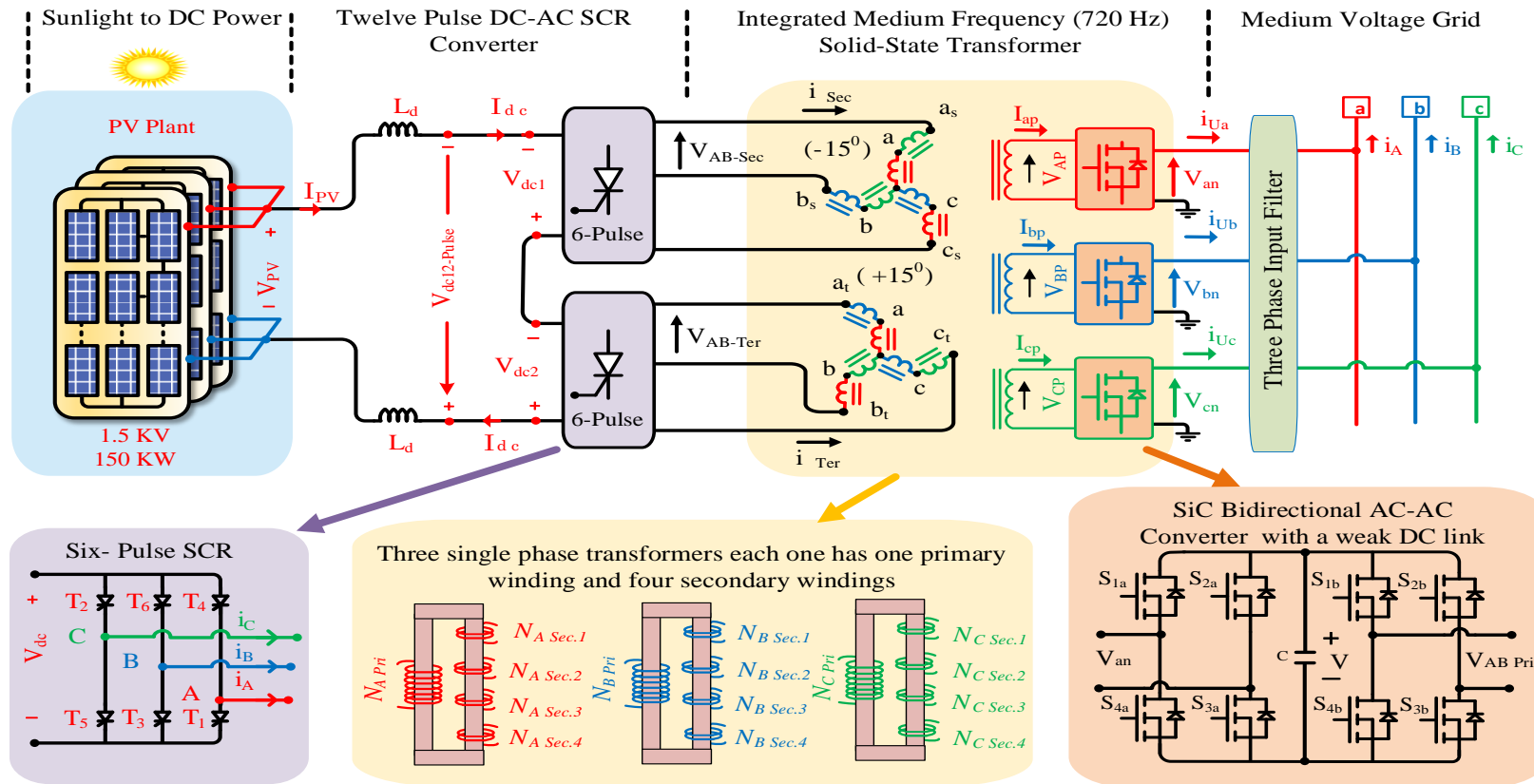
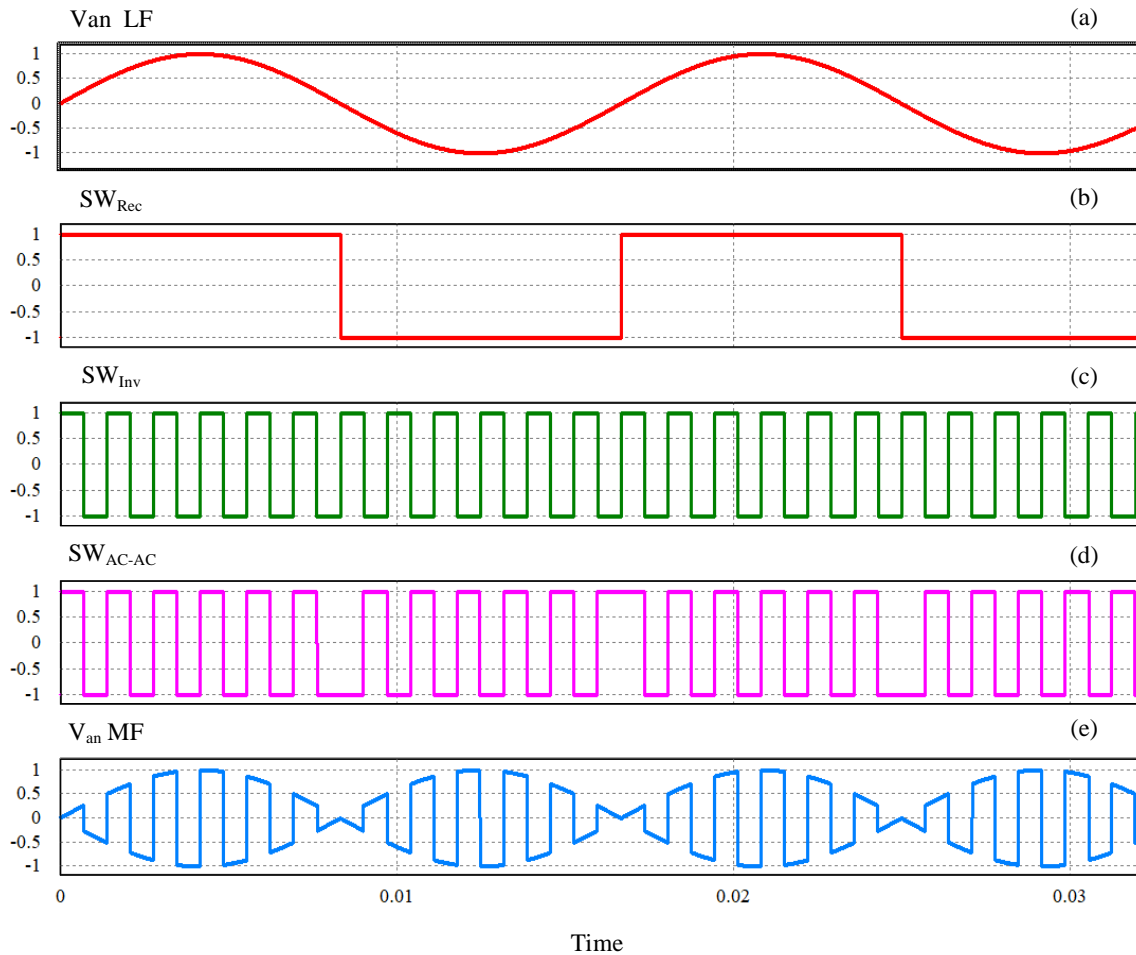


Figure 3-2 Proposed topology of the medium voltage DC collection grid for large-scale PV power plant with SCR converter and integrated medium frequency 720 Hz solid-state transformer. Reprinted with the permission from © 2019 IEEE [36].



**Figure 3-3 Functional operation of bidirectional AC-AC converter (Figure 3-2), (a)  $V_{an}$  line to neutral input voltage 60 Hz, (b) bridge rectifier switching function  $SW_{Rec}$ , (c) Medium frequency 720 Hz square wave 50% duty cycle, (d) AC-AC converter switching function  $SW_{AC-AC}$ , (e) phase “a” AC-AC output voltage  $V_{an}$  MF. Reprinted with the permission from © 2019 IEEE [36].**

in Figure 3-3 (a) and given by (3.1). The switching function of the rectifier bridge  $SW_{Rec}$  60 Hz is shown in Figure 3-3 (b) and given by (3.2). The switching function for the inverter bridge  $SW_{Inv}$  720 Hz square wave is shown in Figure 3-3 (c) and given by (3.3). The overall switching function for the AC-AC converter  $SW_{AC-AC}$  is shown in Figure 3-3 (d) and given by (3.4) [36]. The medium frequency output voltage of the

$$V_{an} = \sin(\omega_s \cdot t) \quad V \quad (3.1)$$

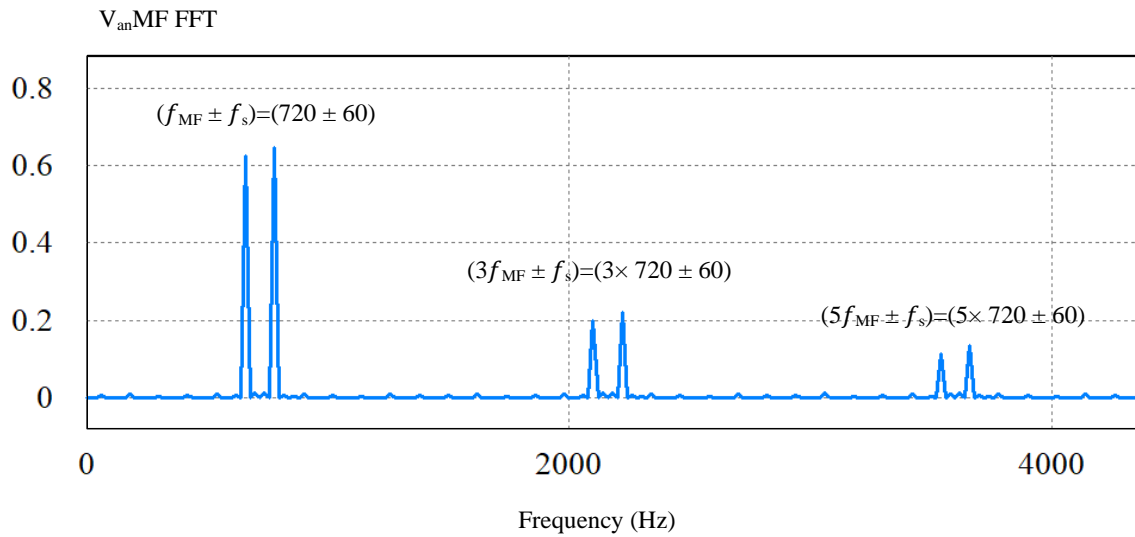
$$SW_{Rec} = \frac{4}{\pi} \sum_{n=1,3,5,\dots}^{\infty} \frac{1}{n} \sin(n \cdot \omega_s \cdot t) \quad (3.2)$$

$$SW_{Inv} = \sum_{n=1,3,5,\dots}^{\infty} \frac{1}{n} \sin(n \cdot \omega_{MF} \cdot t) \quad (3.3)$$

$$\begin{aligned} SW_{AC-AC} &= SW_{Rec} \times SW_{Inv} \\ &= \frac{4}{\pi} \sum_{n=1,3,5,\dots}^{\infty} \frac{1}{n} \sin(n \cdot \pi \cdot D) \cdot \sin(n \cdot \omega_{MF} \cdot t) \end{aligned} \quad (3.4)$$

$$V_{anMF} = \left[ \begin{array}{l} [0.636 \sin(\omega_{MF} \pm \omega_s)t + \quad 0.192 \sin(3\omega_{MF} \pm \omega_s)t +] \\ [0.106 \sin(5\omega_{MF} \pm \omega_s)t + \quad \text{High Order Terms}] \end{array} \right] \quad (3.5)$$

AC-AC converter  $V_{anMF}$  is shown in Figure 3-3 (e) and given by (3.5). The frequency spectrum FFT of  $V_{anMF}$  is shown in Figure 3-4. It is clear that the medium frequency output voltage has frequency components  $(\omega_{MF} \pm \omega_s)$ ,  $(3\omega_{MF} \pm \omega_s)$ ,  $(5\omega_{MF} \pm \omega_s)$ . Evidently, SST transformer's primary voltage  $V_{anMF}$  has a dominant frequency around 720 Hz that allowed the transformer to operate at the medium frequency range. Series stacks of AC-AC converter can be used for high voltage levels. The function of this converter is to generate a medium frequency voltage 720 Hz at the primary windings of the medium frequency transformer and allow the power to flow in both directions [36].



**Figure 3-4 FFT spectrum analysis for the phase “a” AC-AC converter output voltage  $V_{an}$  MF.**

For the phase “b” and “c”, the AC-AC converter output voltages are going to be the same, except they are shifted by 120 degree respectively.

### 3.2.2. Medium Frequency Zig-Zag Phase-Shift Transformer

The second part of the presented topology is the medium frequency SST. As shown in Figure 3-2, the primary side of this transformer is a star connected while the secondary side consists of a group that has 4 windings per phase. The secondary and tertiary side of this transformer has been connected in a zig-zag scheme to create a net ( $30^0$ ) between them (refer to Figure 3-2). In other words, this transformer has two sets of zig-zag connections. Each secondary side is connected to a six-pulse SCR converter. The secondary of the zig-zag connections creates a set of three phase voltages with a ( $-15^0$ ) phase difference with respect to the input primary side voltages. The tertiary side creates another set of three phase voltages with a ( $+15^0$ ) with respect to the input primary side

voltages. The phase-shift between the secondary and tertiary sides is  $(30^\circ)$  to perform the 12-pulse operation of SCR converter [36]. A phasor diagram of the zig-zag connection is shown in Figure 3-5. The primary side shows the line-to-line voltages forming an equilateral triangle.  $V_{an}$ ,  $V_{bn}$  and  $V_{cn}$  are the reference voltages as expressed in equations (3.6-3.8). The line-to-line voltages phasor expressions for  $V_{ab}$ ,  $V_{bc}$  and  $V_{ca}$  are given by (3.9-3.11)

$$V_{an} = \sqrt{2} V_{ph (rms)} \angle 0^\circ \quad (3.6)$$

$$V_{bn} = \sqrt{2} V_{ph (rms)} \angle -120^\circ \quad (3.7)$$

$$V_{cn} = \sqrt{2} V_{ph (rms)} \angle +120^\circ \quad (3.8)$$

$$V_{ab} = \sqrt{3} \sqrt{2} V_{ph (rms)} \angle +30^\circ \quad (3.9)$$

$$V_{bc} = \sqrt{3} \sqrt{2} V_{ph (rms)} \angle -90^\circ \quad (3.10)$$

$$V_{ca} = \sqrt{3} \sqrt{2} V_{ph (rms)} \angle +90^\circ \quad (3.11)$$

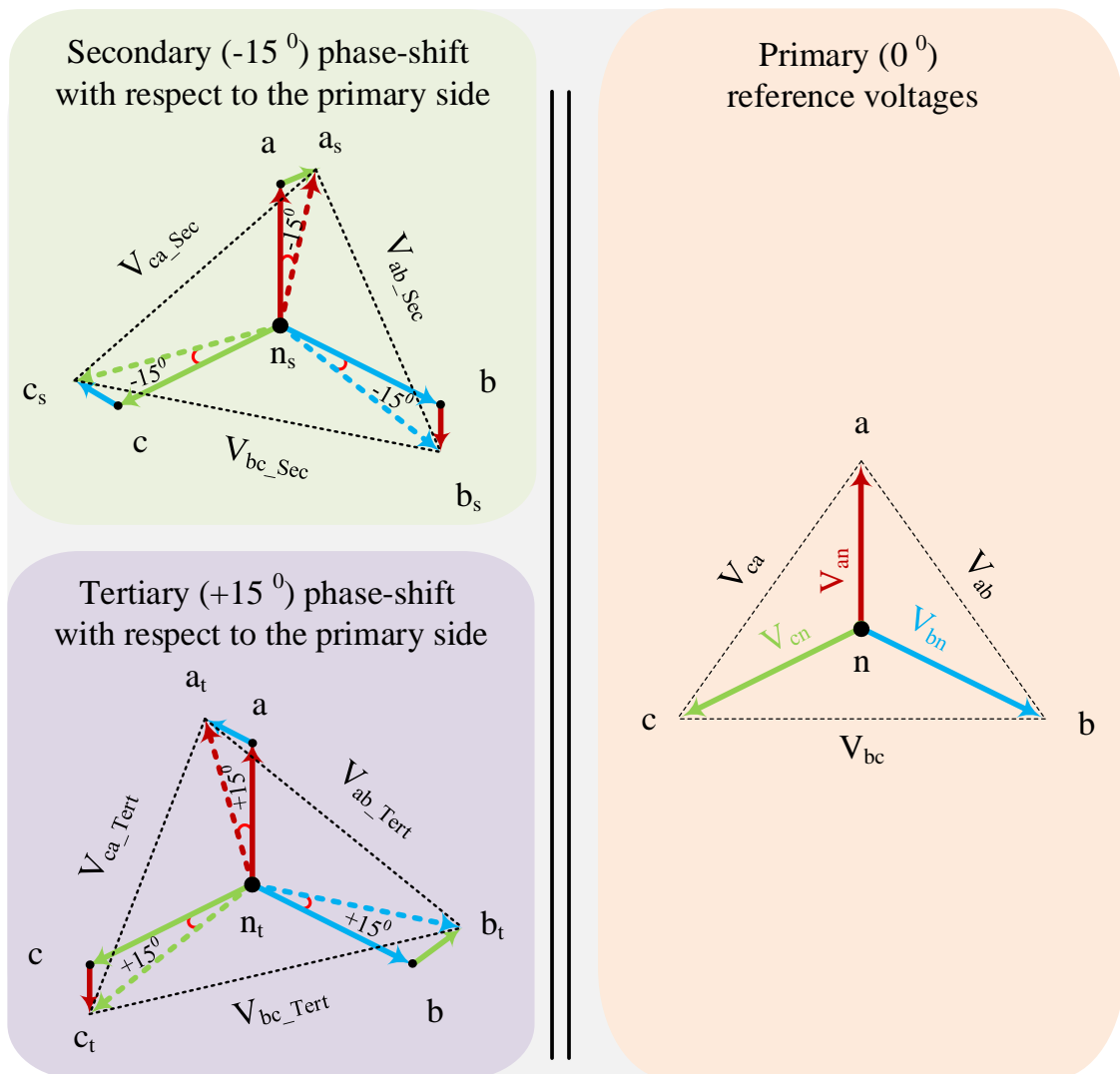
The turns ratio of these windings can be found by solving equation (3.12) and (3.13) breaking them into their real and imaginary parts yields two systems of two equations and two unknowns. Solving them gives the desired turns ratio as, expressed by (3.14) [36].

$$V_{as} = N_{s1} \cdot V_{an} - N_{s2} \cdot V_{cn} = N_{s1} \angle 0^\circ - N_{s2} \angle 120^\circ = 1 \angle -15^\circ \quad (3.12)$$

$$V_{at} = N_{s3} \cdot V_{an} - N_{s4} \cdot V_{bn} = N_{s3} \angle 0^\circ - N_{s4} \angle -120^\circ = 1 \angle +15^\circ \quad (3.13)$$

$$N_{p1} : N_{p2} : N_{s1} : N_{s2} : N_{s3} : N_{s4} = 1 : 1 : 0.816 : 0.298 : 0.816 : 0.298 \quad (3.14)$$





**Figure 3-5 Phasor diagram of three phase zig-zag phase-shift transformer that has on group star primary windings and two sets of secondary windings to create phase-shift ( $-15^\circ$ ,  $+15^\circ$ ) with respect to the input primary side voltages. Reprinted with the permission from © 2019 IEEE [36].**

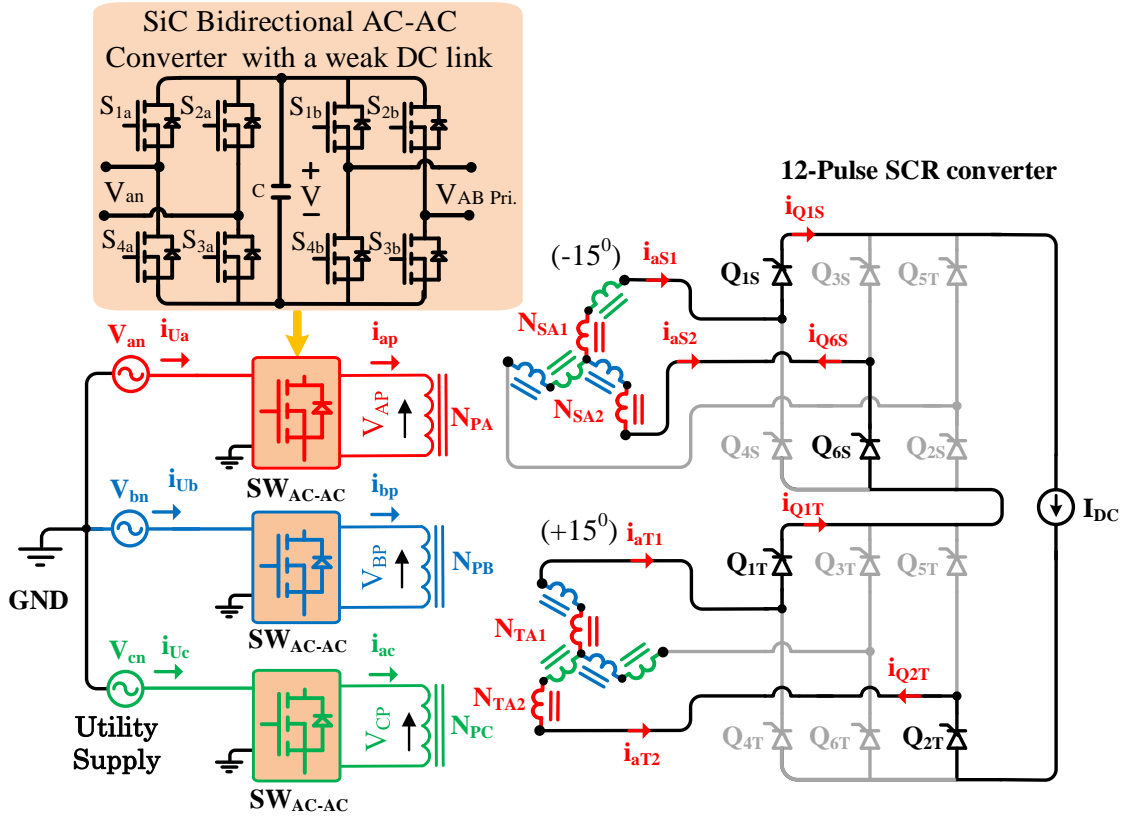
### 3.2.3. 12-pulse SCR Converter

The last part of the presented topology is two groups of six-pulse SCR converters connected in series for multi-pulse operation (see Figure 3-2). The first group has been

connected to the transformer secondary side ( $-15^0$ ), while the second group is connected to the transformer tertiary side ( $+15^0$ ). Each switch SCR should be inverter grade type (i.e. fast turn-off Thyristor) to work at medium frequency range [36]. By firing (gating) the SCR switches at the inversion mode ( $\alpha > \pi/2$ ), the 12-pulse converter works as an inverter. Simple square wave gating signals can be used to run the topology. Using a 12-pulse SCR converter improves the input quality current because the low order harmonics ( $5^{\text{th}}$ ,  $7^{\text{th}}$ ) have been eliminated. Finally, a dc-link inductor  $L_d$  is used to smooth the PV plant current and reduce its ripple.

### 3.3. Input Current Analysis

The low order harmonics ( $5^{\text{th}}$ ,  $7^{\text{th}}$ ) have been removed from the unfiltered utility input currents  $i_{Ua}$ ,  $i_{Ub}$ ,  $i_{Uc}$  by nature of the net  $30^0$  phase-shift zig-zag medium frequency transformer. The analysis shows that this current has the same quality as the conventional line frequency transformer 12-pulse converter. The mathematical analysis proves that the  $i_{Ua}$  dominant harmonics are ( $11^{\text{th}}$ ,  $13^{\text{th}}$  ..etc.). In order to derive the mathematical equation of  $i_{Ua}$ , the output current  $i_{DC}$  is assumed to be pure DC (ripple free), the 12-pulse SCR converter is worked at the rectification mode ( $\alpha=0$ ). The analysis is applied for the phase “a” as shown in Figure 3-6.  $i_{Ua}$  is given by (3.15).  $I_{ap}$  is the phase “a” primary transformer winding current and  $SW_{AC-AC}$  is the overall AC-AC converter switching function that is given by (3.4). To obtain the relationship of  $I_{ap}$  and the secondary side currents of the transformer, volt-ampere balanced between the primary and secondary sides can be used as given by (3.16) [36].



**Figure 3-6** Phase “a” unfiltered input current  $i_{Ua}$  analysis for the proposed topology in Figure 3-2.

$$i_{Ua} = SW_{AC-AC} \times I_{ap} \quad (3.15)$$

$$N_{PA} \cdot I_{ap} = N_{SA1} \cdot I_{aS1} + N_{SA2} \cdot I_{aS2} + N_{TA1} \cdot I_{aT1} + N_{TA2} \cdot I_{aT2} \quad (3.16)$$

$$I_{aS1} = I_{Q1S} \quad (3.17)$$

$$I_{aS2} = -I_{Q6S} \quad (3.18)$$

$$I_{aT1} = I_{Q1T} \quad (3.19)$$

$$I_{aT2} = -I_{Q2T} \quad (3.20)$$

Substituting equations (3.17-3.20) into equation (3.16) yields:

$$I_{ap} = N_{SA1}(I_{Q1S} + I_{Q1T}) - N_{TA1}(I_{Q6S} + I_{Q2T}) \quad (3.21)$$

The output current of 12-pulse SCR converter  $I_{DC}$  that goes through ( $I_{Q1S}, I_{Q6S}, I_{Q1T}, I_{Q2T}$ ) creates a quasi-square wave shape at the primary current  $i_{ap}$ . The  $i_{ap}$  has a switching function  $S_q$  is given by (3.22). However, this current has to react with the overall switching function of the AC-AC converter  $SW_{AC-AC}$  which is given by (3.4).

$$S_q(\omega_s t) = \sum_{n=1,3,5,7,\dots}^{\infty} \left[ \frac{4 I_{DC}}{n\pi} \cos\left(\frac{n\pi}{6}\right) \right] \cdot \sin(n \cdot \omega_s \cdot t) \quad (3.22)$$

Due to the effect of the  $SW_{AC-AC}$ , the currents of the SCR switches become

$$I_{Q1S} = SW_{AC-AC} \times S_q\left(\omega_s \cdot t - \frac{\pi}{12}\right) \quad (3.23)$$

$$I_{Q6S} = SW_{AC-AC} \times S_q\left(\omega_s \cdot t - \frac{\pi}{12} - \frac{2\pi}{3}\right) \quad (3.24)$$

$$I_{Q1T} = SW_{AC-AC} \times S_q\left(\omega_s \cdot t + \frac{\pi}{12}\right) \quad (3.25)$$

$$I_{Q2T} = SW_{AC-AC} \times S_q\left(\omega_s \cdot t + \frac{\pi}{12} + \frac{2\pi}{3}\right) \quad (3.26)$$

Evidently, equations (3.23) and (3.25) prove that there is a ( $30^0$ ) phase-shift between the secondary and the tertiary side for the 12-pulse operation. Plugging equations (3.23-3.26) into equation (3.21) results:

$$I_{ap} = \left[ \begin{array}{c} N_{SA1} \left[ S_q\left(\omega_s \cdot t - \frac{\pi}{12}\right) + S_q\left(\omega_s \cdot t + \frac{\pi}{12}\right) \right] - \\ N_{TA1} \left[ S_q\left(\omega_s \cdot t - \frac{\pi}{12} - \frac{2\pi}{3}\right) + S_q\left(\omega_s \cdot t + \frac{\pi}{12} + \frac{2\pi}{3}\right) \right] \end{array} \right] \times SW_{AC-AC} \quad (3.27)$$

Plugging equation (3.27) into (3.15) to find the overall unfiltered phase “a” utility current  $i_{Ua}$  that is given by (3.28).

$$i_{Ua} = \left[ \begin{array}{l} N_{SA1} \left[ S_q \left( \omega_s \cdot t - \frac{\pi}{12} \right) + S_q \left( \omega_s \cdot t + \frac{\pi}{12} \right) \right] - \\ N_{TA1} \left[ S_q \left( \omega_s \cdot t - \frac{\pi}{12} - \frac{2\pi}{3} \right) + S_q \left( \omega_s \cdot t + \frac{\pi}{12} + \frac{2\pi}{3} \right) \right] \end{array} \right] \times [SW_{AC-AC}]^2 \quad (3.28)$$

Simplifying the equation further yields to:

$$i_{Ua} = \frac{4\sqrt{3} I_{DC}}{\pi} \left[ \begin{array}{l} \sin(\omega_s \cdot t) \quad - \frac{1}{11} \sin(11 \cdot \omega_s \cdot t) \\ - \frac{1}{13} \sin(13 \cdot \omega_s \cdot t) \quad + \frac{1}{23} \sin(23 \cdot \omega_s \cdot t) \\ + \quad \text{High Order Terms} \end{array} \right] \times [SW_{AC-AC}]^2 \quad (3.29)$$

For (D=0.5),

$$[SW_{AC-AC}]^2 = \left[ \frac{4}{\pi} \sum_{n=1,3,5,7,\dots}^{\infty} \frac{1}{n} \sin(n \cdot \pi \cdot D) \cdot \sin(n \cdot \omega_{HF} \cdot t) \right]^2 = 1 \quad (3.30)$$

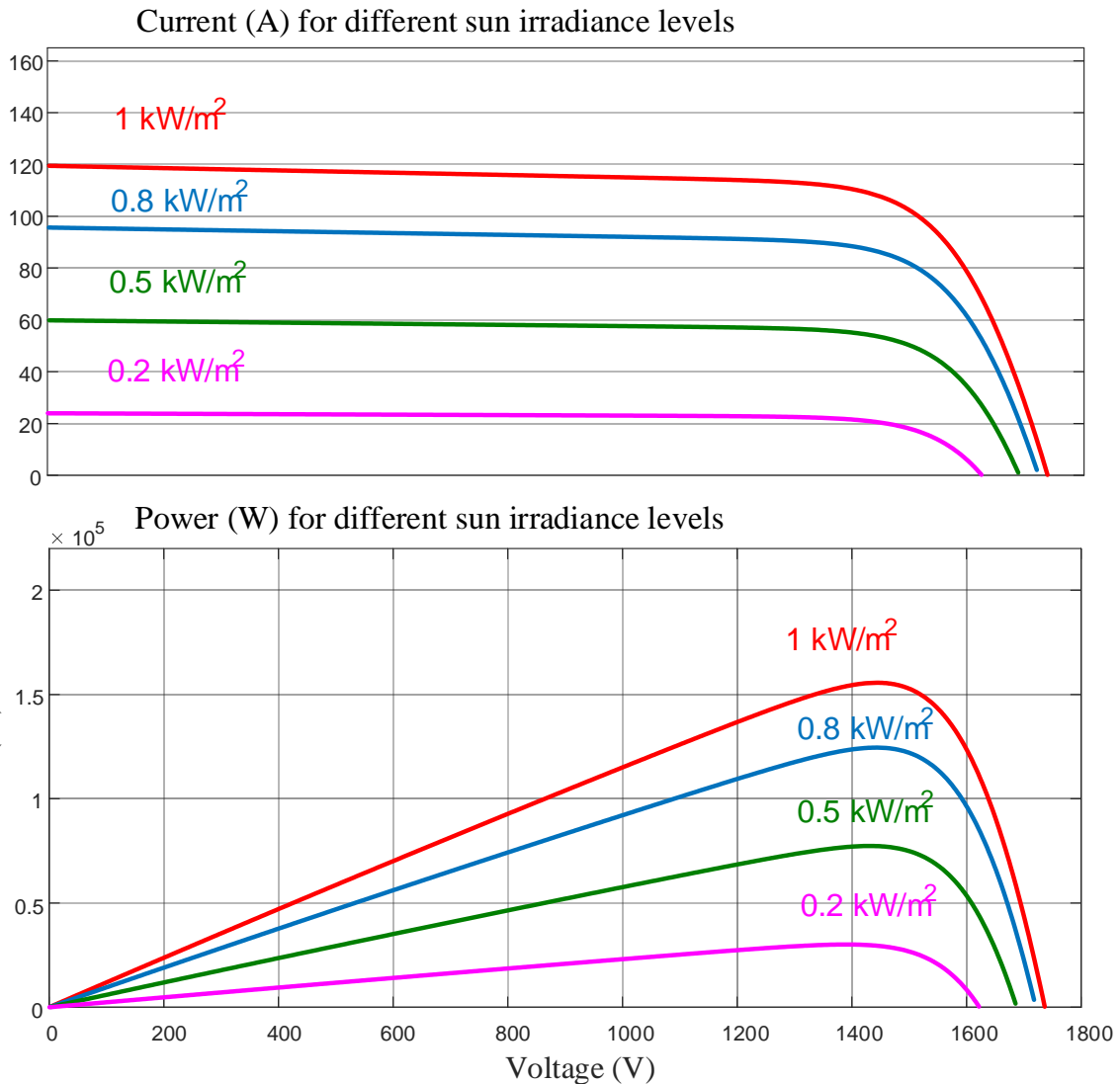
Then the unfiltered utility current for phase “a”  $i_{Ua}$  becomes:

$$i_{Ua} = \frac{4\sqrt{3} I_{DC}}{\pi} \left[ \begin{array}{l} \sin(\omega_s \cdot t) - \frac{1}{11} \sin(11 \cdot \omega_s \cdot t) \\ - \frac{1}{13} \sin(13 \cdot \omega_s \cdot t) \quad + \frac{1}{23} \sin(23 \cdot \omega_s \cdot t) \\ + \quad \text{High Order Terms} \end{array} \right] \quad (3.31)$$

Evidently, equation (3.31) proves that the unfiltered utility current  $i_{Ua}$  has the same performance of the conventional 12-pulse SCR converter by eliminating the unwanted low order harmonics (5<sup>th</sup>, 7<sup>th</sup>). The math derivation proves that the presented topology has a good performance utility input current. For ( $\alpha \neq 0$ ), there will be zero states produce at the DC side ( $2f_{MH}, 4f_{MH}, 6f_{MH} \dots$  etc.) These frequency components interact with the fundamental frequency and low order harmonics of the unfiltered utility input current ( $f_s, 11f_s, 13f_s \dots$  etc.) Since the switching frequency is ( $f_{MH} = 720$  Hz), changing the firing angle  $\alpha$  will create harmonics at higher frequencies and keep the low order harmonics intact. This implies regulating the output voltage by adjusting the firing angle won't affect the input current performance. Theoretical THD of the input utility current is (17%) which is the same as for the conventional 12-pulse SCR converter.

### 3.4. Design Example

A medium voltage 2300 V<sub>LL rms</sub>, 150 kW, 1500 V dc design example is considered to study the feasibility of the proposed concept, as shown in Figure 3-2. In order to run the SCR converter in the inversion region, the firing angle should be greater than 90° ( $\alpha=160^\circ$ ). An American solar wholesale ASW-260M PV model is selected with 40 series models and 15 parallel strings to generate the V<sub>PV</sub>=1.5 kV, I<sub>PV</sub>=100 A, 150 kW PV plant. Figure 3-7 shows the IV and PV plant characteristics for different sun irradiancies levels. For the medium frequency phase-shift SST, the volt-ampere rating can be found using the rms voltage and rms current under the assumption that the output current has ripple-free (negligible ripple). Table 3-1 shows the voltage and current ratings for the medium frequency transformer.



**Figure 3-7 IV and PV characteristics for different sun irradiance levels for the designed PV farm 1.5 kV, 150 kW, and 100 A. Array type: American Solar Wholesale ASW-260M, 40 series modules, 15 parallel strings.**

Table 3-2 shows the volt, ampere ratings semiconductor switches. Utility line to line voltage  $V_{LL\ rms}$  has been used to normalize the voltage rating, while  $I_{PV}$  has been used to normalize the current rating of the semiconductor. For the AC-AC converter, the SiC switch current should handle a (0.816) per unit rating with utility input voltage 2.3 kV to

6.5 kV rms value. The overall dc voltage for the 12-pulse converter is (-5835.49 V). Since the desired dc output voltage is (-1500 V), the turns ratio of the secondary windings should be adjusted using a factor  $k_t$  which can be calculated as follows:

$$k_t = \frac{1500}{5835.49} = 0.257 \quad (3.32)$$

**Table 3-1 Medium frequency transformer ratings for the design example of the presented topology in Figure 3-2.**

Primary side windings	Voltage expression (rms)	$\frac{V_{LL}}{\sqrt{3}} = 0.227V_{DC}$
	Current expression (rms)	$0.9 I_{PV}$
Turns ratio $N_{S1}$ for secondary side windings	Voltage expression (rms)	$\frac{V_{LL}}{\sqrt{3}} \frac{\sqrt{2}}{3} = 0.227V_{LL}$
	Current expression (rms)	$\sqrt{\frac{2}{3}} I_{PV}$
Turns ratio $N_{S2}$ for secondary side windings	Voltage expression (rms)	$\frac{(\sqrt{3}-1) V_{LL}}{3\sqrt{2} \sqrt{3}}$
	Current expression (rms)	$\sqrt{\frac{2}{3}} I_{PV}$
$VA_{Total} = 3 \frac{V_{LL}}{\sqrt{3}} \times 0.9 I_{PV} + 6 \sqrt{\frac{2}{3}} I_{PV} \left[ \frac{\sqrt{3}-1}{3\sqrt{2}} \frac{V_{LL}}{\sqrt{3}} + \frac{\sqrt{2}}{3} \frac{V_{LL}}{\sqrt{3}} \right] = 0.194 \times V_{DC} \times I_{PV}$ $VA_{equivalent} = \frac{1}{2} VA_{Total} = 0.097 P_{Out}$		



**Table 3-2 Semiconductor device ratings for the design example of the presented topology in Figure 3-2.**

Switches	Parameters	Expression	Per unit	Design value 150 kW
AC-AC bridge rectifier	Peak voltage	$\sqrt{\frac{2}{3}} V_{LL}$	0.816 P.U	1878 V
	Peak current	$k_t \frac{4}{\pi PF} I_{PV}$	1.3 $k_t$	35A
	Rms current	$k_t \frac{2}{\pi PF} I_{PV}$	0.6 $k_t$	18 A
AC-AC bridge inverter	Peak voltage	$\sqrt{\frac{2}{3}} V_{LL}$	0.816 P.U	1878 V
	Peak current	$k_t \frac{4}{\pi PF} I_{PV}$	0.816 P.U	35A
	Rms current	$k_t \frac{2}{\pi PF} I_{PV}$	1.3 $k_t$	18 A
12-pulse SCR converter	Peak voltage	$k_t \sqrt{\frac{2}{3}} V_{LL}$	0.816 $k_t$	469.2 V
	Peak current	$I_{PV}$	1	100 A
	Rms current	$I_{PV} \sqrt{\frac{2}{\pi} \left( \frac{\pi}{12} + \frac{1}{4} \right)}$	0.57	57 A

### 3.5. Simulation Results

In this subsection, the simulation results of the proposed converter (see Figure 3-2) are simulated and discussed using MATLAB software to verify the proposed concept. The specification parameters for the design example are listed in Table 3-3. The output voltages of the AC-AC converters are connected to the primary side of the medium frequency 720 Hz phase-shift transformer. The transformer primary side voltages ( $V_{AP}$ ,  $V_{BP}$ ,  $V_{CP}$ ) and their associated currents ( $I_{ap}$ ,  $I_{bp}$ ,  $I_{cp}$ ) are shown in Figure 3-8. Evidently, the voltages and their associated currents are out of phase confirming the inversion operation of the proposed concept, which means the PV power has been injected to the utility grid. Figure 3-9 shows the frequency spectrum of the medium frequency primary voltage  $V_{AP}$ . Obviously, the dominant frequency of  $V_{AP}$  appears around 720 Hz ( $720 \pm 60$ ), which implies that the transformer works at a medium frequency range. Since it works at a medium frequency, that decreases its core size/weight and improves the power density of the converter. Each secondary side of the transformer is connected to a six-pulse SCR converter. A 12-pulse is used to eliminate the low order harmonics ( $5^{th}, 7^{th}$ ) from the input utility currents. In order to run the 12-pulse in the inversion mode, the firing angle should be greater than 90 degree ( $\alpha = 160^0$ ). Figure 3-10 depicts voltage  $V_{PV}$ , current  $I_{PV}$  for the designed PV plant, the output DC voltage for each six-pulse group  $V_{dc1}$ ,  $V_{dc2}$ , and the overall DC outputs for the 12-pulse converter  $V_{dc12\text{-pulse}}$ , respectively. Figure 3-11 shows the input line to neutral voltages  $V_{an}$ ,  $V_{bn}$ ,  $V_{cn}$ , and their associated overall unfiltered utility input current  $i_{Ua}$ ,  $i_{Ub}$ ,  $i_{Uc}$ .

**Table 3-3 Simulation parameters for the design example of the proposed topology in Figure 3-2.**

Utility input voltage	$V_{LL\ rms}$	1230 V
	Utility frequency	60 Hz
Output DC voltage	- 1500 V DC	
AC-AC converter	Bridge rectifier switching frequency	60 Hz
	Bridge inverter switching frequency	720 Hz
Transformer turns ratio	$1/k_t$	Transformer operating frequency= 720 Hz
PV plant specifications	40 series modules connected in series	15 parallel strings
Module: American Solar Wholesale (ASW-260 M)	$V_{PV}=1500\ V\ DC$	Power=150 kW
DC link inductor $L_d$	10 mH	

The FFT analysis of the  $i_{U_a}$  is shown in Figure 3-12. It is clear that the 5<sup>th</sup> and 7<sup>th</sup> and even 17<sup>th</sup>, 19<sup>th</sup> harmonics have been eliminated due to 12-pulse operation. Moreover, with the proposed topology, the injected power to the grid can be regulated by adjusting the firing angle ( $\alpha$ ).

### 3.5.1. Semiconductors Power Losses Evaluation

The semiconductor power losses of the presented system can be computed by analyzing switching, and conduction losses for each semiconductor switch. For the SCR

switch, the commercially available from WESTCODE is used [37]. It is fast turn off Thyristor and it can handle up to 1300 V, 260 A. The switching losses for SCR include two parts:

$$\text{Turn\_ON}_{\text{Loss}} = E_{\text{ON}} \times f_{\text{SW}} \text{ W/Pulse} \quad (3.33)$$

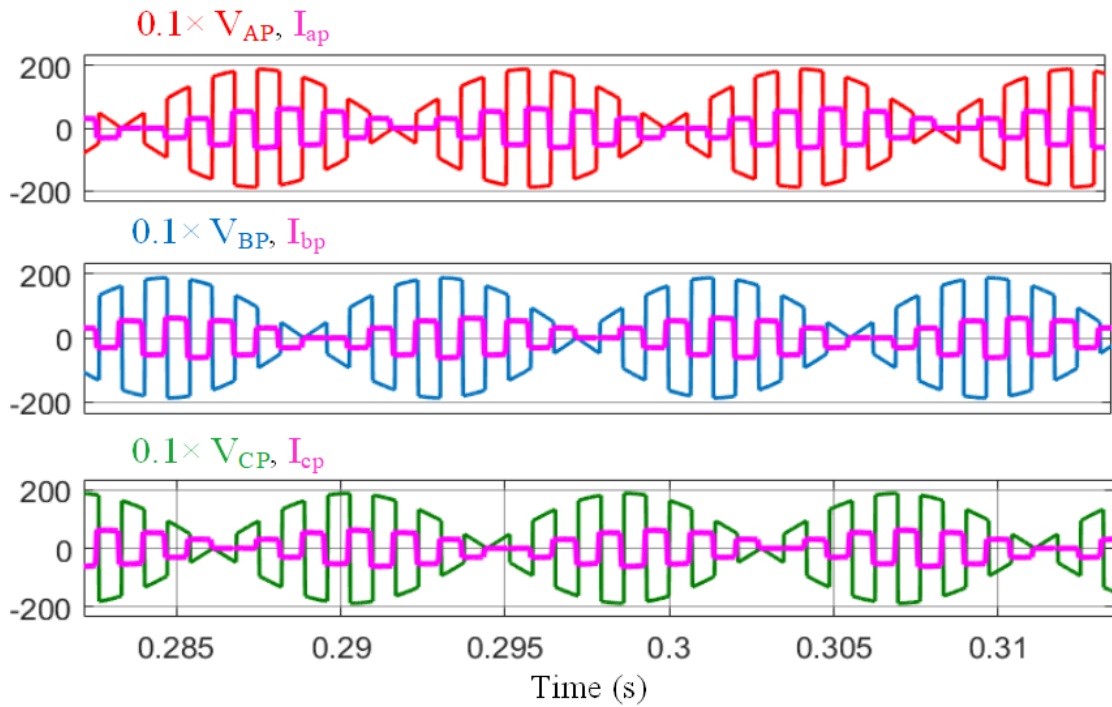
$$\text{Turn\_OFF}_{\text{Loss}} = E_{\text{OFF}} \times f_{\text{SW}} \text{ W/Pulse} \quad (3.34)$$

$E_{\text{ON}}$  and  $E_{\text{OFF}}$  are the energy per pulse and  $f_{\text{SW}}$  is the switching frequency. According to [3], the conduction losses can be calculated as follow:

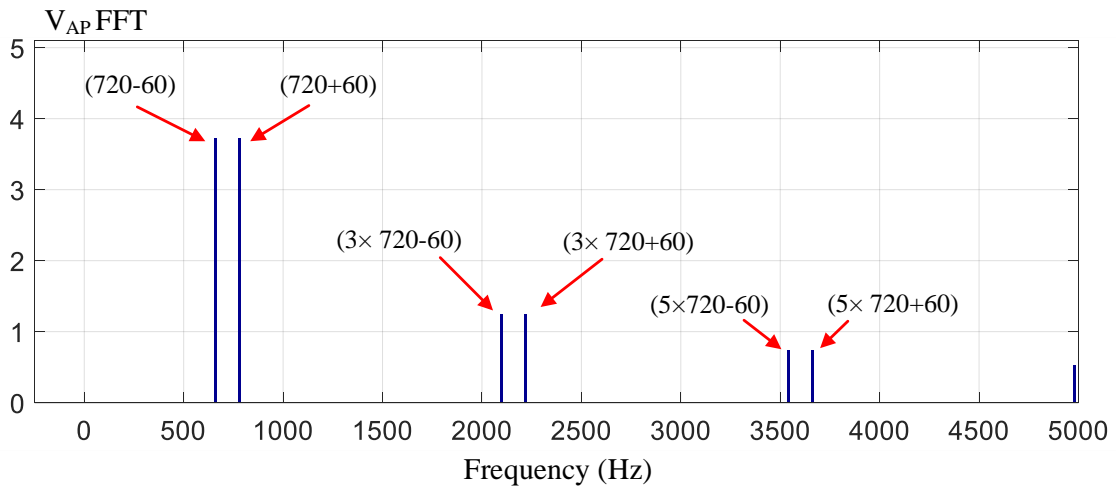
$$P_{\text{Conduction}} = \frac{1}{T} \int_0^T V_T \cdot i_T dt \text{ W} \quad (3.35)$$

$$= \frac{1}{T} \int_0^T (V_{\text{TO}} \cdot i_T) + (R_{\text{On}} \cdot i_T^2 dt) dt = V_{\text{TO}} I_{\text{TM}} R_{\text{On}} \cdot I_T^2 \text{ W} \quad (3.36)$$

Where  $T$  is the period.  $V_{\text{TO}}$  is the  $V$  threshold when the anode current  $I_A$  is zero,  $I_{\text{TM}}$  is the average current, which can be found by integrating the instantaneous current or using the conducting ratio  $\delta$  (i.e. conducting period as a percentage of the full cycle). In six pulse bridge converter, each SCR conducts for  $120^\circ$ . Therefore,  $\delta = 0.333$ .  $I_T$  is the Thyristor current (rms value). For this particular SCR that available [37] and according to its datasheet  $P_{\text{Conduction}} = 85.384 \text{ W}$ ,  $\text{Turn\_ON}_{\text{Loss}} = 5.7 \text{ W}$ , and  $\text{Turn\_OFF}_{\text{Loss}} = 14.4 \text{ W}$ . The total losses per switch are  $105.484 \text{ W}$  and the total losses for the 12-pulse SCR is  $1.2658 \text{ kW}$  which is less than 1% from the total power. For the AC-AC converter,  $6.5 \text{ kV}$ ,  $200 \text{ A}$  Wolfspeed Cree company SiC switch can be used [38].



**Figure 3-8 Primary input voltages, currents for the medium frequency phase-shifted solid-state transformer SST ( $V_{AP}$ ,  $I_{ap}$ ), ( $V_{BP}$ ,  $I_{bp}$ ), and ( $V_{CP}$ ,  $I_{cp}$ ). Note that the voltages are scaled down by 10 for better resolution.**

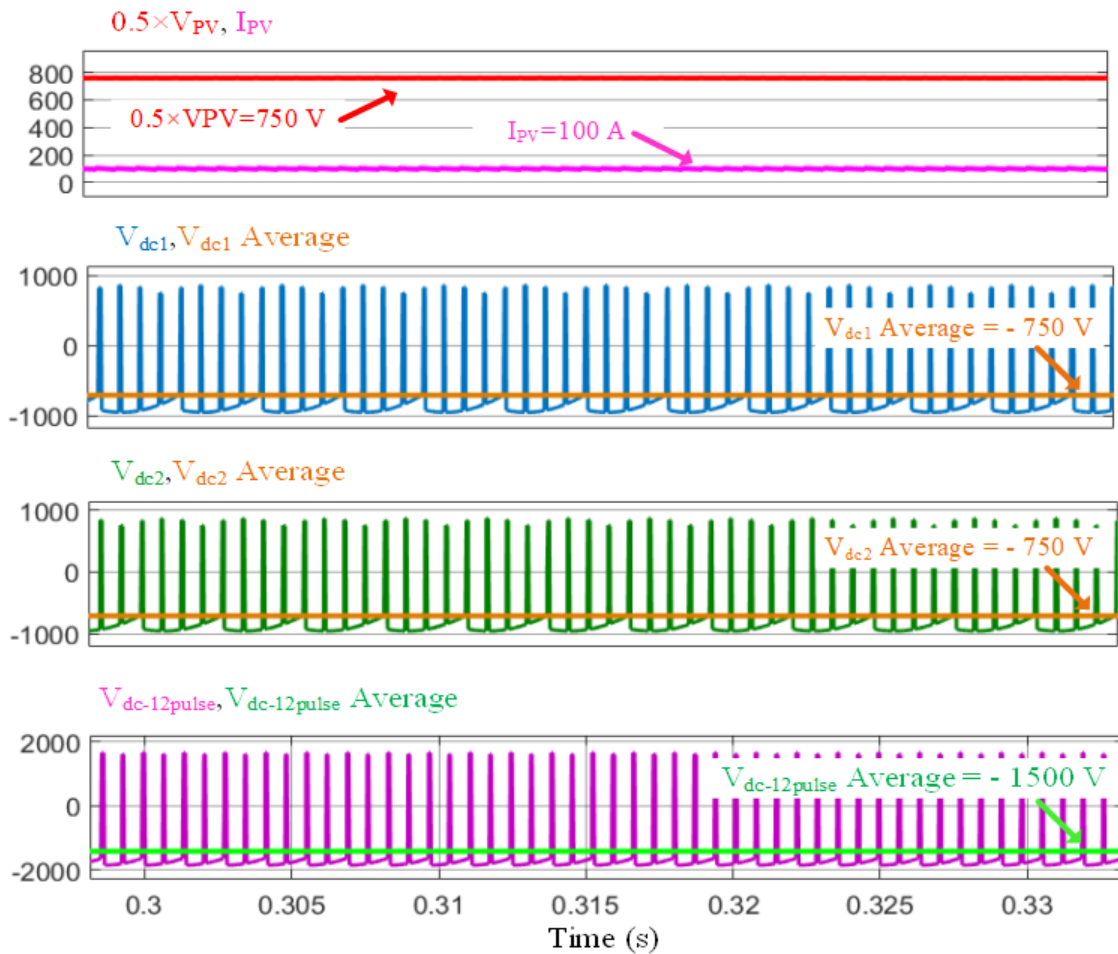


**Figure 3-9 FFT analysis for phase “a” primary voltage of the medium frequency solid-state transformer  $V_{AP}$ .**

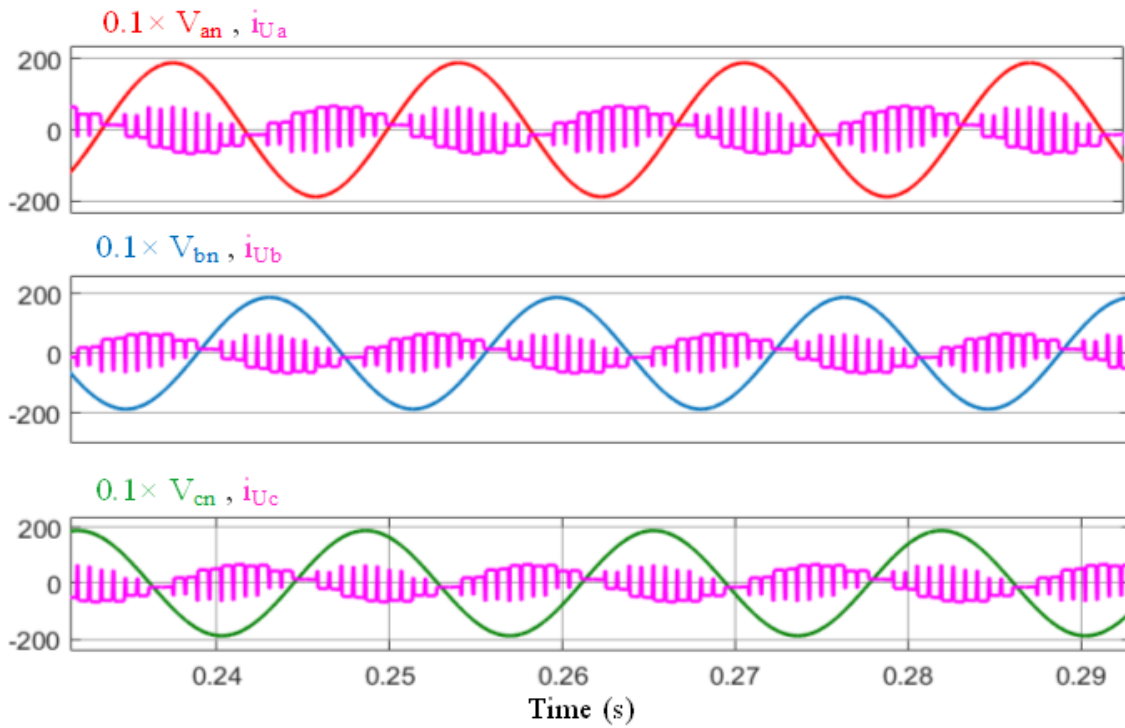
This switch has  $R_{DS\_on} = 20\text{ m}\Omega$ . The conduction loss  $P_{\text{Cond. Loss}}(\text{SiC})$  can be calculated as given by (3.37) and the switching loss  $P_{\text{SW. Loss}}(\text{SiC})$  is given by (3.38).

$$P_{\text{Cond. Loss}}(\text{SiC}) = (I_{\text{rms}})^2 \times R_{DS\_on} = 20.48\text{ W} \quad (3.37)$$

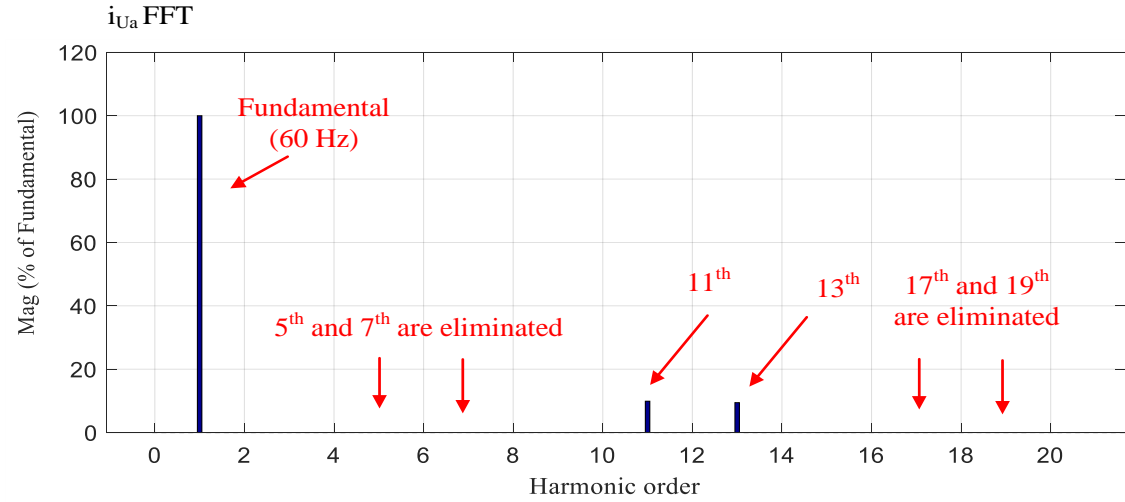
$$P_{\text{SW. Loss}}(\text{SiC}) = (E_{\text{ON}} + E_{\text{OFF}}) \times f_{\text{SW}} = (130\text{ mJ}) \times 720 = 93.6\text{ W} \quad (3.38)$$



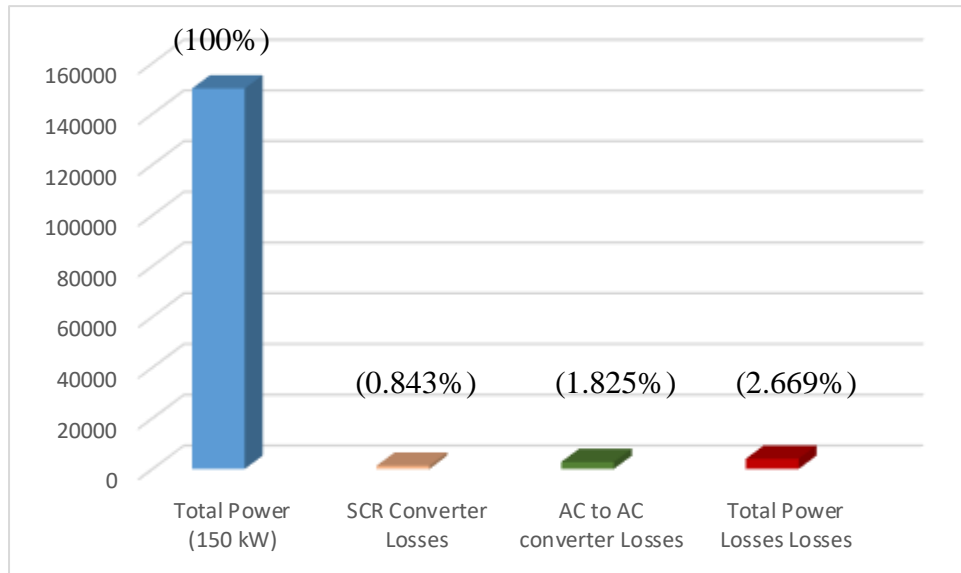
**Figure 3-10** ( $V_{PV}$ ,  $I_{PV}$ ), ( $V_{dc1}$ ,  $V_{dc1}\text{ Average}$ ), ( $V_{dc2}$ ,  $V_{dc2}\text{ Average}$ ), ( $V_{dc12\text{-pulse}}$ ,  $V_{dc12\text{-pulse}\text{ Average}}$ ). Note  $V_{PV}$  is scaled down by 0.5 for better resolution.



**Figure 3-11** Utility input voltages and unfiltered input currents ( $V_{an}$ ,  $i_{Ua}$ ), ( $V_{bn}$ ,  $i_{Ub}$ ), ( $V_{cn}$ ,  $i_{Uc}$ ). Note that the voltages are scaled down by 10 for better resolution.



**Figure 3-12** FFT frequency spectrum for the overall unfiltered input current  $i_{Ua}$ . ( $5^{th}$ ,  $7^{th}$ ,  $17^{th}$  and  $19^{th}$ ) harmonics have been eliminated using the 12-pulse operation.



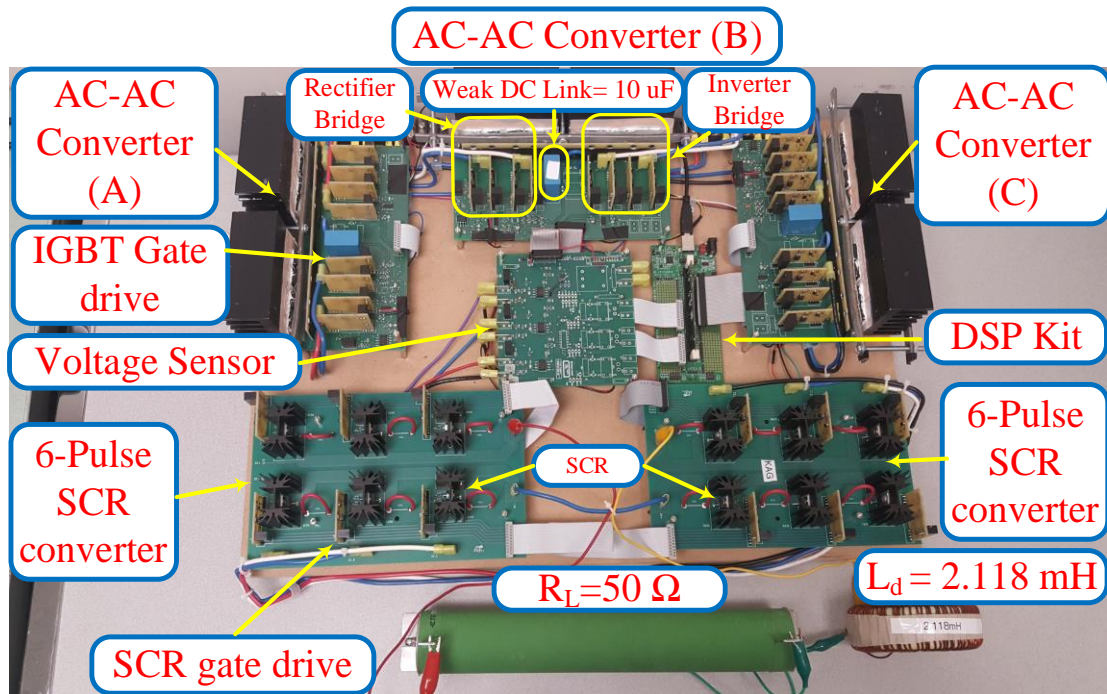
**Figure 3-13 Semiconductor losses break down for the presented topology in Figure 3-2. The overall switching and conduction losses are less than (3%) of the total power.**

The total switching losses for the three phase AC-AC converters for 24 switches are 2737.92 W which is less than (2%) from the overall total power. The total losses for the all semiconductor switches are 4003.74 W which is (2.669%) from the overall power. Figure 3-13 shows the losses break down of the proposed topology in Figure 3-2.

### 3.6. Experimental Results

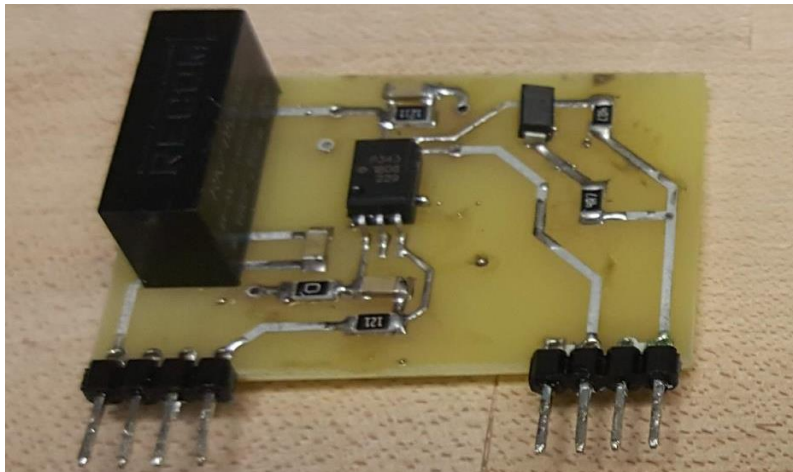
In order to perform the proposed concept, a scale-down laboratory type rated at 1 kW is designed and tested. Figure 3-14 shows the experimental set up of the presented topology in Figure 3-2. The input three phase line to line voltage  $V_{LL\ rms}$  is 90 with line frequency 60 Hz. The switching frequency of the AC-AC converter is 720 Hz. The gate drive for the SCR switches is designed and constructed using surface mount



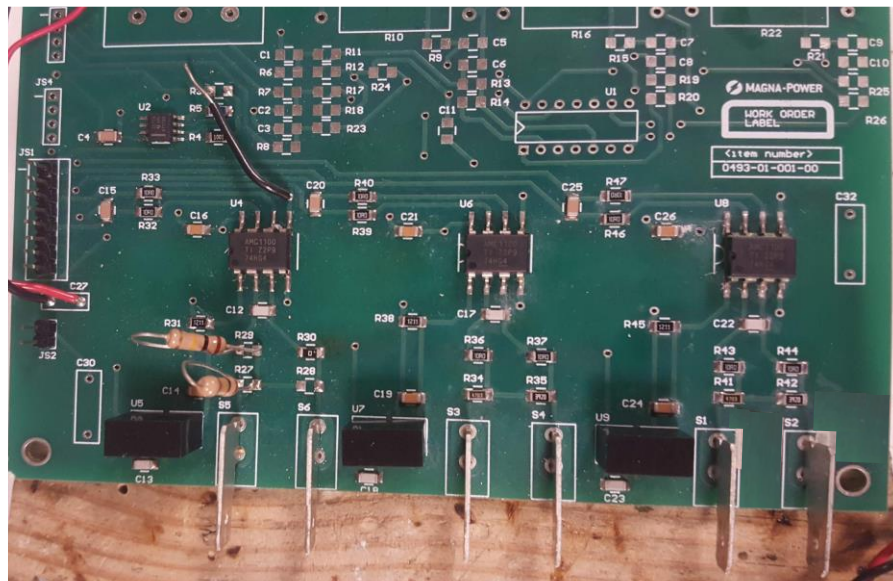


**Figure 3-14 Prototype scale down 1 kW for the proposed topology in Figure 3-2.**

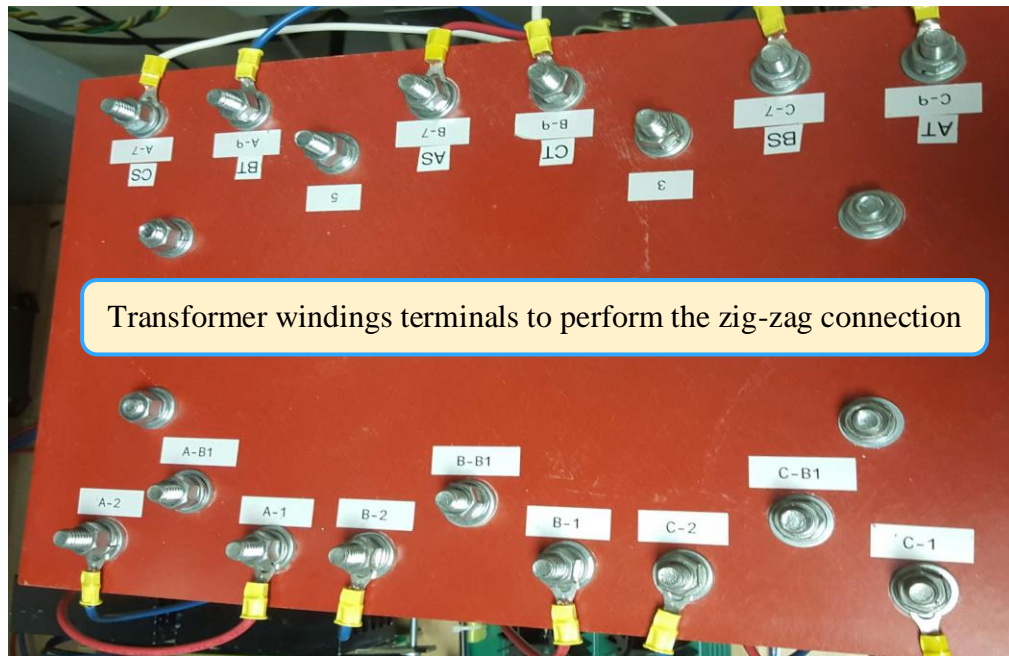
components as shown in Figure 3-15 to drive this particular SCR switch (2N6399) [39]. For the AC-AC converter, the IGBT [40] is used for both rectifier and inverter bridge. The input voltage sensors are designed and built to sense the input utility voltages ( $V_{an}$ ,  $V_{bn}$ ,  $V_{cn}$ ) as shown in Figure 3-16. The gate drive for the AC-AC converter is designed and constructed too. A physical dead time (1.5  $\mu$  Sec) was built for AC-AC converter. The gate drive signals are generated using the Texas Instrument microcontroller (TMS320F28335) [41]. The zig-zag medium frequency transformer is designed to work at the medium frequency range 720 Hz. The core material of this transformer is M19 silicon steel. Figure 3-17 shows the physical zig-zag transformer with dimensions (32 cm  $\times$  24 cm  $\times$  5 cm). The experimental results are similar to the simulation results.



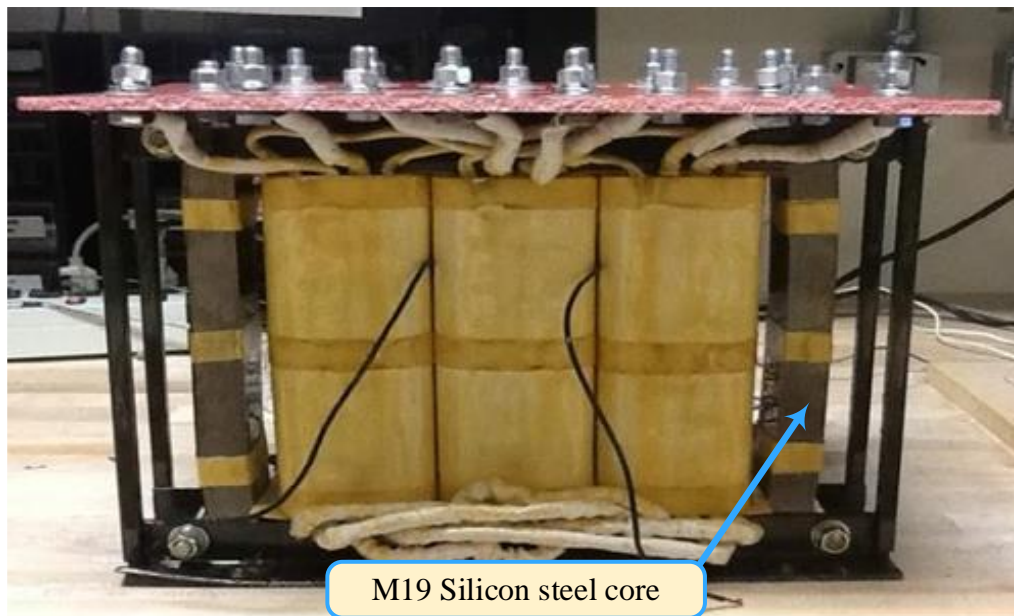
**Figure 3-15 SCR's gate drive circuit using surface mount components.**



**Figure 3-16 Voltage sensors board for the three phase input utility voltages ( $V_{an}$ ,  $V_{bn}$ ,  $V_{cn}$ ).**



(a)



(b)

**Figure 3-17 Physical medium frequency zig-zag transformer with dimensions (32 cm × 24 cm × 5 cm), 7 KVA M19 Silicon steel core material used for the experimental results. (a) front view, (b) side view.**

Figure 3-18 shows the three phase medium frequency 720 Hz transformer input voltages  $V_{AP}$ ,  $V_{BP}$ ,  $V_{CP}$ . Evidently, these input voltages are shifted by  $(6.667 \text{ ms}) 120^\circ$  to each other. Figure 3-19 is  $V_{AP}$  FFT confirming the medium frequency operation of the transformer. It is evident that the dominant frequency component appears at  $(720 \pm 60)$  Hz,  $(3 \times 720 \pm 60)$  Hz,  $(5 \times 720 \pm 60)$  Hz. This enables the transformer to operate at medium frequency. The 12-pulse DC output voltage is observed from Figure 3-20; the net  $30^\circ$  phase-shift  $(1.667 \text{ ms}) 30^\circ$  between the secondary side voltage  $V_{AB \text{ Sec}}$  and tertiary side voltage  $V_{AB \text{ Ter}}$  of the presented topology (see Figure 3-2) is observed too. The  $30^\circ$  phase-shift between the secondary and tertiary sides is evident to allow the 12-pulse operation. The voltage and current for  $T_1$  switch (see Figure 3-2) are shown in Figure 3-21. When the switch is turned off, there is a blocking voltage  $V_{AK}$  and the current at this interval time is zero. However, when the switch is turned on,  $V_{AK}$  almost zero (ignoring the forward drop voltage) and there is a current at this interval of time as expected. Figure 3-22 shows the input line to neutral voltage  $V_{an}$ , the overall unfiltered input utility current  $i_{Ua}$  along with its FFT. The frequency spectrum shows that the low order harmonics ( $5^{\text{th}}$ ,  $7^{\text{th}}$ ) are eliminated to confirm the 12-pulse operation. Furthermore, the  $17^{\text{th}}$  and  $19^{\text{th}}$  harmonics are eliminated too. The THD of this current is 19%, but it can be improved by using a passive input filter. One of the features of the presented topology is the DC output voltage can be regulated by adjusting the firing angle ( $\alpha$ ). Figure 3-23 shows the DC output voltage for six-pulse and 12-pulse converter for ( $\alpha=0^\circ$ ). The  $V_{dc1}=108 \text{ V}$ ,  $V_{dc2}=110 \text{ V}$ , and the  $V_{dc12\text{-pulse}}=231 \text{ V}$ . By increasing ( $\alpha=30^\circ$ ), these aforementioned voltages are decreased as shown in Figure 3-24.

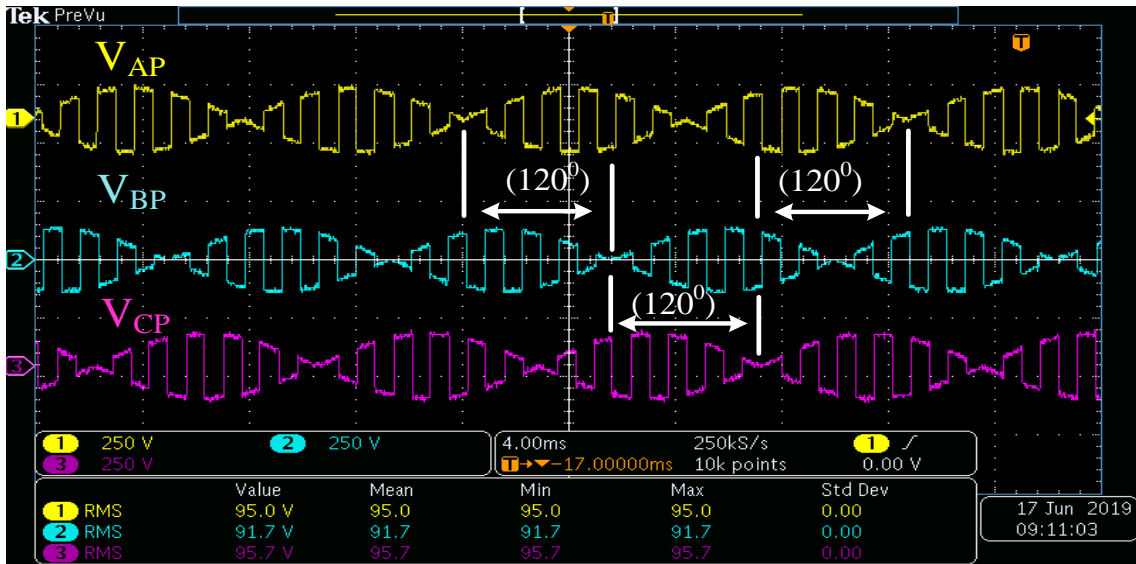


Figure 3-18 Experimental results for medium frequency transformer primary voltages. Ch1: Phase “a” primary voltage  $V_{AP}$ , Ch2: Phase “b” primary voltage  $V_{BP}$ , Ch3: Phase “c” primary voltage  $V_{CP}$ . Note: they are shafted by  $120^\circ$  to each other.

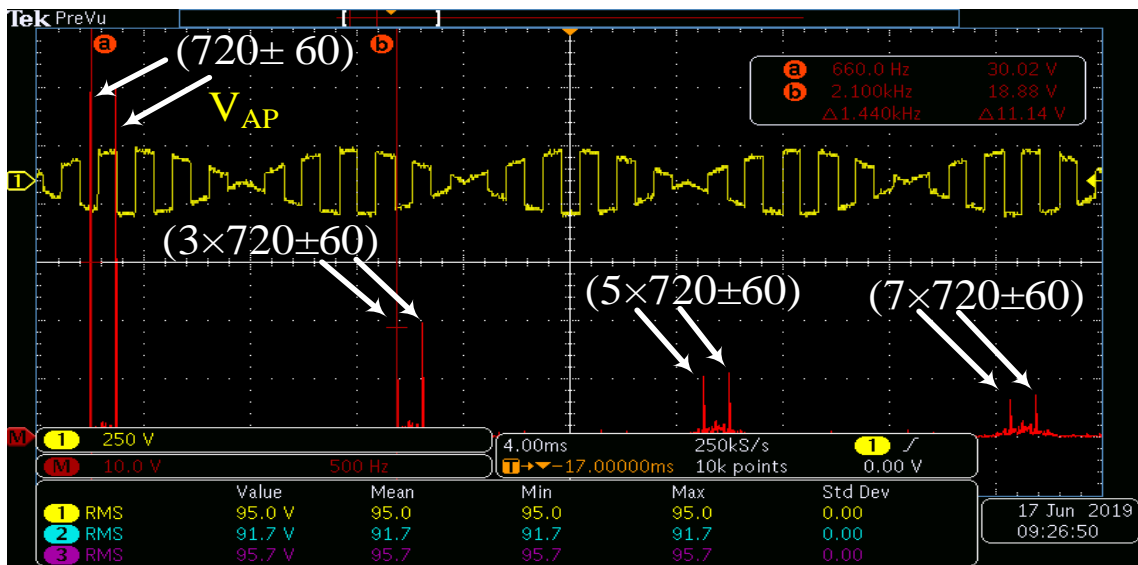


Figure 3-19 Experimental results. Ch. 1: Primary voltage  $V_{AP}$ ; Ch. M:  $V_{AP}$  FFT analysis shows the dominant frequency component appears around 720 Hz enabling the medium frequency operation.

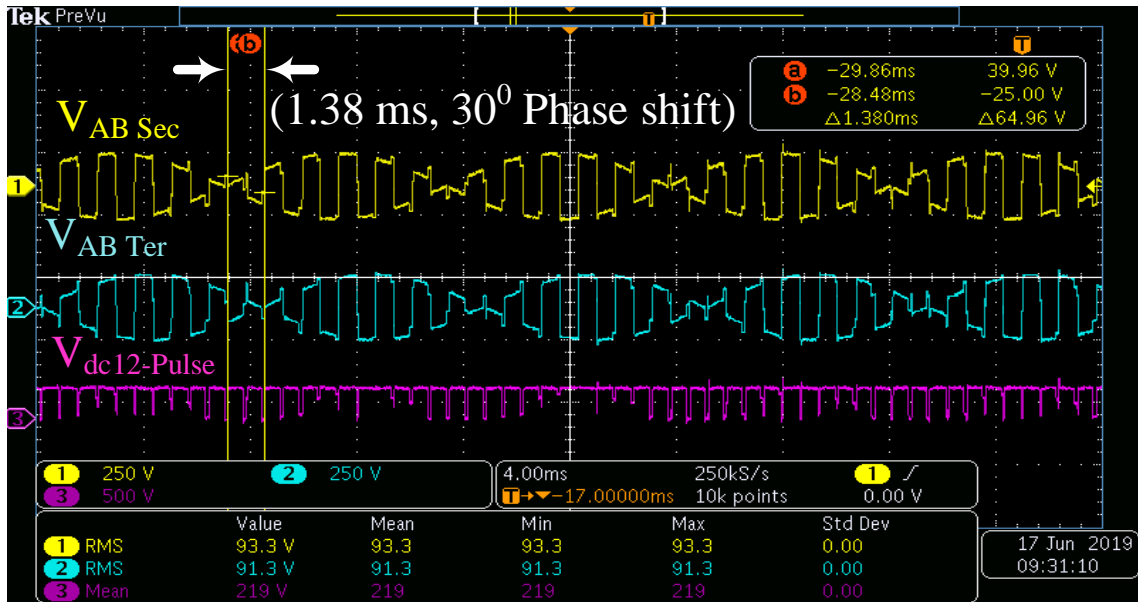


Figure 3-20 Experimental results. Ch.1 Line to line voltage of the secondary side  $V_{AB-Sec}$ ; Ch.2 Line to Line of the tertiary side  $V_{AB-Ter}$ ; Ch.3 DC output voltage for the 12-pulse converter  $V_{dc12-pulse}$  when ( $\alpha=0^0$ ) for rectification mode operation.

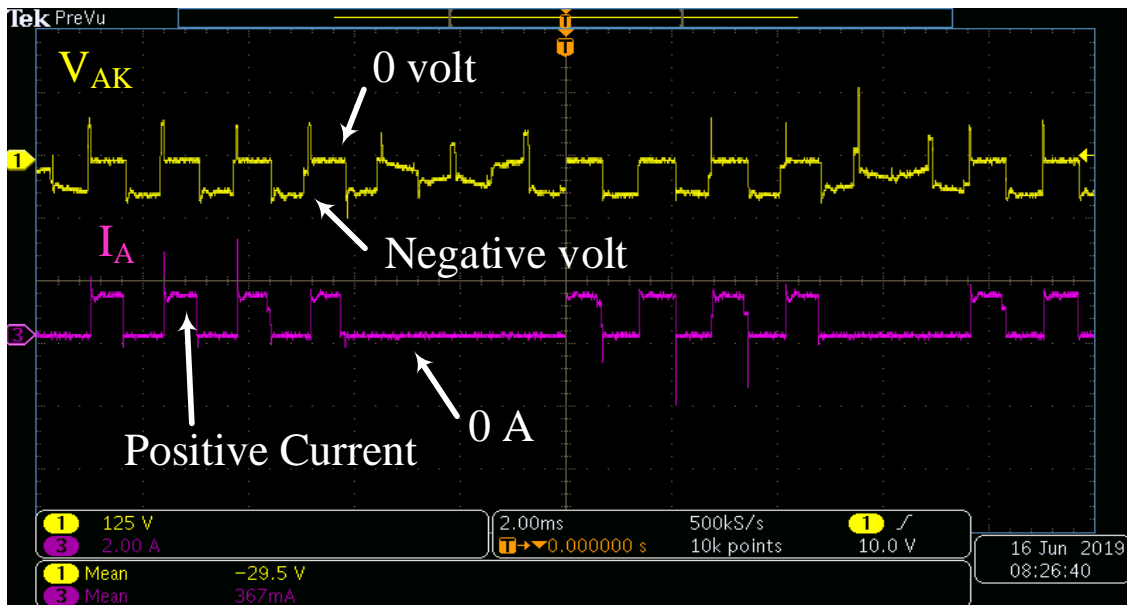


Figure 3-21 Experimental results. Ch.1 Anode cathode voltage  $V_{AK}$  for  $T_1$ ; Ch.2 Anode current  $I_A$  for  $T_1$  (see Figure 3-2).

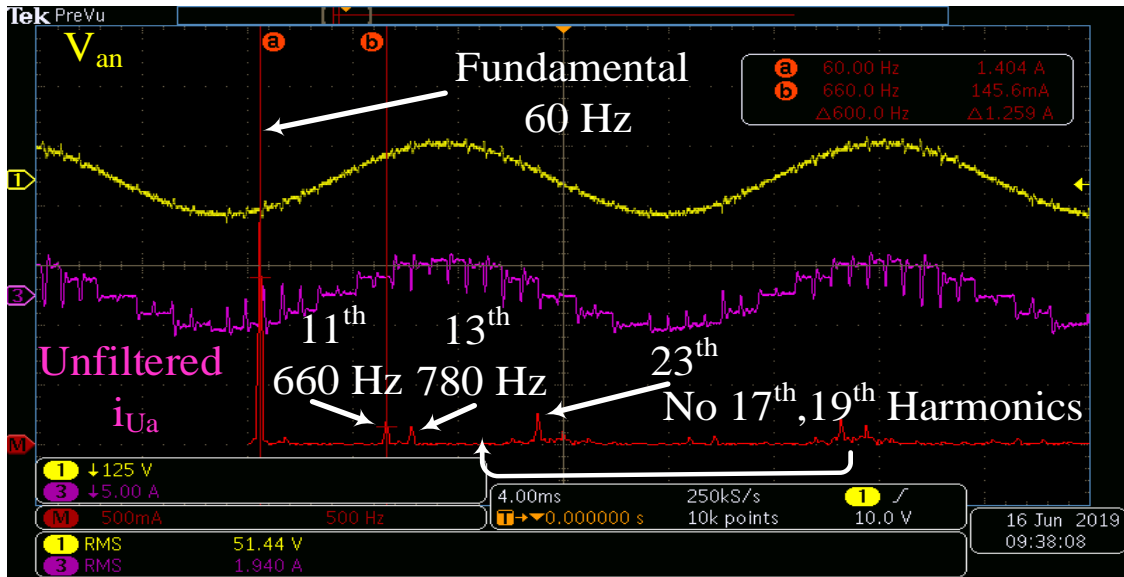


Figure 3-22 Experimental results. Ch. 1: Input line to neutral voltage  $V_{an}$ ; Ch. 3: Unfiltered input current  $i_{Ua}$ ; Ch. M:  $i_{Ua}$  FFT spectrum analysis. (5<sup>th</sup>, 7<sup>th</sup>, 17<sup>th</sup> and 19<sup>th</sup> are eliminated due to the 12-pulse operation).

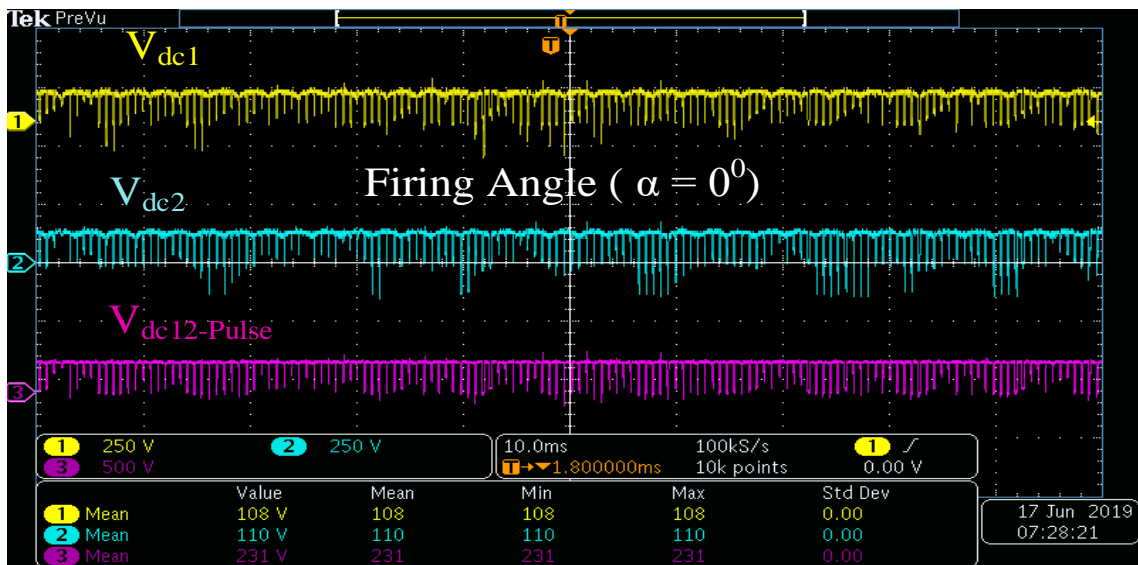


Figure 3-23 Experimental results. Ch.1: DC output voltage for the first six-pulse SCR converter  $V_{dc1}=108$  V; Ch.2 DC output voltage for the second six-pulse SCR converter  $V_{dc1}=110$  V; Ch. 3: DC output voltage for the 12-pulse converter  $V_{dc12-Pulse}=231$  V. The firing angle ( $\alpha=0^\circ$ ).

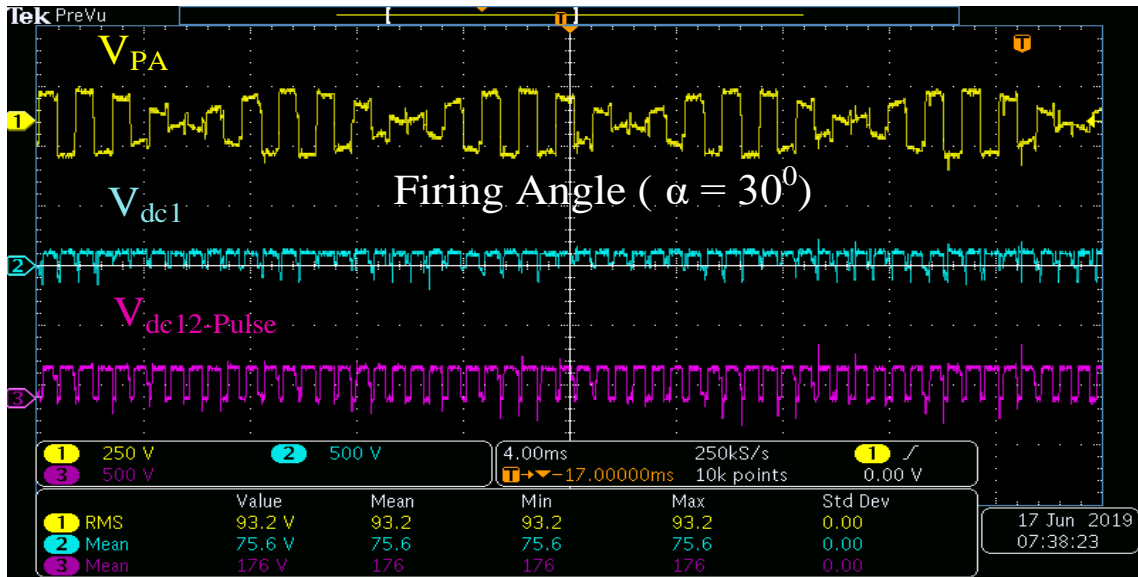


Figure 3-24 Experimental results. Ch.1: Transformer primary voltage  $V_{AP}$ ; Ch.2: DC output voltage for the first six-pulse SCR converter  $V_{dc1}=75.6$  V; Ch. 3: DC output voltage for the 12-pulse converter  $V_{dc12-Pulse}=176$  V. The firing angle ( $\alpha=30^\circ$ ).

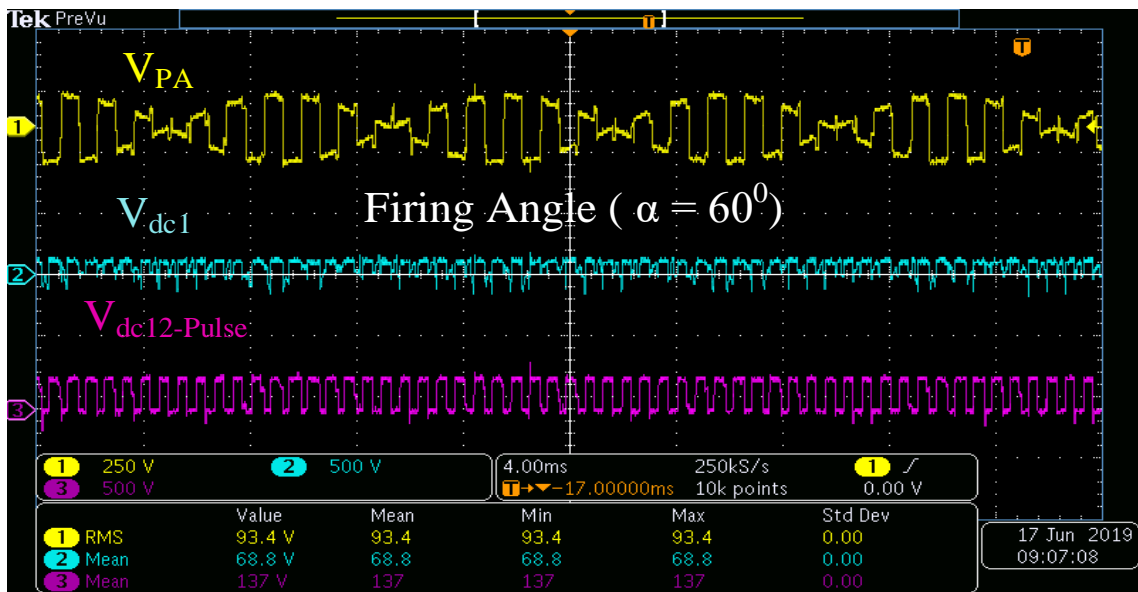
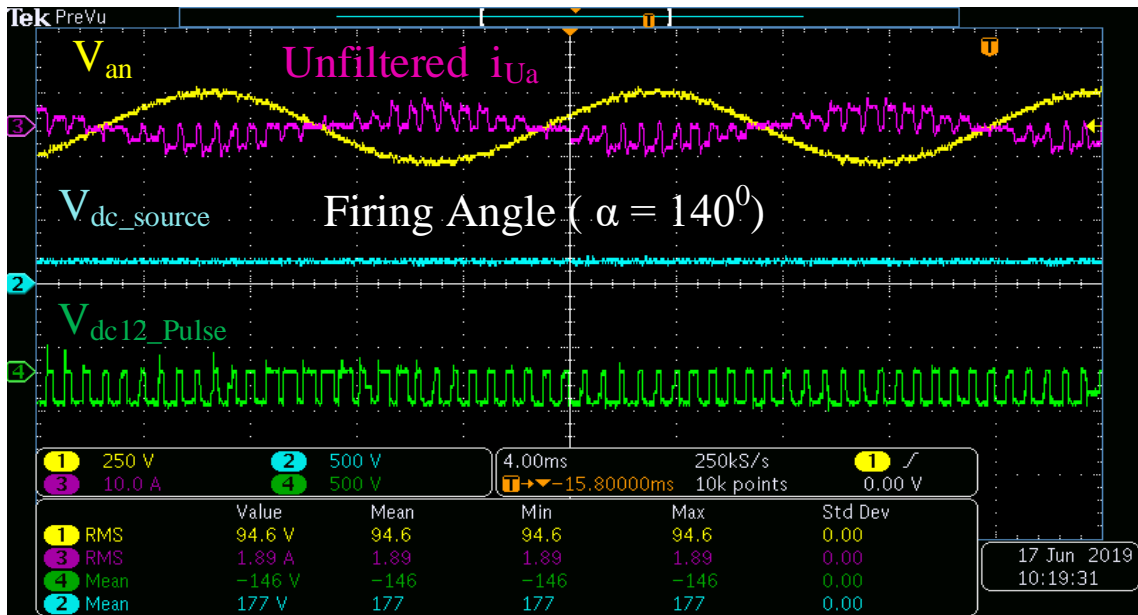


Figure 3-25 Experimental results. Ch.1: Transformer primary voltage  $V_{AP}$ ; Ch.2: DC output voltage for the first six-pulse SCR converter  $V_{dc1}=68.8$  V; Ch. 3: DC output voltage for the 12-pulse converter  $V_{dc12-Pulse}=137$  V. The firing angle ( $\alpha=60^\circ$ ).





**Figure 3-26 Experimental results. Ch.1: Input line to neutral voltage  $V_{an}$ ; Ch.3: Unfiltered input current  $i_{Ua}$ ; Ch. 2: DC voltage supply=177 V; Ch. 4: DC output voltage for the 12-pulse converter  $V_{dc12-Pulse} = -146$  V. The firing angle ( $\alpha=140^\circ$ ).**

$V_{dc1}=75.6$  V and  $V_{dc12-pulse}=176$  V. Further increasing the firing angle ( $\alpha =60^\circ$ ), these voltages are decreased further as shown in Figure 3-25  $V_{dc1}=68.8$  V and  $V_{dc12-pulse}=137$  V. The SCR switch can work for more than one quadrant. For the inversion mode operation, the firing angle should be ( $90 > \alpha > 180$ ) theoretically, but in practical ( $\alpha < 180$ ). To confirm the inversion mode operation, DC voltage source has been connected at the output terminal of the 12-pulse converter with inductor ( $L_d=2.1$  mH). The firing angle sets ( $\alpha=140^\circ$ ) to let the power goes back from the DC side to the utility AC side. Figure 3-26 shows the input line to neutral voltage  $V_{an}$  and the phase “a” unfiltered input current  $i_{Ua}$ . They are out of phase confirming the inversion mode operation.

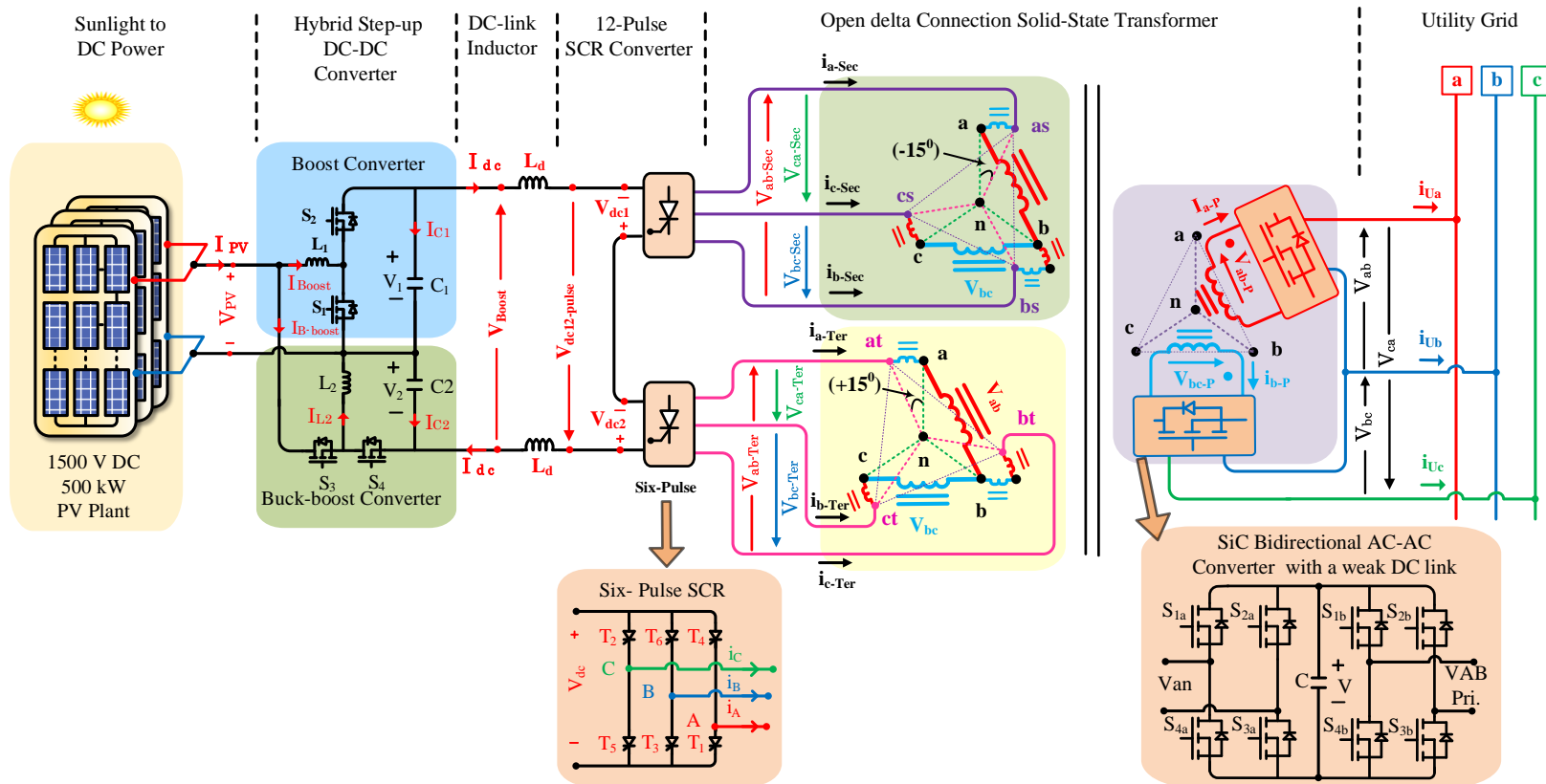
### **3.7. Open Delta Scheme for 12-Pulse SCR Converter with Medium Frequency**

#### **Integrated Solid-State Transformer**

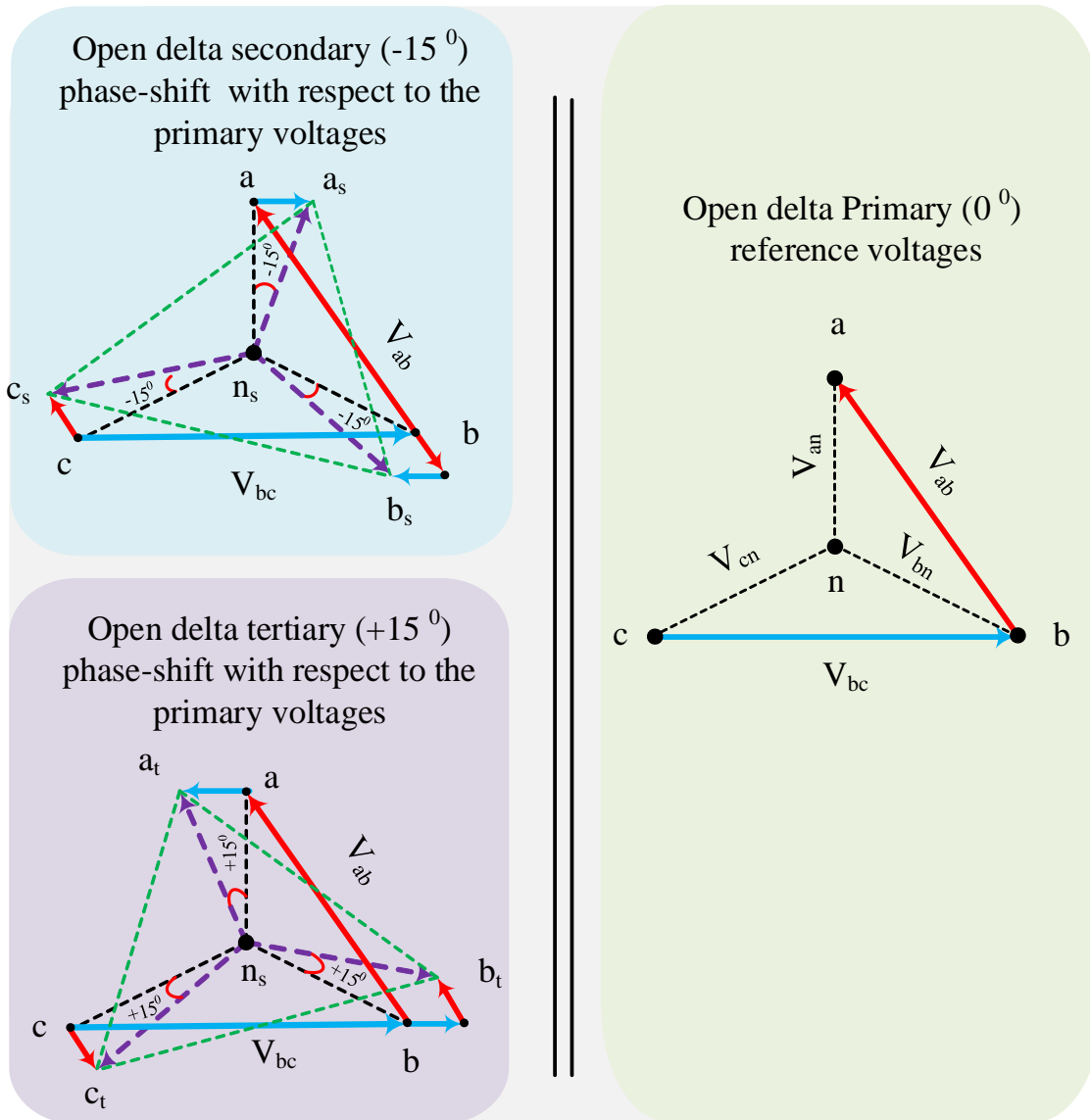
In order to increase the reliability of the proposed topology in Figure 3-2 by minimizing the number of semiconductor components, the open delta connection can be used. It will decrease the number of AC-AC converters. Instead of using three AC-AC converters that have twenty-four active switches, with the open delta concept, it is possible to use only two AC-AC converters that have only sixteen switches. Moreover, this concept reduces the transformer windings too. The system efficiency will be improved by reducing the losses of the AC-AC converter and transformer windings losses. Figure 3-27 shows the proposed concept of open delta connection for 12-pulse SCR converter using zig-zag phase-shift medium frequency MF solid-state transformer SST and the proposed hybrid step-up DC-DC converter. The proposed step-up DC-DC converter is explained in the previous section.

#### **3.7.1. Open Delta Phase-Shift Transformer Phasor Diagram**

The phasor diagram of the open delta transformer is illustrated in Figure 3-28. Mainly, each phase has one primary winding and six secondary windings (see Figure 3-27). In order to design the net  $(-15^\circ, +15^\circ)$  phase-shift that should be created between the secondary and tertiary side, equation (3.39) explains how to get the  $(-15^\circ)$  phase shift at the secondary side with respect to the primary voltages. Simplifying the previous equation further to get the transformer designed turns ratio yields to equation (3.40).



**Figure 3-27 Proposed medium frequency open delta solid-state transformer for 12-pulse SCR converter and the proposed hybrid step-up DC-DC converter.**



**Figure 3-28** Phasor diagram of the proposed open delta phase-shift transformer to create a  $(30^\circ)$  phase-shift between the secondary and tertiary sides. Each phase has one primary winding and six secondary windings (see Figure 3-27).

$$\begin{aligned}
 & N_{s3} \cdot V_{ab} + N_{s1} \cdot V_{bc} + N_{s1} \cdot V_{ab} + N_{s1} \cdot V_{bc} & (3.39) \\
 & = N_{s3} \angle 30^\circ + N_{s1} (2 \angle -90^\circ + 1 \angle 30^\circ) = 1 \angle -15^\circ
 \end{aligned}$$

$$N_{p1} : N_{s1} : N_{s2} : N_{s3} : N_{s4} : N_{s5} : N_{s6} = 1 : 0.15 : 0.15 : 0.97 : 0.97 : 0.15 : 0.15 \quad (3.40)$$

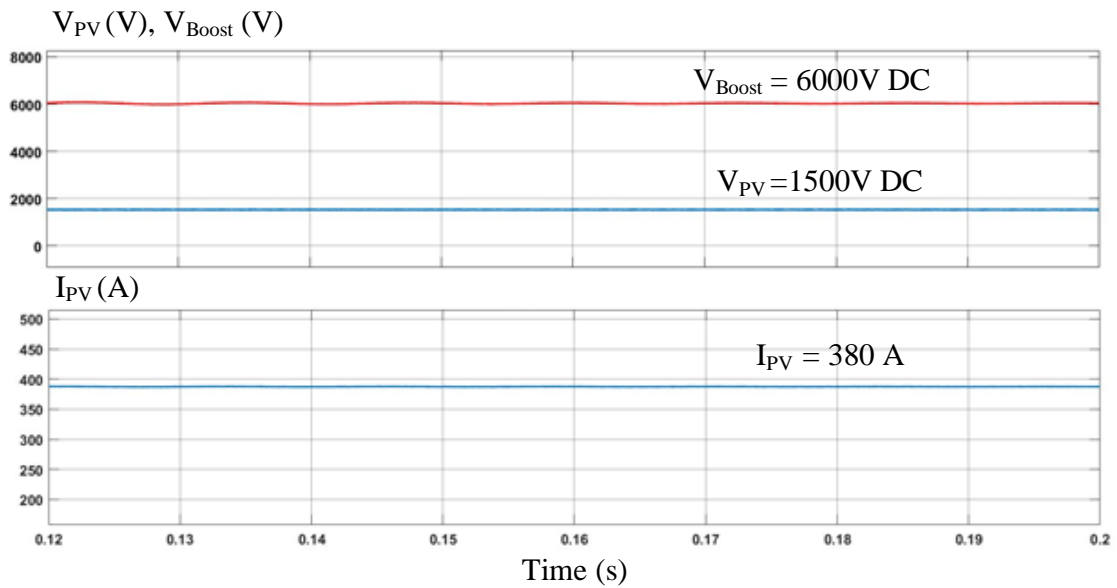
### 3.7.2. Open Delta Simulation Results

The presented concept of open delta scheme (see Figure 3-27) for 12-pulse SCR converter has been simulated using MATLAB software to verify the concept. The design example parameters are listed in Table 3-4. Figure 3-29 shows the 1.5 kV PV plant voltage  $V_{PV}=1500V$ , the step-up DC-DC converter output voltage  $V_{Boost}=6kV$ , and the PV plant current  $I_{PV}=380A$ . Figure 3-30 demonstrates the DC voltage of each six-pulse ( $V_{dc1}$ ,  $V_{dc1-Ave}$ ), ( $V_{dc2}$ ,  $V_{dc2-Ave}$ ), and the dc output voltage of the 12-six-pulse ( $V_{dc12-pulse}$ ,  $V_{dc12pulse-Ave}$ ).

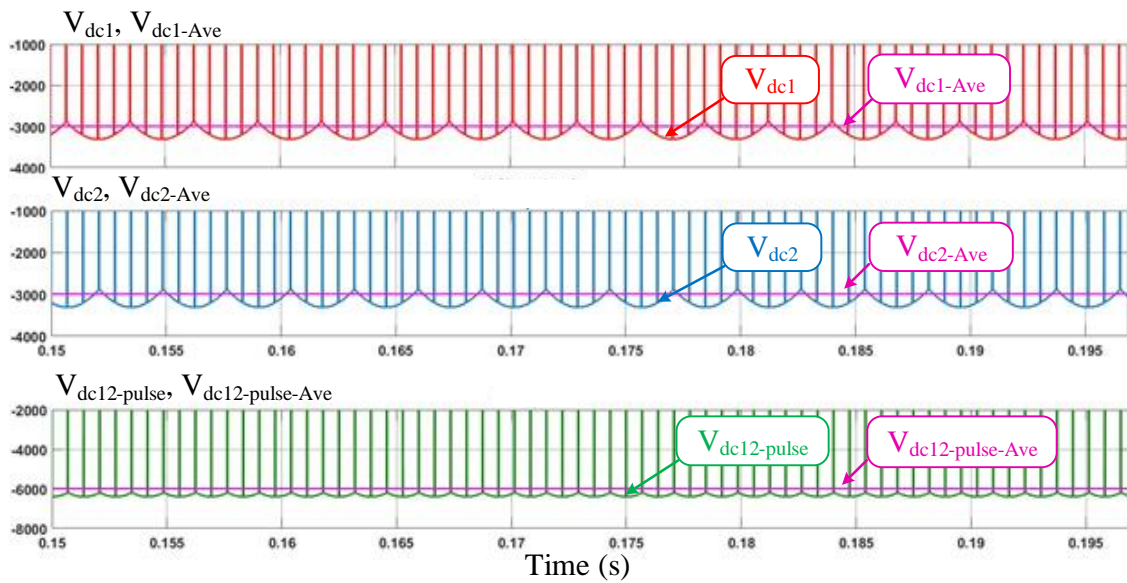
**Table 3-4 Simulation parameters for the design example of the proposed open delta concept in Figure 3-27.**

PV Plant	
Module type	American Solae Wholesale ASW-260
Number of series panels=35	Number of parallel strings=55
PV Generated power=0.5 MW	$V_{PV} = 1.5 \text{ kV}$
Utility grid voltage= 2.26 kV	Utility grid frequency=60 Hz
SCR parameters for 12-pulse converter	
SCR switching frequency= 720 Hz	$\alpha = 160^\circ$ , $L_d=10 \text{ mH}$
Hybrid step-up DC-DC converter	
$C_1=100 \text{ uF}$ , $L_1=150 \text{ uH}$	$C_2=100 \text{ uF}$ , $L_2=150 \text{ uH}$
$V_{in}=1500 \text{ V}$	$V_{out}=6000 \text{ V}$
Switching frequency 10 kHz	$D_1=0.5$ , $D_2=0.667$

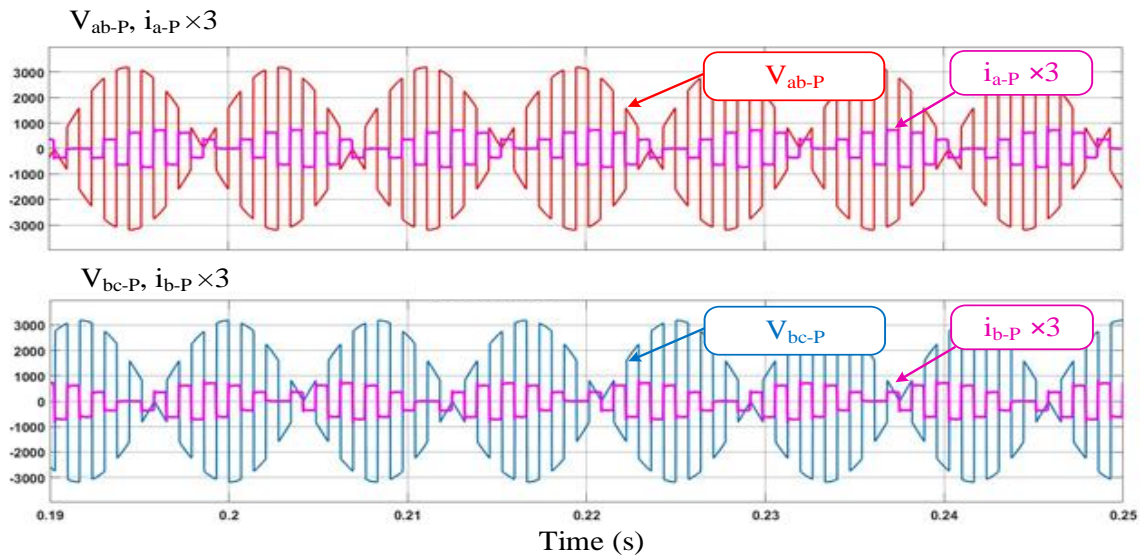
Figure 3-31 shows the medium frequency 720 Hz open delta transformer primary voltages and currents (see Figure 3-27). The medium frequency secondary voltages and currents for the open delta phase-shift solid-state transformer are shown in Figure 3-32. The medium frequency tertiary side voltages and currents are shown in Figure 3-33. Finally, Figure 3-34 shows the overall utility side voltages and their associated unfiltered currents ( $V_{ab}$ ,  $i_{Ua}$ ), ( $V_{bc}$ ,  $i_{Ub}$ ), ( $V_{ca}$ ,  $i_{Uc}$ ). Note that all the currents have been multiplied by 3 for better resolution. The FFT spectrum analysis for the overall unfiltered input current for phase “a”  $i_{Ua}$  is shown in Figure 3-35. It is shown the low order harmonics ( $5^{th}$ ,  $7^{th}$ ) are eliminated by the 12-pulse operation. Furthermore, the ( $17^{th}$ ,  $19^{th}$ ) are eliminated too. The simulation results demonstrate a good input current quality same as the conventional 12-pulse converter. However, this concept replaces the line frequency (50/60) Hz transformer by medium frequency 720 Hz one. Furthermore, the open delta concept improves the reliability, efficiency, and power density of the overall converter.



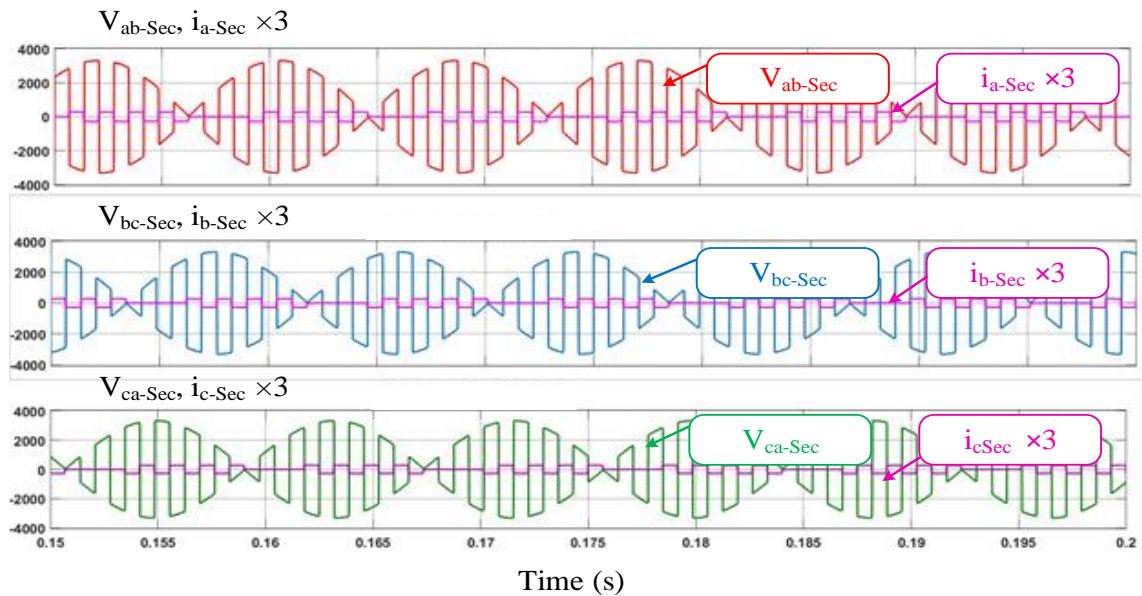
**Figure 3-29**  $V_{PV}=1.5$  kV PV plant voltage, hybrid step-up DC-DC converter output voltage= 6kV,  $I_{PV}=380$  A PV plant current.



**Figure 3-30** Output voltage of first six-pulse ( $V_{dc1}$ ,  $V_{dc1-Ave}$ ), output voltage of second six-pulse ( $V_{dc2}$ ,  $V_{dc2-Ave}$ ), output voltage of the 12- pulse ( $V_{dc12-pulse}$ ,  $V_{dc12pulse-Ave}$ ).

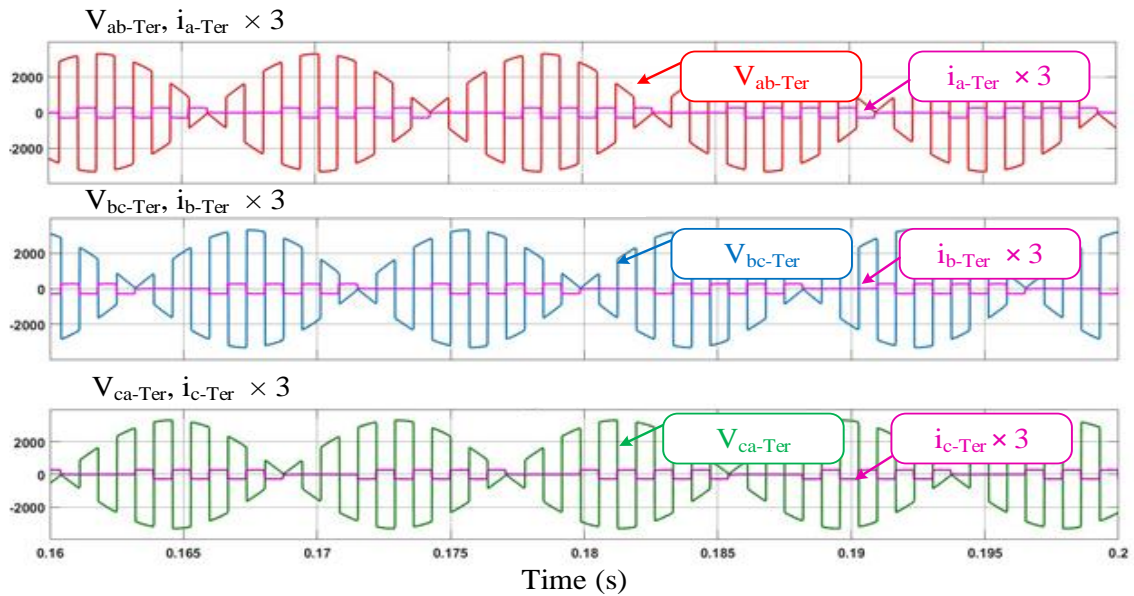


**Figure 3-31 Primary voltages and currents for the open delta phase-shift solid-state transformer ( $V_{ab-P}$ ,  $i_{a-P} \times 3$ ), ( $V_{bc-P}$ ,  $i_{b-P} \times 3$ ). Note the input currents have been multiplied by 3 for better resolution.**

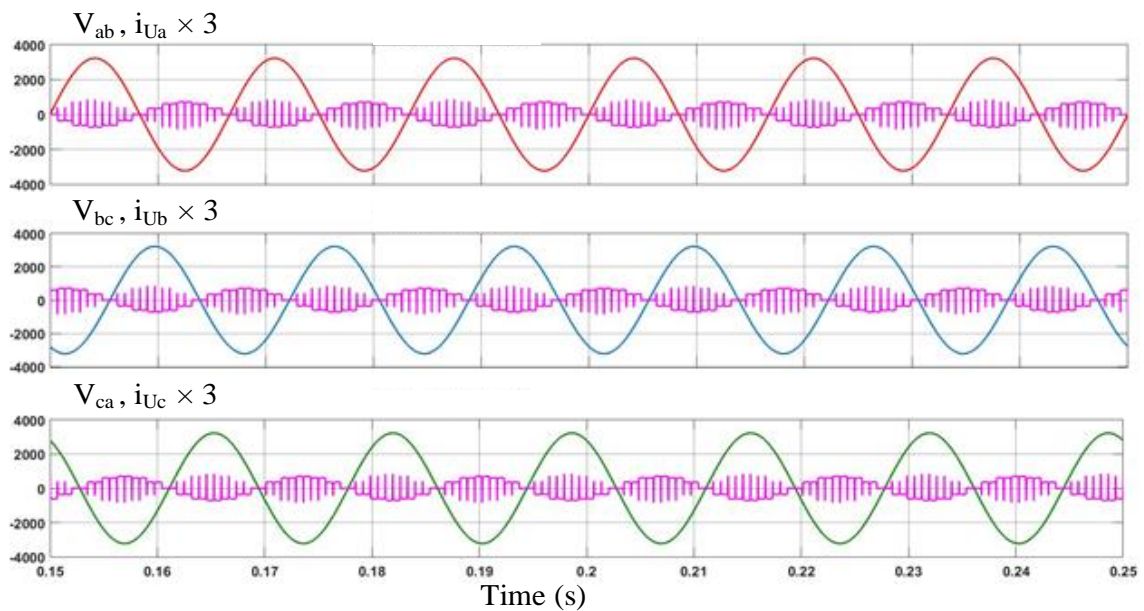


**Figure 3-32 Secondary voltages and currents for the open delta phase-shift solid-state transformer ( $V_{ab-Sec}$ ,  $i_{a-Sec} \times 3$ ), ( $V_{bc-Sec}$ ,  $i_{b-Sec} \times 3$ ), ( $V_{ca-Sec}$ ,  $i_{c-Sec} \times 3$ ). Note the secondary currents have been multiplied by 3 for better resolution.**





**Figure 3-33 Tertiary voltages and currents for the open delta phase-shift solid-state transformer ( $V_{ab-Ter}$ ,  $i_{a-Ter} \times 3$ ), ( $V_{bc-Ter}$ ,  $i_{b-Ter} \times 3$ ), ( $V_{ca-Ter}$ ,  $i_{c-Ter} \times 3$ ). Note the tertiary currents have been multiplied by 3 for better resolution.**



**Figure 3-34 Utility input voltages and currents ( $V_{ab}$ ,  $i_{Ua} \times 3$ ), ( $V_{bc}$ ,  $i_{Ub} \times 3$ ), ( $V_{ca}$ ,  $i_{Uc} \times 3$ ). Note the input utility currents have been multiplied by 3 for better resolution.**

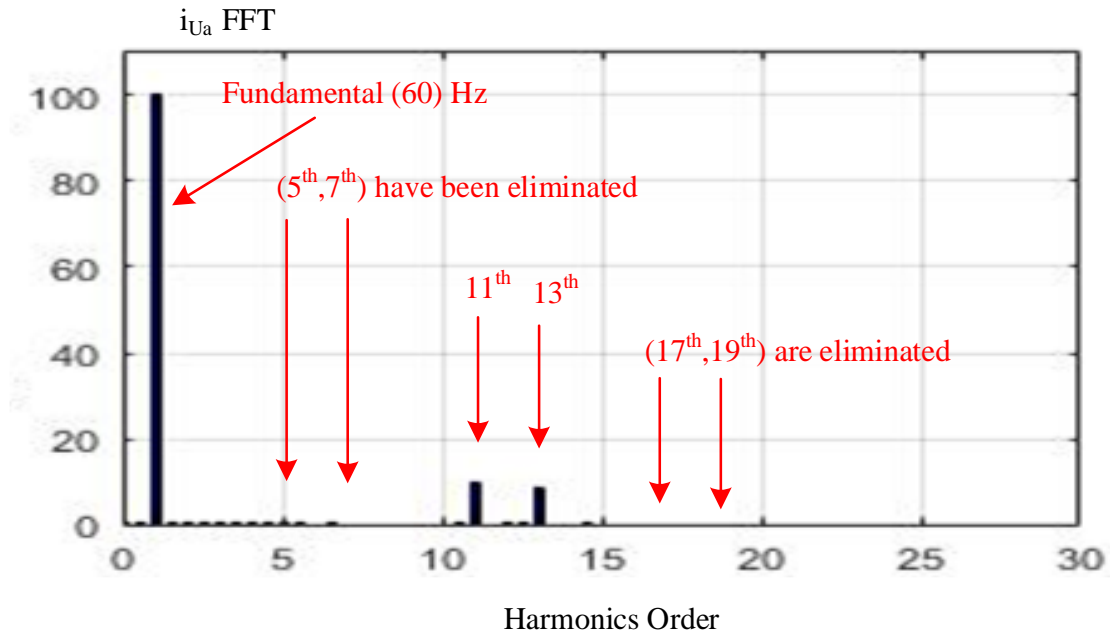


Figure 3-35 FFT analysis for phase “a” utility input current  $i_{Ua}$ .

### 3.8. Conclusion

In this section, a medium voltage DC collection grid with medium frequency 720 Hz integrated solid-state transformer, and 12-pulse SCR converter is presented. Simulation results with detailed design example along with scale down 1 kW laboratory prototype experimental results demonstrate the operation of 12-pulse SCR converter. The results show the capability of bidirectional power flow between the AC and DC side. The input current has a very good quality by eliminating the low order harmonics, e.g. (5<sup>th</sup>, 7<sup>th</sup>, 17<sup>th</sup>, 19<sup>th</sup>), which is the same as the conventional 12-pulse operation. Furthermore, a new concept of open delta medium frequency integrated solid-state transformer is presented. The system reliability, efficiency, and power density are improved by eliminating one of

the AC-AC converters and transformer windings, while maintaining the same input current quality of 12-pulse operation.

#### **4. HIGH FREQUENCY INTEGRATED SOLID-STATE TRANSFORMER (SST) FOR UTILITY INTERFACE OF SOLAR PV / BATTERY ENERGY STORAGE SYSTEMS\*\***

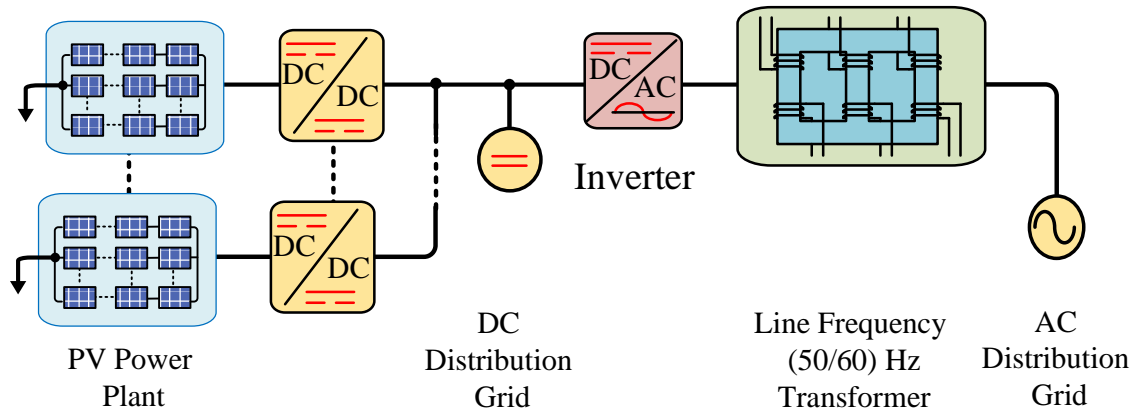
In this section, a high frequency solid-state transformer SST concept for utility interface of solar PV / battery energy storage system is proposed. The primary side consists of three 1-phase AC-AC converter blocks with a weak dc-link (small film capacitor) interfaced with a high frequency transformer. The secondary side of the transformer is connected to the three phase pulse width modulation PWM current source converter CSC. The input of AC-AC converters are modulated using high frequency square wave 20 kHz with 50% duty cycle. The output of the three phase current source converter is controlled with selective harmonic elimination SHE pulse width modulation PWM technique with 5<sup>th</sup>, 7<sup>th</sup>, 11<sup>th</sup>, 13<sup>th</sup> harmonics elimination. It is shown that the utility line currents are of high quality with the elimination of lower order harmonic currents. The proposed approach has the advantage of higher power density, absence of electrolytic capacitors, higher frequency isolation, and higher input current quality. Simulation results are presented on 120 kW solar PV system employing 1500 V DC. Experimental results for a scale down 1 kW laboratory prototype are discussed too.

---

\*\* Part of this section is reprinted with permission from:  
© 2020 IEEE. S. Sabry and P. Enjeti, "High Frequency Integrated Solid State Transformer (SST) for Utility Interface of Solar PV / Battery Energy Storage Systems," *2020 IEEE Applied Power Electronics Conference and Exposition (APEC)*, New Orleans, LA, USA, 2020, pp. 546-553.

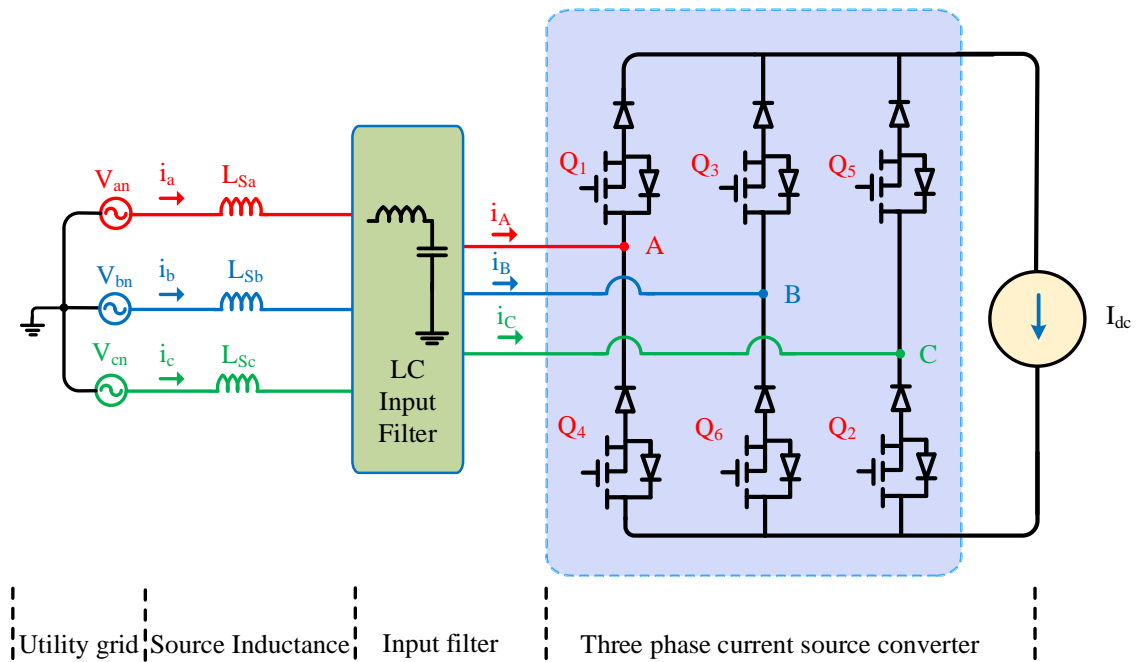
#### 4.1. Introduction

Worldwide electrical consumption is rapidly increasing, which is leading to rise demand on renewable energy systems. The growth of sharing in 2000 was about 1%, while in 2018 increased to 26%. Most of the power sharing comes from solar systems. This motivates most countries to develop and expand their renewable capacity base. According to the global energy statistic yearbook in 2019, renewable energies cover 36% of the power generation in Europe, 26% in China, 18% in the United States, India, and Japan [42]. Figure 4-1 shows the conventional PV grid-tied using line frequency 60 Hz transformer. The drawback of this approach is using the line frequency bulky transformer. In the recent past, interest in employing a solid-state transformer for utility interface has been increasing. This section proposed a new concept of a PWM controlled current source converter along with an integrated high frequency solid-state transformer. In general, there are two types of CSC; line commuted converter and PWM converter. The line commutated uses silicon control rectifier SCR whose commutation is assisted by a load while the PWM converter uses switches IGBT/MOSFET for the self-commutated [44,45]. The disadvantage of CSC is high conduction losses due to the series connection of the diode for the reverse blocking capability [42]. Employing wide bandgap devices such as Silicon carbide SiC, Gallium nitride Gan for the series blocking diode enhances the operation of the CSC due to their low losses [43]. The line commutated rectifier using SCR converter is discussed in [36]. Figure 4-2 shows a simple three phase grid-tied PWM CSC. The CSC has rules that have to be met. For instance, at any interval of time except the commutation time, there are two switches conducting, one from the top half and one from the bottom



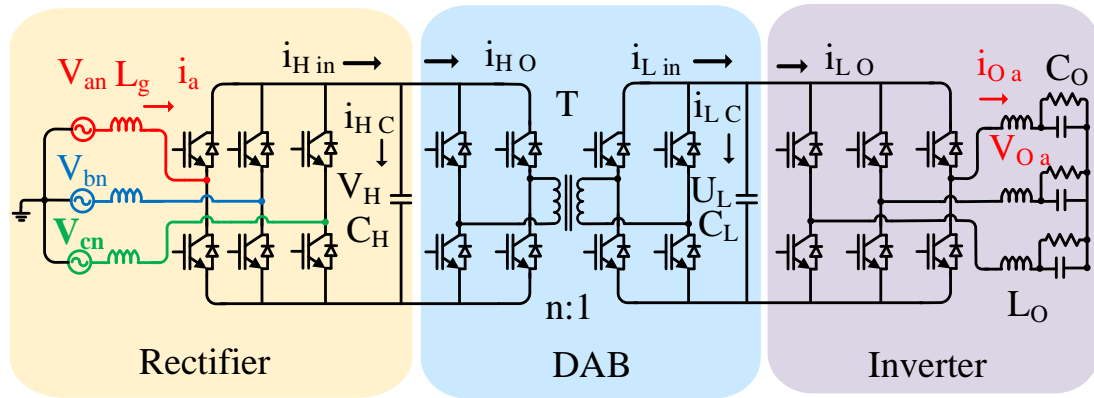
**Figure 4-1 Conventional solar PV grid-tied with line frequency (50/60) Hz transformer.**

half of the three phase converter to make sure the continuity of the DC current is valid [48]. A PWM controlled CSC is robust in operation with many advantages [46,50]. Selective harmonic elimination SHE is a pre-calculated modulation scheme which it has the capability to eliminate the unwanted low order harmonics of the input utility current. The switching angles are offline calculations in order to import them to a digital controller for the implementation [48,49]. Many approaches for the solid-state transformer have been proposed [51-63]. SST is called power electronic transformer, or smart transformer has some advantages, low size (volume), less weight, unity power factor, fault isolation, and insensitive to harmonics [51,53]. Replacing line frequency transformer by SST has been considered in such applications, for example, aircraft, traction where weight and volume are substantially significant, and good efficiency can be achieved [51]. The power electronic stage in the SST can be used to fully control voltages, currents, active and reactive power flow [63]. Thus, SST can be the key element of future smart distribution systems. In [51], a configuration of three phase SST for feedforward control was



**Figure 4-2 Three phase grid-tied current source converter.**

presented, as shown in Figure 4-3. This topology has multiple stages; rectifier, dual active bridge DAB, and inverter stage. In addition, it has dc-link  $C_H$  and  $C_L$ . Furthermore, the power transfer is limited since it uses one single phase transformer. In [52], a new concept of SST has been proposed using soft-switching technique, as shown in Figure 4-4. This concept has 12 main active devices and an auxiliary resonant circuit. In this approach, the three phase power transfer is also limited due to using one single phase transformer and it uses fly-back concept to transfer the power. In other words, the power is not directly coupled to the transformer. This section discusses the operation of the CSC using integrated SST and simple SHE PWM technique. The presented topology is shown in Figure 4-5. While the SST interfaced to the utility operates at a fixed frequency 20kHz,

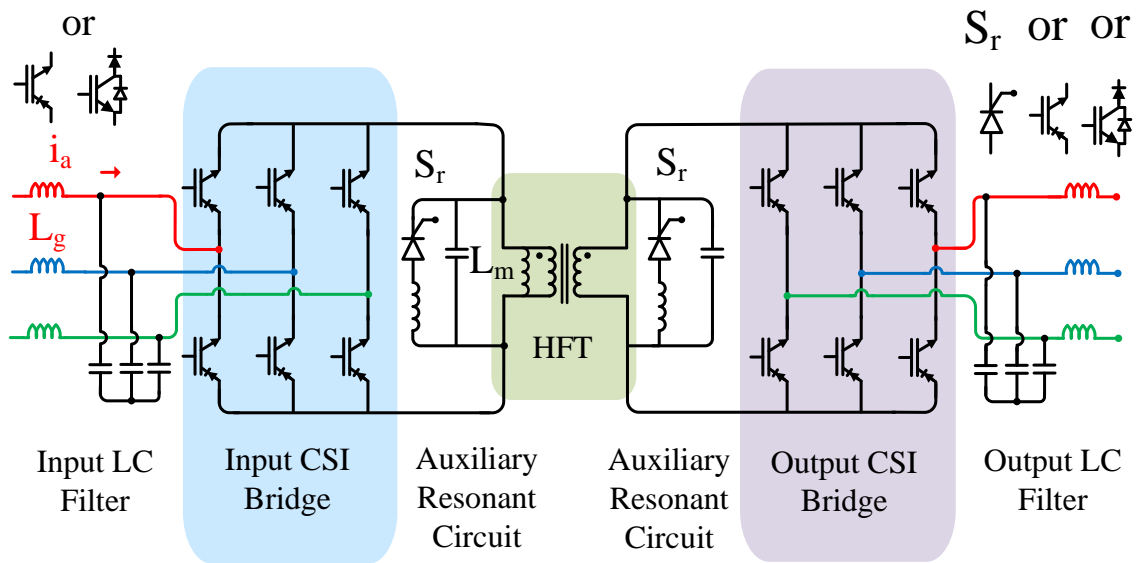


**Figure 4-3 Configuration of three phase solid-state transformer that has three stages rectifier, dual active bridge DAB and inverter stage. Adapted from [51].**

the PWM CSC is controlled with selective harmonic elimination SHE with 5<sup>th</sup>, 7<sup>th</sup>, 11<sup>th</sup>, and 13<sup>th</sup> eliminated to result in a near sinusoidal utility line current. It is important to combine high frequency 20kHz for SST to realize high power density with low frequency SHE control of PWM CSC. The aspect of selecting frequency separation in the control of the proposed converter is detailed in the input current analysis subsection. The proposed approach has the following advantages:

- 1) Galvanic isolation by SST is provided via a high frequency 20kHz, resulting in higher power density.
- 2) The approach is capable of bidirectional power flow. It could be used for grid-tied PV or electric vehicle EV battery fast-charging stations.
- 3) Low order harmonics in the utility line current are eliminated, improving power quality.



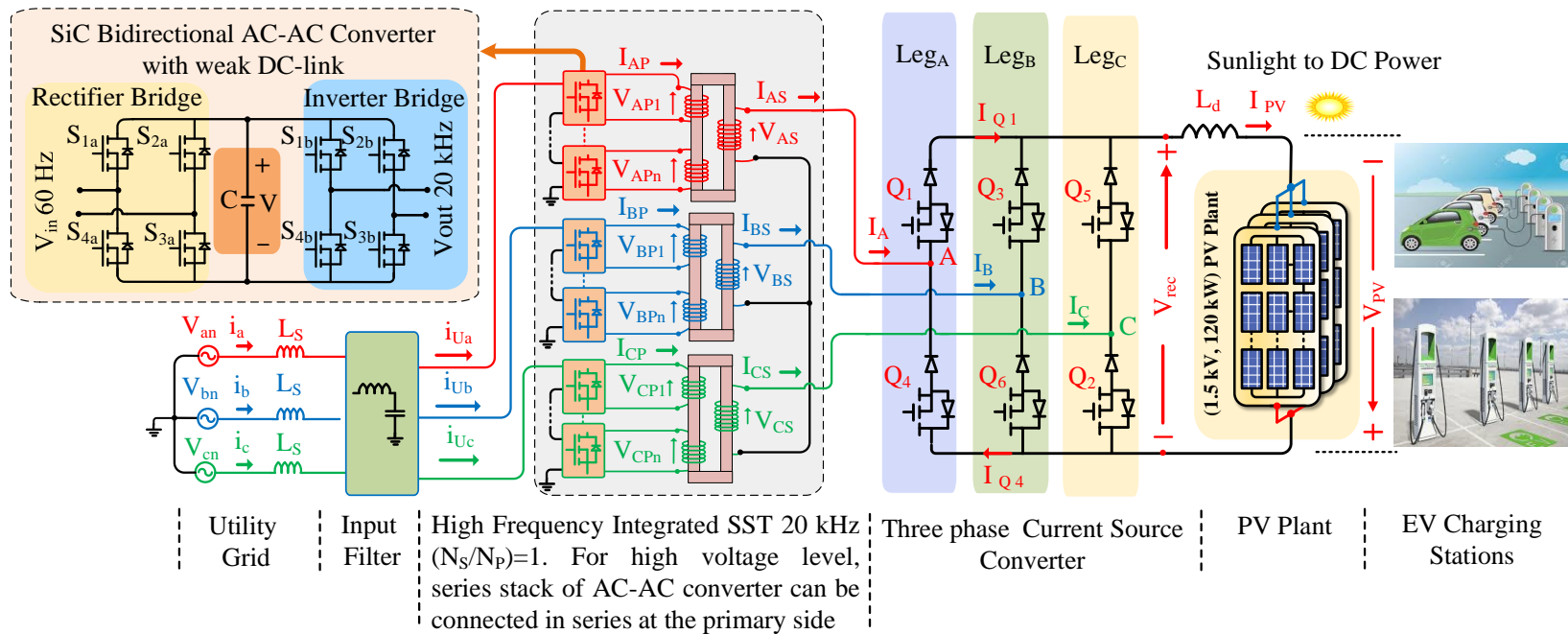


**Figure 4-4 Configuration of three phase soft-switching solid-state transformer. Adapted from [52].**

- 4) No electrolytic capacitors are employed, and the CSC offers a more robust operation with enhanced reliability.

#### 4.2. Selective Harmonics Elimination Pulse Width Modulation SHE PWM

The SHE (Programmable) PWM does not have a carrier signal, as shown in Figure 4-6. For the optimization function, many objective functions can be used, such as selective harmonic elimination, Minimum total harmonics distortion THD, reduced acoustic noise, minimum losses, and torque pulsations. One of the objective functions could be a selective harmonics elimination. The switching angles are pre-calculated and defined between  $(0 \text{ to } \frac{\pi}{2})$  degree, as stated in equation (4.1) [49].



**Figure 4-5 Proposed topology of bidirectional power flow current source converter using high frequency integrated solid-state transformer SST for utility interface of solar PV / battery energy storage systems. Reprinted with the permission from © 2020 IEEE [48].**

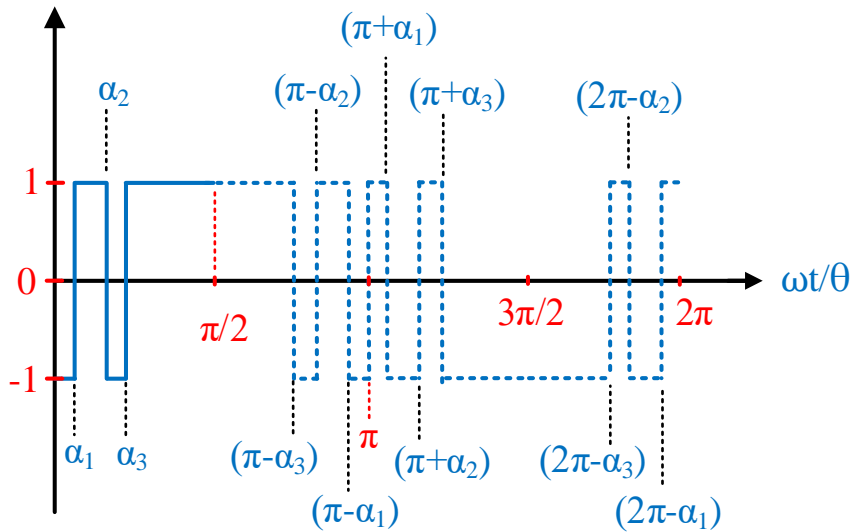
From  $(\frac{\pi}{2}$  to  $\pi$ ), the same switching angles are going to be folded, and between  $(\pi$  to  $2\pi$ ) are going to be the mirror for the first half cycle, except it is negative. If the condition of equation (4.1) is met, then the Fourier series coefficients can be written as given by (4.2-4.4) and solved for an optimization function. N represents the number of the switching angles, (N-1) refers to the number of harmonics to be eliminated [47].

$$\alpha_1 < \alpha_2 < \alpha_3 \dots < \alpha_N < \frac{\pi}{2} \tag{4.1}$$

$$a_0 = 0 \tag{4.2}$$

$$a_n = \frac{4}{n\pi} \left[ 1 + 2 \sum_{k=1}^N (-1)^k \cos(k\alpha_k) \right] \tag{4.3}$$

$$b_n = 0 \tag{4.4}$$



**Figure 4-6 Line to neutral switching pattern for one cycle that has three angles ( $\alpha_1$ ,  $\alpha_2$ ,  $\alpha_3$ ) to eliminate the (5<sup>th</sup>,7<sup>th</sup>) harmonics and control the fundamental amplitude ( $a_1$ ). Reprinted with the permission from © 2020 IEEE [48].**

The advantages of the SHE PWM technique are; reducing the switching frequency compare to the conventional sin PWM to achieve the same THD performance, it is suitable for high power application where the switching frequency is limited due to high losses, over modulation can be achieved. The bn coefficient is zero because it is an odd function and it has quadratic symmetry. Solving the non-linear transcendental equations (4.5) for the angles ( $\alpha_1, \alpha_2, \dots, \alpha_N$ ) is explained in [49]. The switching angles to eliminate the low order harmonics 5<sup>th</sup>, 7<sup>th</sup>... up to N-1 are listed in Table 4-1. In order to control the fundamental amplitude waveform ( $a_1$ ), an additional angle is assigned ( $\alpha_N$ ). For the phase “b” and “c”, the angles are going to be the same except they are phase shifted by 120 degree respectively.

$$\begin{bmatrix} 2 \cos(\alpha_1) & -2 \cos(\alpha_2) & \dots & 2(-1)^{N+1} \cos(\alpha_N) \\ 2 \cos(5\alpha_1) & -2 \cos(5\alpha_2) & \dots & 2(-1)^{N+1} \cos(5\alpha_N) \\ \vdots & \vdots & & \vdots \\ 2 \cos(x_1) \alpha_1 & -2 \cos(x_1) \alpha_1 & \dots & 2(-1)^{N+1} \cos(x_1) \alpha_1 \end{bmatrix} = \begin{bmatrix} \frac{\pi \alpha_1}{4} + 1 \\ 1 \\ \vdots \\ 1 \end{bmatrix} \quad (4.5)$$

**Table 4-1 Switching angles for line to neutral selective harmonic elimination for different objective functions including control the fundamental amplitude ( $a_1$ ).**

Fundamental Amplitude ( $a_1$ )	$\alpha_1$	$\alpha_2$	$\alpha_3$	$\alpha_4$	$\alpha_5$	Harmonics Eliminated
1.18	8.240	23.278	26.835	-	-	5 <sup>th</sup> and 7 <sup>th</sup>
1.0	14.85	37.60	44.08	-	-	
0.5	22.99	32.29	56.68	-	-	
0.25	26.57	32.29	56.68	-	-	
1.15	7.89	22.54	25.64	76.93	77.91	5 <sup>th</sup> , 7 <sup>th</sup> , 11 <sup>th</sup> , 13 <sup>th</sup>
1	7.05	24.39	29.83	69.83	73.25	
0.5	3.65	22.78	35.54	64.42	76.21	

Figure 4-6 shows the line to neutral switching scheme that has all the tripled harmonics. For the line to line waveforms, all tripled odd harmonics can be eliminated by the concept of three phase system  $120^0$  phase-shift, as explained by [48]. The unwanted low order harmonics are eliminated up to the first dominant harmonic using the objective function of the selected low order harmonics.

### **4.3. Proposed High Frequency Integrated Solid-State Transformer with Selective Harmonics Elimination Technique for Utility Interface**

The proposed topology of high frequency integrated SST concept for utility interface of solar or battery energy storage system is shown in Figure 4-5. The analysis of the presented topology is divided into the following parts: bidirectional AC-AC converter, high frequency transformer, three phase SHE PWM current source converter.

#### **4.3.1. Bidirectional AC-AC Converter**

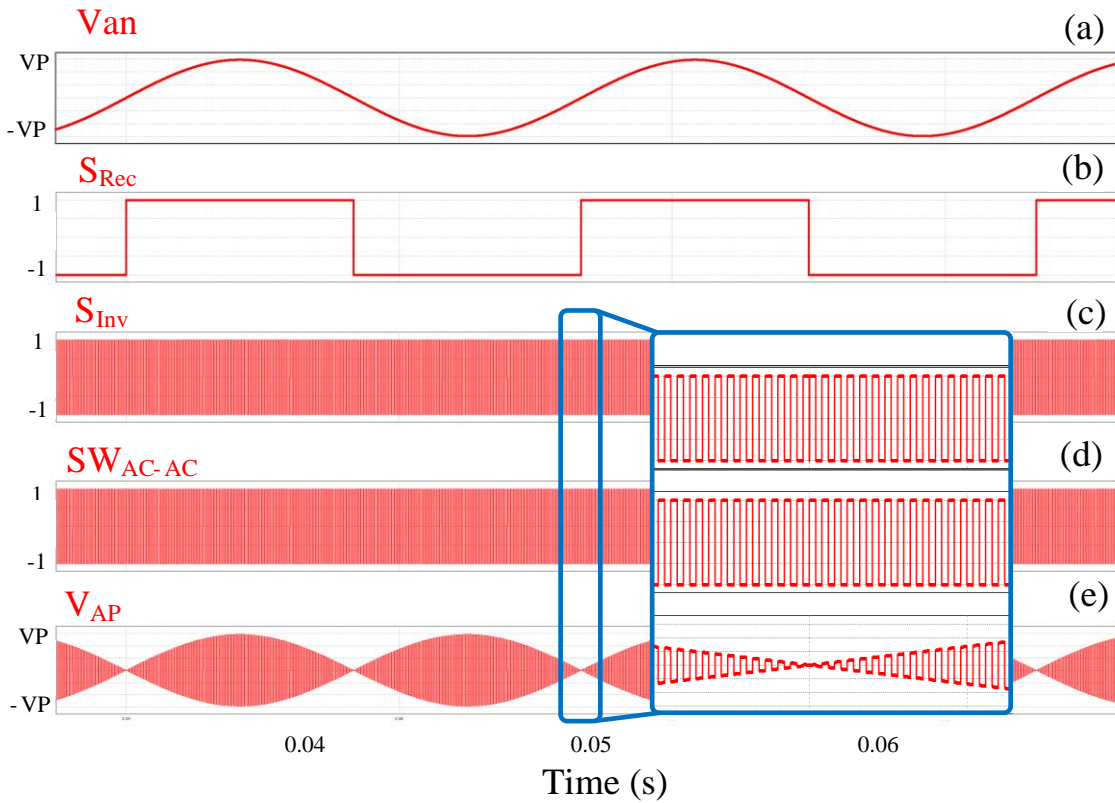
The proposed topology that is shown in Figure 4-5 consists of three bidirectional AC-AC converters. Each one composes a single phase bridge rectifier, small film capacitor (weak dc-link 5 uF), and followed by a full bridge inverter. The three phase utility input voltages are given by (4.6-4.8),  $\omega_s$  is the line frequency. The bridge rectifier of the AC-AC converter is switched at line frequency with a switching function  $S_{Rec}$ , as shown in Figure 4-7 (b) and given by (4.9), which means low switching losses. However, the inverter bridge's switching function  $S_{Inv}$  is a high frequency 20 kHz square wave 50% duty cycle, as demonstrated in Figure 4-7 (c) and given by (4.10).

$$V_{an} = \sqrt{\frac{2}{3}} V_{LL} \sin(\omega_s \cdot t) \quad (4.6)$$

$$V_{bn} = \sqrt{\frac{2}{3}} V_{LL} \sin(\omega_s \cdot t - \frac{2\pi}{3}) \quad (4.7)$$

$$V_{cn} = \sqrt{\frac{2}{3}} V_{LL} \sin(\omega_s \cdot t + \frac{2\pi}{3}) \quad (4.8)$$

The switching function of the inverter bridge is switched in such a way that the overall switching function of the three AC-AC converters is going to be the same square wave high frequency with fundamental frequency  $\omega_{HF}$  20 kHz 50% duty cycle ( $D=0.5$ ). The overall AC-AC converter switching function  $SW_{AC-AC}$  is shown in Figure 4-7 (d) and given by (4.11). The high frequency AC link at the output of the AC-AC converter for the phase “a”  $V_{AP}$  is given by (4.12) and shown in Figure 4-7(e).  $V_{AP}$  is generated by multiplying the input line frequency utility voltage  $V_{an}$  with the overall high frequency switching function  $SW_{AC-AC}$  (see Figure 4-7). The output voltage of the converter is applied to the primary windings of the high frequency transformer. From equation (4.12), It can be seen that the fundamental voltage of  $V_{AP}$  depends mainly on  $\omega_{HF}$ . Evidently, the transformer works at 20 kHz, which results in reducing the size of its core and leads to improve the power density of the overall converter. Since all three AC-AC converters use the same high frequency square wave 20 kHz  $\omega_{HF}$ ,



**Figure 4-7 AC-AC converter switching functions (a) line to neutral input voltage  $V_{an}$  (b) line frequency switching function for the rectifier bridge  $S_{Rec}$ , (c) high frequency switching function for the inverter bridge  $S_{Inv}$ , (d) switching function for the overall AC-AC converter  $SW_{AC-AC}$ , (e) phase “a” high frequency output voltage AC-AC converter  $V_{AP}$ .**

but their input line frequency voltages are shifted by 120 degree. Thus, the high frequency link  $V_{BP}$ ,  $V_{CP}$  that associated with phase “b”, and “c” respectively are going to be the same, except they are displaced by 120 degree to each other.

$$S_{Rec} = \frac{4}{\pi} \sum_{n=1,3,5,7,\dots}^{\infty} \frac{1}{n} \sin(n \cdot \omega_s \cdot t). \quad (4.9)$$

$$S_{Inv} = \sum_{n=1,3,5,\dots}^{\infty} \frac{1}{n} \sin(n. \omega_{HF}. t) \quad (4.10)$$

$$SW_{AC-AC} = S_{Rec} \times S_{Inv} = \frac{4}{\pi} \sum_{n=1,3,5,7,\dots}^{\infty} \frac{1}{n} \sin(n. \pi. D). \sin(n. \omega_{HF}. t) \quad (4.11)$$

$$\begin{aligned} V_{AP} &= V_{an} \times SW_{AC-AC} \\ &= \sqrt{\frac{2}{3}} V_{LL} \sum_{n=1,3,5,7,\dots}^{\infty} \frac{2}{n\pi} \sin(n. \pi. D). \sin([n. \omega_{HF} \pm \omega_s]. t) \end{aligned} \quad (4.12)$$

The modulation scheme for the AC-AC converter is simple and easy to build. The most substantial step is to detect the zero-crossing points for the three phase input voltages to synchronize the modulation. The maximum voltage of the AC-AC converter occurs at (D=0.5). For (D>0.5), there will be a short circuit, which means this state would be prohibited. For (D<0.5), zero states will appear at the output voltage of the AC-AC converter, which results in reducing the output voltage of the AC-AC converter. Series stacks of AC-AC converter can be used for high voltage level (see Figure 4-5).

#### 4.3.2. High Frequency Transformer

The second part of the presented topology is the high frequency transformer HFT. As shown in Figure 4-5, it has three primary windings and three secondary windings with unity turns ratio. It is a simple star to star connection. The primary side of the HFT is interfaced with the output of the AC-AC converters while the secondary side is connected to the three phase CSC. The HFT substantially affects the power density of the overall

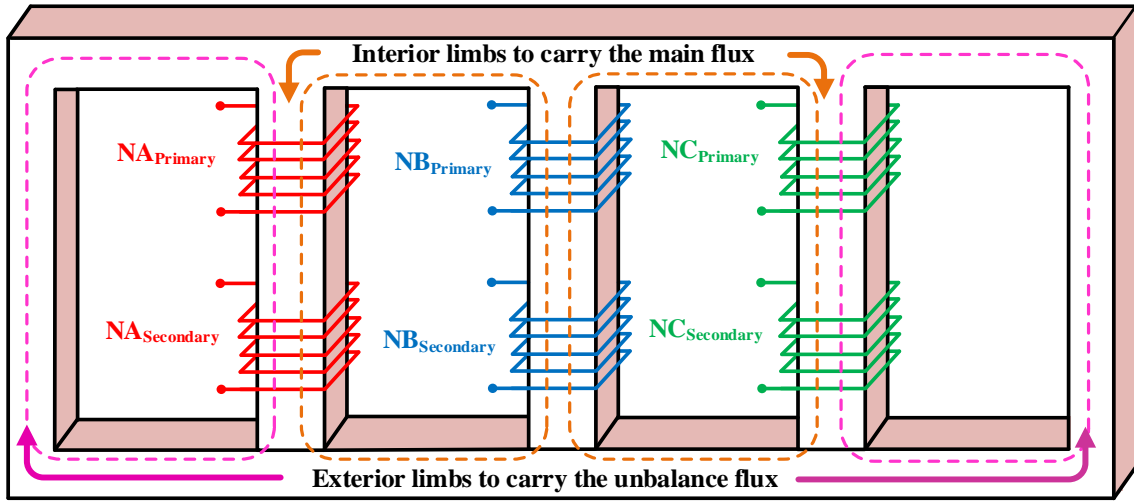


presented topology. Even though increasing the transformer frequency operation will improve the power density, however, working at high frequency will increase the AC-AC converter's losses and the transformer's core losses. The switching frequency should be selected without sacrificing the efficiency (high losses) in order to improve the power density. The second factor to improve power density is choosing a suitable magnetic core material. Silicon steel core material would be preferable for frequency range less than 1 kHz while Amorph core material would be suitable for frequency range between (1-2) kHz according to [64]. For high frequency operation 20 kHz, Ferrite core material should be chosen because silicon steel material absorbs high losses for operating frequency more than 1 kHz [65]. The transformer core structure has five limbs, as shown in Figure 4-8. The function of the outer limbs is to prevent the core saturation by carrying the unbalanced flux lines [66].

### **4.3.3. Three Phase Current Source Converter CSC Using Selective Harmonics**

#### **Elimination SHE Pulse Width Modulation PWM**

The last part of the presented topology is the current source converter CSC using SHE PWM. The CSC consists of six unidirectional switches (switch in series with a diode). This converter has been interfaced with the secondary side of the HFT (see Figure 4-5). Each switch follows by a diode to enable the reverse blocking voltage capability and enforce the current to flow in one direction. These diodes should be able to switch at



**Figure 4-8 Five limbs high frequency transformer, it has two exterior limbs to carry the unbalanced flux lines and three interior limbs for the main flux lines. Reprinted with the permission from © 2020 IEEE [48].**

high frequency 20kHz, and they should have fast recovery time to avoid high switching losses. The presented topology uses simple selective harmonics elimination pulse width modulation (programmable PWM) to eliminate the low order harmonics ( $5^{\text{th}}, 7^{\text{th}}, 11^{\text{th}}, 13^{\text{th}}$ ) from the unfiltered input utility current  $i_{Ua}$ ,  $i_{Ub}$ ,  $i_{Uc}$  (see Figure 4-5). The advantages of SHE PWM are mentioned in [48,49]. After selecting up to which low order harmonic to be eliminated, equation (4.5) has to be solved in order to find the angles. Table 4-1 demonstrates the switching angles for different selective harmonics objective functions and fundamental amplitude value ( $a_1$ ). Once the angles are defined, a bipolar line to neutral switching function  $S_1$  is defined. This switching function would be for phase “a”. The associated switching functions for phase “b”  $S_2$ , and “c”  $S_3$  would be the same, except they are shifted by 120 degree respectively. Figure 4-9 shows the line to neutral bipolar switching function  $S_1$ ,  $S_2$ , and  $S_3$ . These switching functions are used to eliminate the

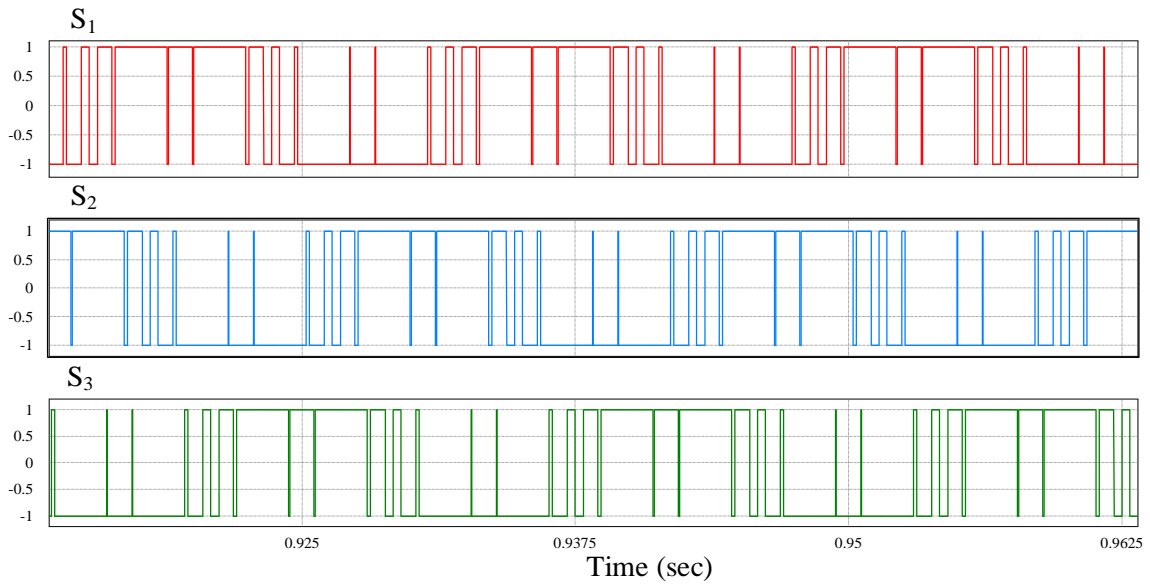
(5<sup>th</sup>,7<sup>th</sup>,11<sup>th</sup>,13<sup>th</sup>) harmonics and set the fundamental amplitude to ( $a_1=1.15$ ). However, these functions  $S_1, S_2, S_3$  have all tripled harmonics as shown in Figure 4-10. In order to eliminate the tripled harmonics, a new set of line to line unipolar switching functions  $S_a, S_b, S_c$  can be found as given by (4.13 - 4.15) and illustrated in Figure 4-11. The unipolar switching functions  $S_a, S_b, S_c$  are the desired waveforms for the unfiltered input utility currents  $i_{u_a}, i_{u_b}, i_{u_c}$  (see Figure 4-5).

$$S_a = S_1 - S_2 \quad (4.13)$$

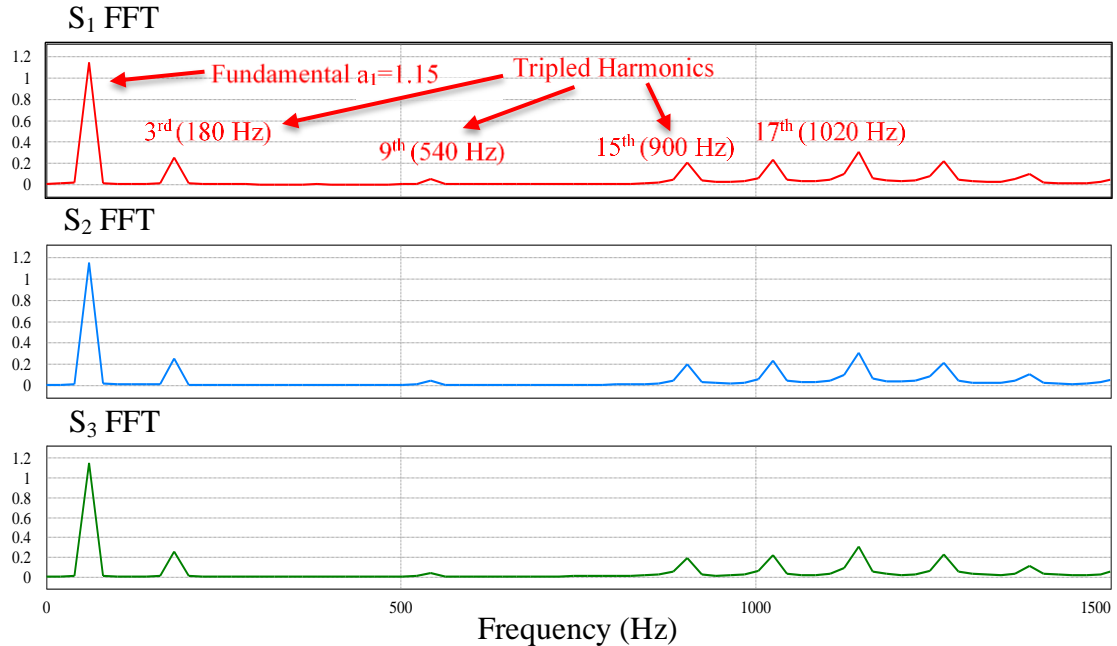
$$S_b = S_2 - S_3 \quad (4.14)$$

$$S_c = S_3 - S_1 \quad (4.15)$$

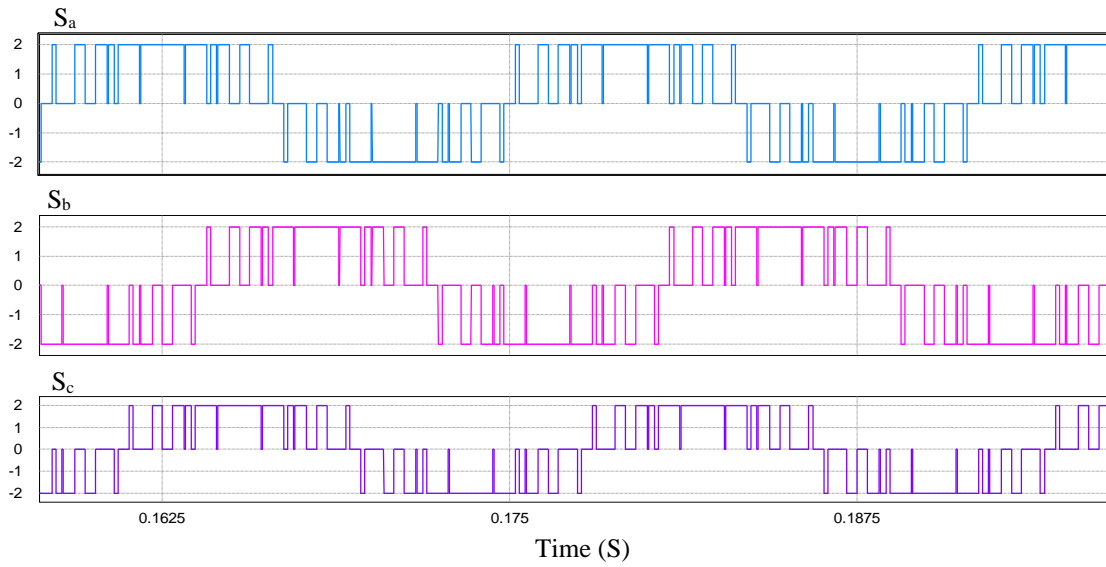
The sum of these unipolar switching functions should be added to zero for three phase balanced condition. The FFT spectrum of these switching functions is depicted in Figure 4-12. All tripled harmonics have been removed due to the nature of the three phase system. The first dominant harmonics is (17<sup>th</sup> =1020 Hz). The switching condition of the three phase CSC are going to be the unipolar switching functions  $S_a, S_b, S_c$  multiplied by the switching function of the AC-AC converter  $SW_{AC-AC}$  (see in equations 4.16 - 4.18). To find the gating signals condition of leg<sub>A</sub> CSC (see Figure 4-5), when the switching function  $SW_A$  is positive, the switch  $Q_1$  of the CSC is turned on while if  $SW_A$  is negative, the switch  $Q_4$  is turned on. When  $SW_A$  is zero, both  $Q_1$  and  $Q_4$  should be turned off. For Leg<sub>B</sub> and Leg<sub>C</sub>, the conduction sates can be found in the same manner.



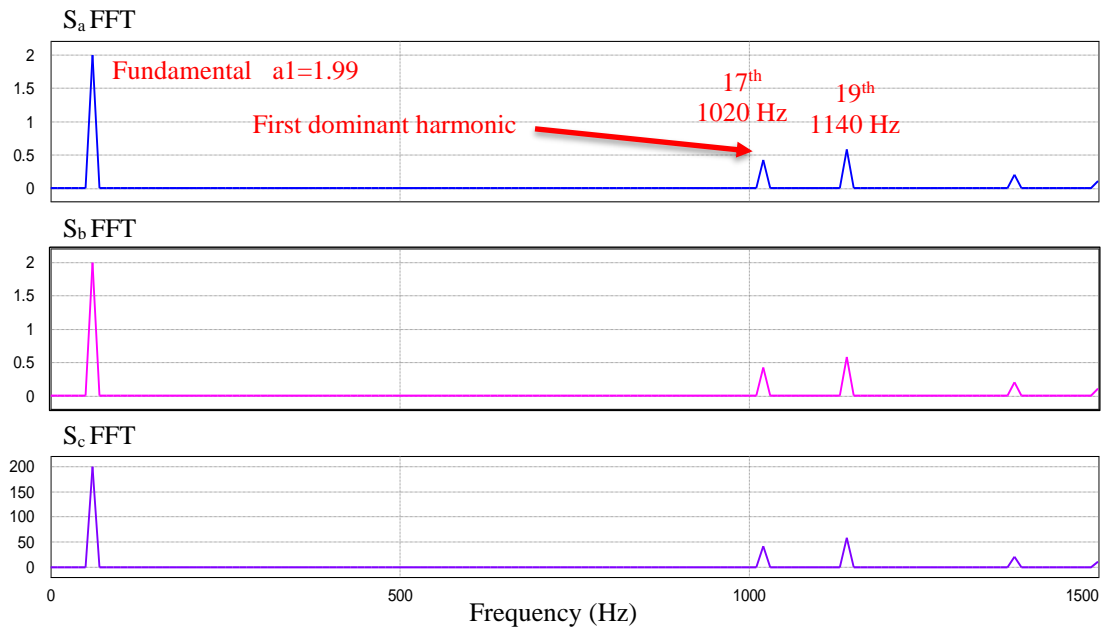
**Figure 4-9** Line to neutral bipolar switching functions ( $S_1$ ,  $S_2$ ,  $S_3$ ) to eliminate the (5<sup>th</sup>, 7<sup>th</sup>, 11<sup>th</sup>, 13<sup>th</sup>), ( $\alpha_1 = 7.89^\circ$ ,  $\alpha_2 = 22.54^\circ$ ,  $\alpha_3 = 25.64^\circ$ ,  $\alpha_4 = 76.93^\circ$ ,  $\alpha_5 = 77.91^\circ$ ). Fundamental amplitude value is ( $a_1=1.15$ ) (see Table 4-1).



**Figure 4-10** FFT analysis of line to neutral bipolar switching functions ( $S_1$ ,  $S_2$ ,  $S_3$ ). The eliminated harmonics are (5<sup>th</sup>, 7<sup>th</sup>, 11<sup>th</sup>, 13<sup>th</sup>). Note that the tripled harmonics are there.



**Figure 4-11** Line to line unipolar switching functions ( $S_a$ ,  $S_b$ ,  $S_c$ ) to eliminate the (5<sup>th</sup>,7<sup>th</sup>,11<sup>th</sup>,13<sup>th</sup>) and all tripled harmonics (see equations 4.13-4.15).



**Figure 4-12** FFT analysis of the line to line unipolar switching function ( $S_a$ ,  $S_b$ ,  $S_c$ ) to eliminate the (5<sup>th</sup>,7<sup>th</sup>,11<sup>th</sup>,13<sup>th</sup>) harmonics. Note that there are no tripled harmonics.

$$SW_A = S_a \times SW_{AC-AC} \quad (4.16)$$

$$SW_B = S_b \times SW_{AC-AC} \quad (4.17)$$

$$SW_C = S_c \times SW_{AC-AC} \quad (4.18)$$

For the SHE PWM, there are some moments of the overall switching function ( $SW_A + SW_B + SW_C = 0$ ). At those moments, a freewheeling path should be provided by activating one of the CSC's legs. For the rectification mode operation, the output voltage of this converter is demonstrated by (4.19), and the average DC output voltage is given by (4.20).

$$V_{rect} = SW_A \times V_{an} + SW_B \times V_{bn} + SW_C \times V_{cn} \quad (4.19)$$

$$V_{rect,AVE} = \frac{4}{3} \times a_1 \times V_{LL} \quad (4.20)$$

#### 4.4. Input Current Analysis

The unfiltered input current for the phase “a” is given by (4.21).  $I_{AP}$  is the phase “a” transformer primary winding current (see Figure 4-5). To find the relationship between the primary and secondary current, the transformer volt-ampere balanced can be used as given by (4.22).  $I_{AP}$  is the same as  $I_{AS}$  since the transformer has unity turns ratio. The Fourier series coefficients of the line to neutral switching function  $S_1$  are given by equations (4.23 - 4.25).  $S_1$  has all tripled harmonics as given by (4.26) and shown in Figure 4-10. However, the line to line unipolar switching function  $S_a$  for the phase “a” that is

shown in Figure 4-11 does not have tripled harmonics as given by (4.27) and shown in Figure 4-12.

$$I_{Ua} = SW_{AC-AC} \times I_{AP} \quad (4.21)$$

$$N_{PA} \times I_{AP} = N_{SA} \times I_{AS} \quad (4.22)$$

$$a_0 = \frac{1}{T} \int_0^T S_1(t) \cdot dt = 0 \quad (4.23)$$

$$a_n = \frac{2}{T} \int_0^T S_1(t) \cdot \cos\left(\frac{2\pi \cdot n \cdot t}{T}\right) \cdot dt = 0 \quad (4.24)$$

$$b_n = \frac{2}{T} \int_0^T S_1(t) \cdot \sin\left(\frac{2\pi \cdot n \cdot t}{T}\right) \cdot dt \quad (4.25)$$

$$S_1(t) = \sum_{n=1,3,9,17,19,23,29..etc}^{\infty} b_n \sin(n \cdot \omega_s \cdot t) \quad (4.26)$$

$$S_a(t) = \sum_{n=1,17,19,23,29..etc}^{\infty} b_n \sin(n \cdot \omega_s \cdot t) \quad (4.27)$$

$S_a(t)$  is the designed switching function for the unfiltered input current for the phase “a”

Therefore,

$$\begin{aligned} I_A(t) &= \sum_{n=1,17,19,23,29..etc}^{\infty} I_n \sin(n \cdot \omega_s \cdot t) = I_1 \sin(\omega_s \cdot t) \\ &+ I_{17} \sin(17 \cdot \omega_s \cdot t) + I_{19} \sin(19 \cdot \omega_s \cdot t) + I_{23} \sin(23 \cdot \omega_s \cdot t) \\ &+ I_{29} \sin(29 \cdot \omega_s \cdot t) + \dots \text{Higher order terms.} \end{aligned} \quad (4.28)$$

After the fundamental, the first dominant harmonic appears at 17<sup>th</sup> (1020 Hz). The transformer's primary winding current is given by (4.29).  $SW_{AC-AC}$  is the high frequency switching function of the overall AC-AC converter, which is provided by (4.11).

$$I_{AP}(t) = SW_{AC-AC} \times I_A(t) \quad (4.29)$$

Plugging equations (4.11) and (4.28) into (4.29) yields:

$$I_{AP}(t) = SW_{AC-AC} \times \begin{bmatrix} I_1 \sin(\omega_s \cdot t) & +I_{17} \sin(17 \cdot \omega_s \cdot t) \\ +I_{19} \sin(19 \cdot \omega_s \cdot t) & +I_{23} \sin(23 \cdot \omega_s \cdot t) \\ +I_{29} \sin(29 \cdot \omega_s \cdot t) & + \dots \text{High order terms} \end{bmatrix} \quad (4.30)$$

The overall unfiltered phase "a" current  $I_{Ua}$  can be determined by substituting (4.30) into (4.21)

$$I_{Ua}(t) = SW_{AC-AC} \times SW_{AC-AC} \times \begin{bmatrix} I_1 \sin(\omega_s \cdot t) + & I_{17} \sin(17 \cdot \omega_s \cdot t) \\ +I_{19} \sin(19 \cdot \omega_s \cdot t) & +I_{23} \sin(23 \cdot \omega_s \cdot t) \\ +I_{29} \sin(29 \cdot \omega_s \cdot t) & + \dots \text{High order terms} \end{bmatrix} \quad (4.31)$$

For 50% duty cycle ( $D=0.5$ ),

$$SW_{AC-AC} \times SW_{AC-AC} = [S_{Rec} \times S_{Inv}]^2 = \left[ \frac{4}{\pi} \sum_{n=1,3,5,7,\dots}^{\infty} \frac{1}{n} \sin(n \cdot \pi \cdot D) \cdot \sin(n \cdot \omega_{HF} \cdot t) \right]^2 = 1 \quad (4.32)$$

Therefore, simplifying the  $I_{Ua}$  further, yields to:



$$I_{Ua}(t) = \begin{bmatrix} I_1 \sin(\omega_s t) + & I_{17} \sin(17. \omega_s t) \\ +I_{19} \sin(19. \omega_s t) & +I_{23} \sin(23. \omega_s t) \\ +I_{29} \sin(29. \omega_s t) & + \dots \text{High order terms} \end{bmatrix} \quad (4.33)$$

Evidently, the unfiltered input current  $I_{Ua}$  for the phase “a” does not have the eliminated non-tripled low order harmonics (e.g., 5<sup>th</sup>, 7<sup>th</sup>, 11<sup>th</sup>, 13<sup>th</sup>). The mathematical analysis proves that the presented topology has good input current quality. Using the high frequency solid-state transformer won’t affect the input current quality instead of replacing the bulky line frequency transformer by a high frequency transformer which, results in improving the power density of the overall topology.

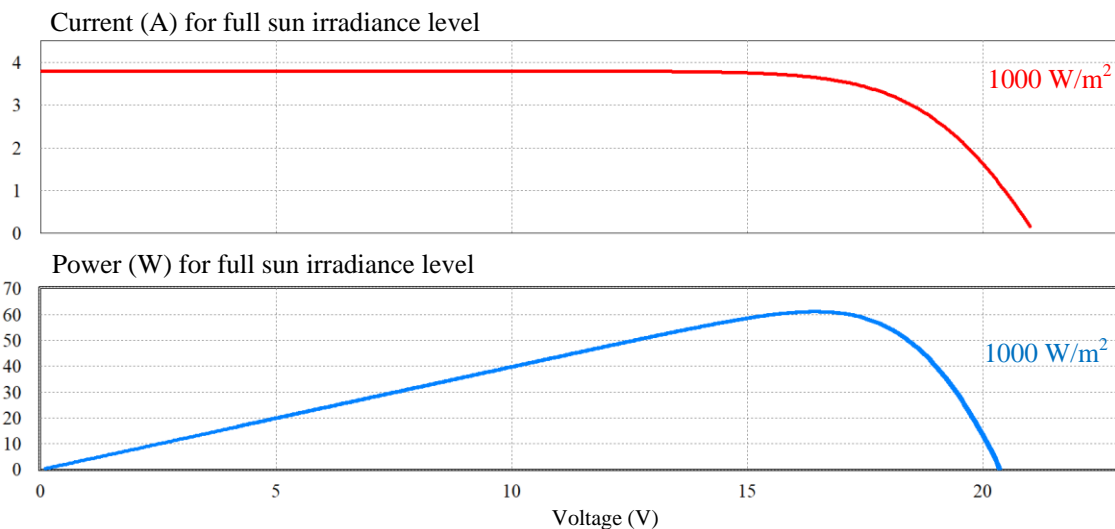
#### 4.5. Design Example

Many types of PV panels are available in the market [67,68]. According to the Solarex data sheet [67], the specification parameters for the one-panel solar cell are listed in Table 4-2. PV panel has been simulated using PSIM software. The IV and PV characteristic curves for one panel are shown in Figure 4-13. In order to design a PV farm (1.5 kV output DC voltage, 120 kW), a combination of series panels  $N_s=88$  and parallel strings  $N_p=23$  have to be connected. After connecting these combinations and simulating the PV farm using PSIM, the IV and PV characteristics curves for different sun irradiance levels are shown in Figure 4-14. The semiconductor device ratings for the proposed topology are listed in Table 4-3. Assuming the power factor is (0.95). For 120 kW power, the  $I_{PV}$  is given by (4.34). The high frequency transformer’s ratings are listed in Table 4-4.

**Table 4-2 Solarex one-panel parameters.**

Number of Cells $N_s$ per panel	36	Standard Light Intensity	1000 W/m
Ref. Temperature $T_{ref}$	25	Series Resistance $R_s$	0.008 Ohm
Shunt Resistance $R_{sh}$	1000	Short Circuit Current $I_{sc0}$	3.8 A
Saturation Current $I_{s0}$	$2.16 \times 10^{-8}$ A	Band Energy $E_g$	1.12
Identity Factor $A$	1.2	Temperature coefficient $C_t$	0.00247

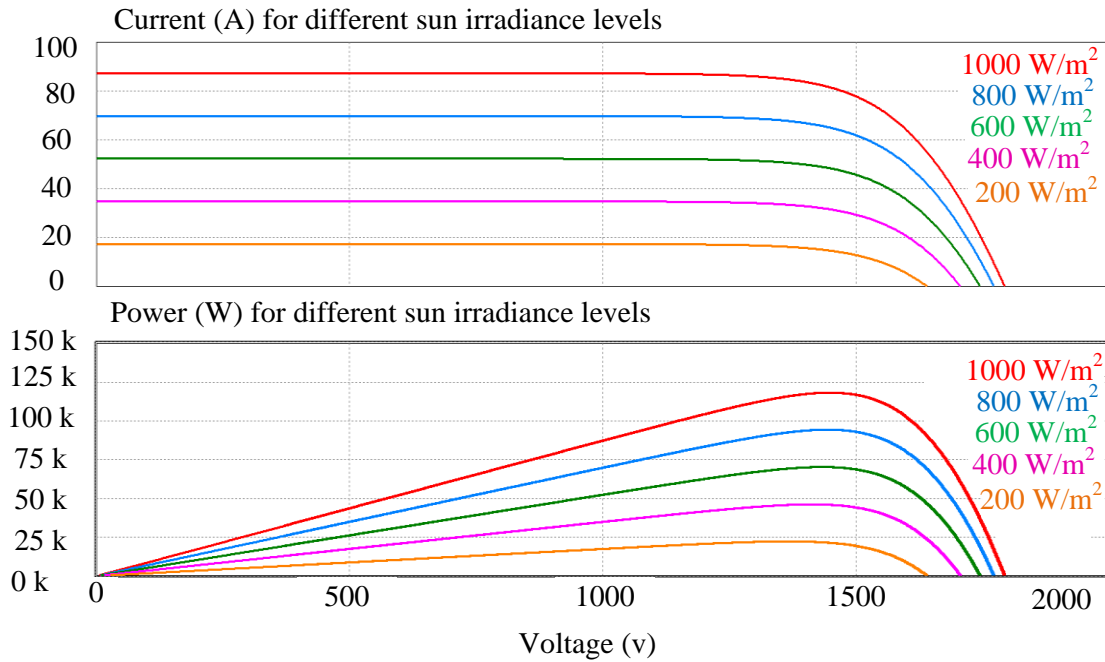
$$I_{PV} = \frac{P_{PV}}{V_{PV}} = \frac{120 \text{ kW}}{1.5 \text{ kV}} = 80 \text{ A} \quad (4.34)$$



**Figure 4-13 IV and PV characteristics for one-panel according to the Solarex data sheet for full sun irradiance level.**

#### 4.6. Simulation Results

The previous design example was simulated using PSIM software to verify the proposed concept. The specific parameters for the design example are listed in Table 4-5.



**Figure 4-14 IV and PV characteristics for the designed PV farm 1.5 kV, 120 kW for different sun irradiance levels.**

The high frequency transformer 20 kHz primary voltages  $V_{AP}$ ,  $V_{BP}$ ,  $V_{CP}$  are shown in Figure 4-15, and their FFT spectrum analysis are shown in Figure 4-16. It is clear that the dominant frequency of these voltages appears around 20 kHz, which implies that the transformer works at high frequency. Since the transformer works at high frequency, that is evident to decrease its core size and weight. For the three phase CSC, SHE PWM is used to eliminate the low order harmonics 5<sup>th</sup>, 7<sup>th</sup>, 11<sup>th</sup>, 13<sup>th</sup> from the utility input current. Equation (4.5) has to be solved first to find the set of switching angles ( $\alpha_1, \alpha_2, \alpha_3, \alpha_4, \alpha_5$ ) [48]. Multiple solution can be existed for the switching angles.

**Table 4-3 Semiconductor device ratings for the desing example of the presented topology in Figure 4-5.**

Switches	Rated parameters	Expression	Measured value for 120 kW
Rectifier bridge of the AC-AC converter	Peak voltage	$\sqrt{\frac{2}{3}} V_{LL}$	1004.29 Volt
	Peak current	$I_{PV}$	80A
	Rms current	$\frac{\sqrt{6} \cdot a_1}{4 \cdot \sqrt{2} \cdot PF} \cdot I_{PV}$	41.93A
Inverter bridge of the AC-AC converter	Peak voltage	$\sqrt{\frac{2}{3}} V_{LL}$	1004.29 Volt
	Peak current	$I_{PV}$	80A
	Rms current	$\sqrt{\frac{2}{\pi} \left( \frac{\pi}{12} + \frac{1}{4} \right)} I_{PV}$	45.66A
Three phase current source converter	Peak voltage	$\sqrt{2} V_{LL}$	1739.48
	Peak current	$I_{PV}$	80A
	Rms current	$\sqrt{\frac{2}{\pi} \left( \frac{\pi}{12} + \frac{1}{4} \right)} I_{PV}$	56.09

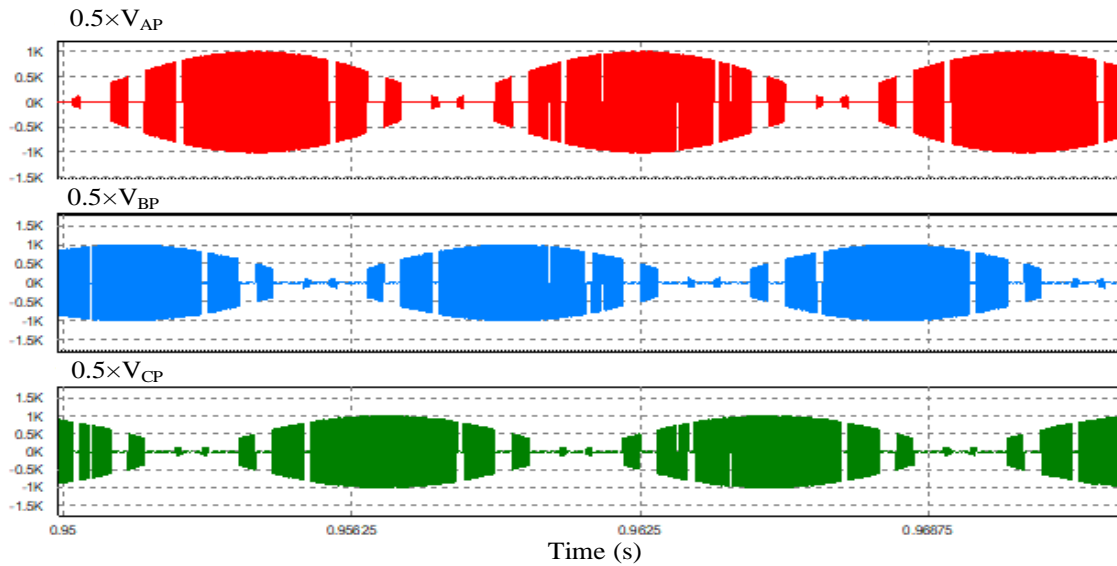
**Table 4-4 High frequency transformer ratings for the design example of the presented topology in Figure 4-5.**

Primary side windings	Voltage $V_{pri\ rms}$	$V_{LL} = 0.82 V_{PV}$
	Current $I_{pri\ rms}$	$0.8 I_{PV}$
Secondary side windings	Voltage $V_{sec\ rms}$	$V_{LL} = 0.82 V_{PV}$
	Current $I_{sec\ rms}$	$0.8 I_{PV}$
Volt-Ampere rating calculation		
Transformer VA		
$= \sum \left( \frac{V_{rms} I_{rms}}{2} \right) = \left( \frac{V_{LL} I_{PA}}{2} \right) \times 3 \times 2 = (0.82 V_{PV} 0.8 I_{PV}) \times 3$ $= 1.968 P_{Out}$		

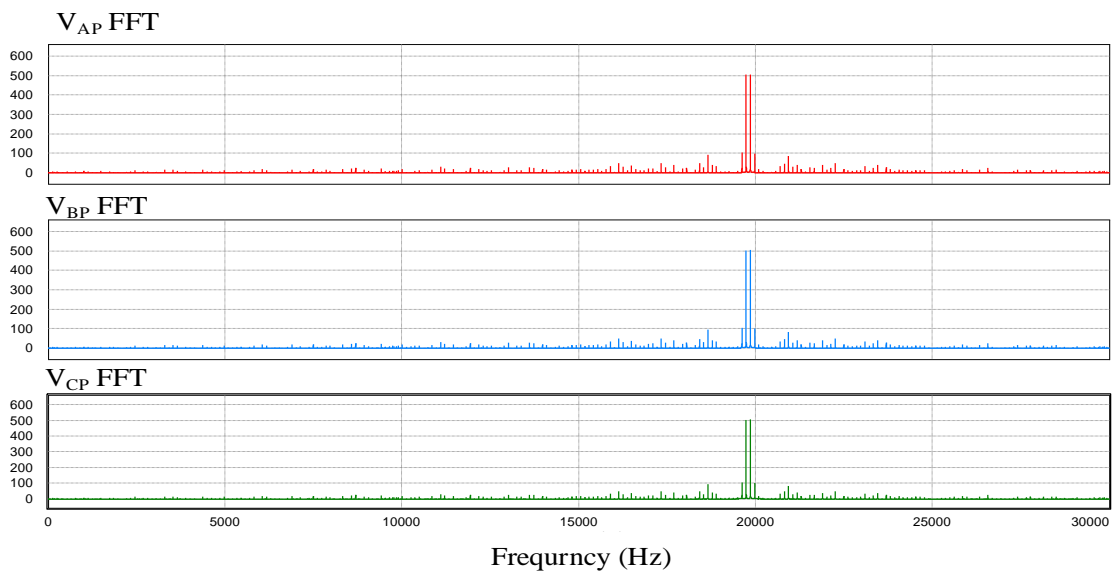
**Table 4-5 Simulation parameters for the design example of the proposed topology in Figure 4-5.**

Utility medium voltage	$V_{LL\ rms}$	2.4 kV
	Utility frequency	60 Hz
Output DC voltage	-1500 V DC	
AC-AC converter	Bridge rectifier switching frequency	60 Hz
	Bridge inverter Switching frequency	20 k Hz
Transformer turn ratio	Unity	Transformer frequency operation = 20 k Hz
PV farm specification	$V_{PV} = 1500$ V DC	$I_{PV} = 80$ A
	$P_{PV} = 120$ k W	
Dc-link inductor $L_d$	20 mH	

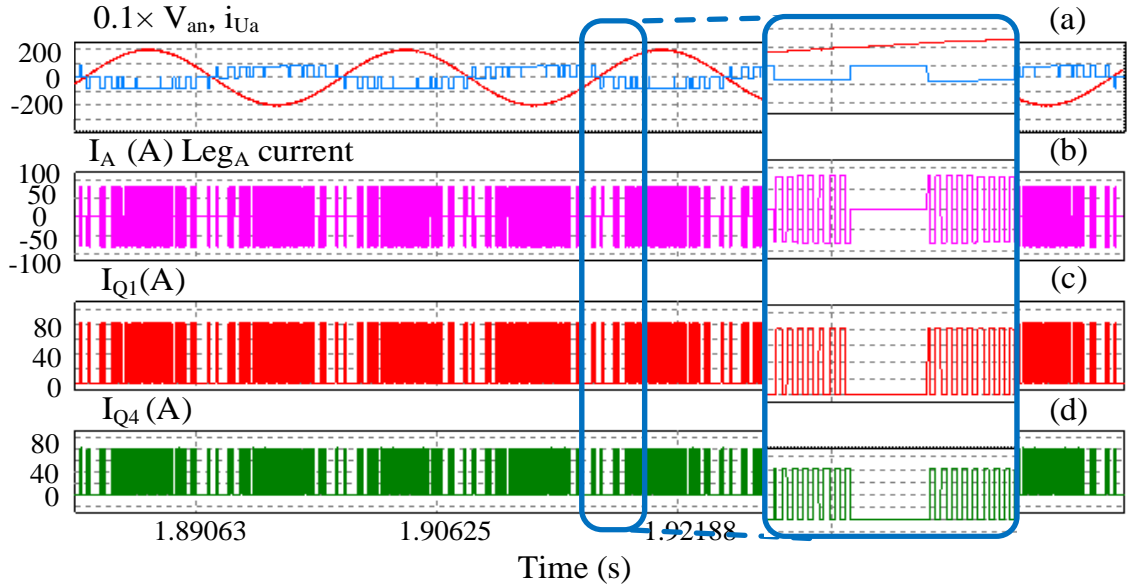
These sets of angles should satisfy the condition in equation (4.1). In this example ( $N=5$ ), which is the number of angles, ( $N-1=4$ ), which is the number of the unwanted low order harmonics that should be eliminated. Different sets of angles with different fundamental amplitudes are listed in Table 4-1. Figure 4-17 shows the current of LegA ( $I_A = I_{Q1} - I_{Q4}$ ) (see Figure 4-5),  $I_{Q1}$  is the current goes through the switch  $Q_1$  for the CSC and  $I_{Q4}$  is the current goes through the switch  $Q_4$ . Figure 4-18 shows the utility input voltage  $V_{an}$  along with associated unfiltered current for the phase “a”  $i_{Ua}$ , PV farm voltage  $V_{PV}=1500$  V, PV farm current  $I_{PV}=80$  A, output voltage of the CSC  $V_{rec} = -1500$ .  $V_{rec}$  is negative because the converter works as an inverter. There are some interval moments that all the gating signals of the current source converter should be zero. In this case, one of the current source converter’s legs should be turned on to provide a freewheeling path as shown in Figure 4-18 (d). The overall unfiltered input currents  $i_{Ua}$ ,  $i_{Ub}$ ,  $i_{Uc}$  along with the utility input voltages  $V_{an}$ ,  $V_{bn}$ ,  $V_{cn}$  are shown in Figure 4-19. The FFT analysis of the unfiltered input currents are shown in Figure 4-20. Evidently, the unfiltered input current dominant harmonic starts on the 17<sup>th</sup>, which is (1020 Hz). The CSC is working as an inverter because the overall input voltages and their associated current are out of phase. The power is injected into the utility grid.



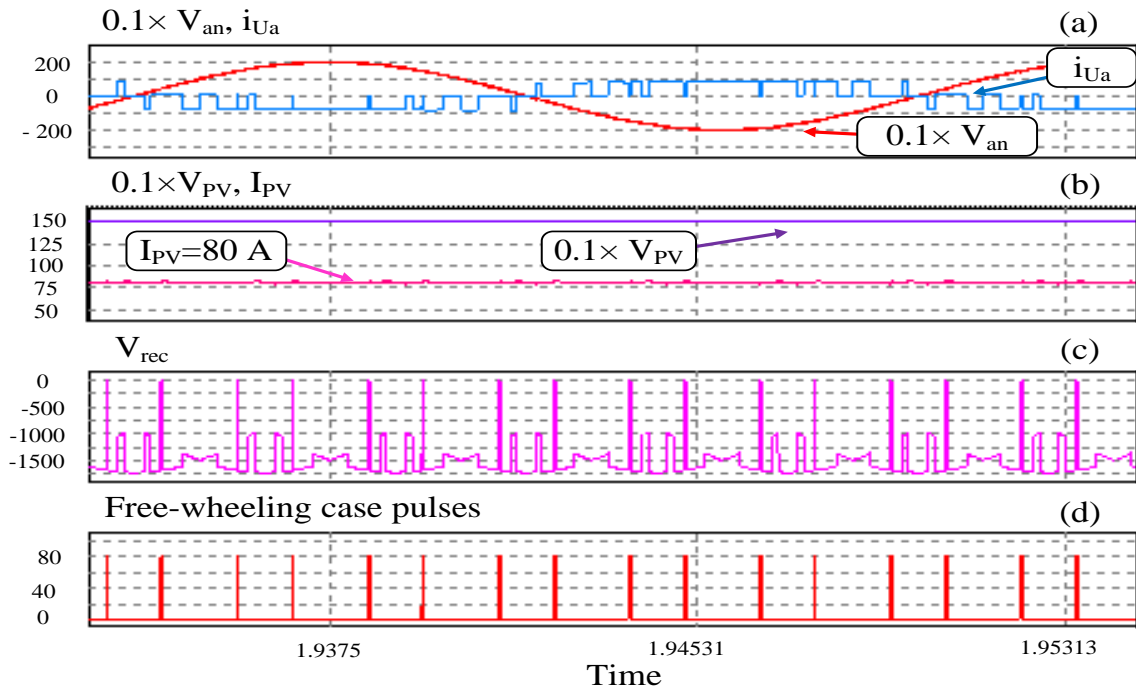
**Figure 4-15** Simulation results for the proposed converter (Figure 4-5): High frequency transformer primary voltages  $V_{AP}$ ,  $V_{BP}$ ,  $V_{CP}$ . Note the voltages have been scaled down by 2 for better resolution.



**Figure 4-16** Frequency spectrum for high frequency transformer primary voltages  $V_{AP}$ ,  $V_{BP}$ ,  $V_{CP}$ . Note the dominant frequency is around 20 kHz.

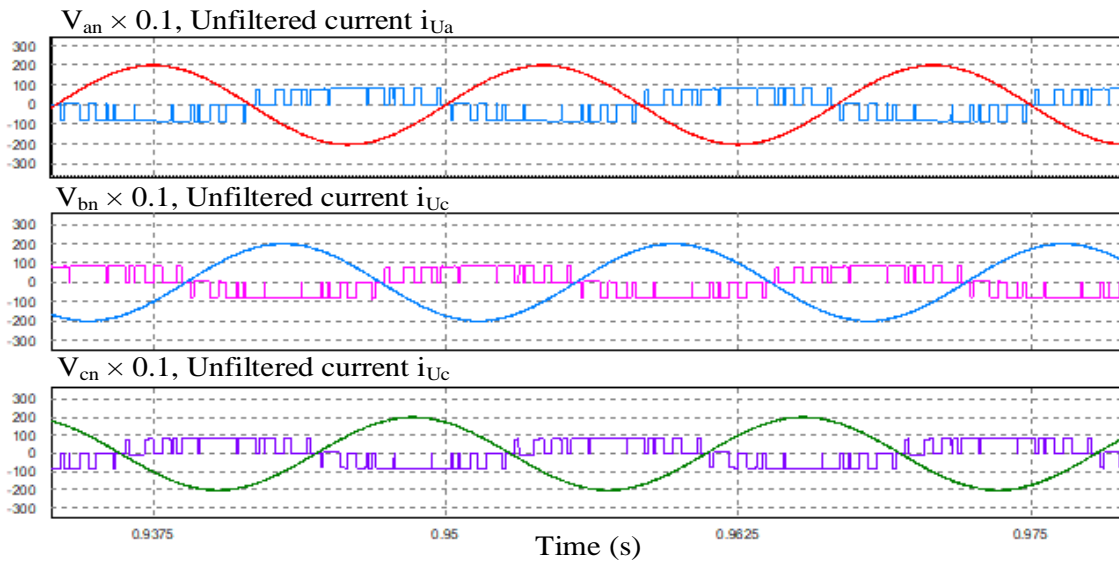


**Figure 4-17** (a) Simulation results for the proposed converter (Figure 4-5): (a) ( $V_{an}$ ,  $i_{ua}$ ), (b)  $I_A = I_{Q1} - I_{Q4}$ , (c)  $I_{Q1}$ , (d)  $I_{Q4}$ . Note  $V_{an}$  is scaled down by 10 for better resolution.

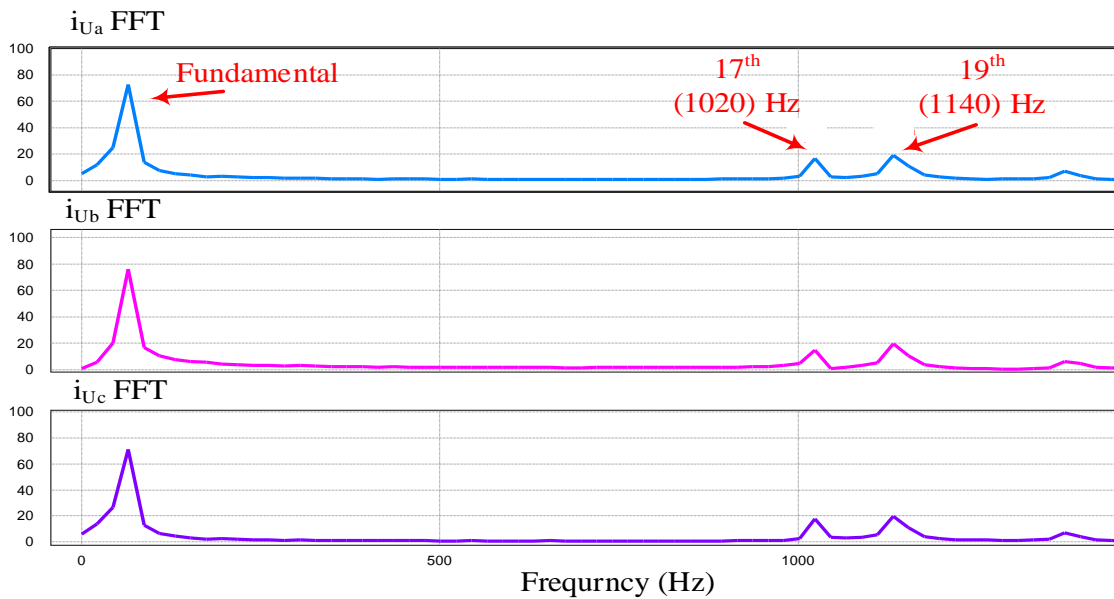


**Figure 4-18** (a) Simulation results for the proposed converter: (a) ( $V_{an}$ ,  $i_{ua}$ ), (b) ( $0.1 \times V_{PV}$ ,  $I_{PV}$ ), (c)  $V_{rec}$ , (d) free-wheeling case pulses for the three phase current source converter. Note  $V_{an}$  and  $V_{PV}$  are scaled down for better resolution.





**Figure 4-19 Simulation results for the proposed converter ( $V_{an}$ ,  $i_{Ua}$ ), ( $V_{bn}$ ,  $i_{Ub}$ ), ( $V_{cn}$ ,  $i_{Uc}$ ). Note the input voltages are scaled down by 10 for better resolution.**



**Figure 4-20 FFT analysis of the unfiltered input currents ( $i_{Ua}$ ,  $i_{Ub}$ ,  $i_{Uc}$ ). ( $5^{th}$ ,  $7^{th}$ ,  $11^{th}$ ,  $13^{th}$ ) harmonics have been eliminated. Note that the first dominant harmonic is the 17<sup>th</sup> (1020 Hz).**

#### 4.7. Experimental Results

Figure 4-21 shows a scale down 1 kW laboratory prototype that has been constructed and tested out to validate the proposed concept in Figure 4-5. Three phase voltage sensors are constructed in order to identify the zero-crossings of the three phase input voltages. The voltage sensor signals are connected to the ADC module of the Texas Instrument microcontroller kit type TMS320F28335 Delfino [41]. It uses to generate the gating signals of the AC-AC converter and CSC. Three sets of AC-AC converter have been built using Gan switch type (LMG3410) [69] from Texas Instrument to connect them to the high frequency transformer.

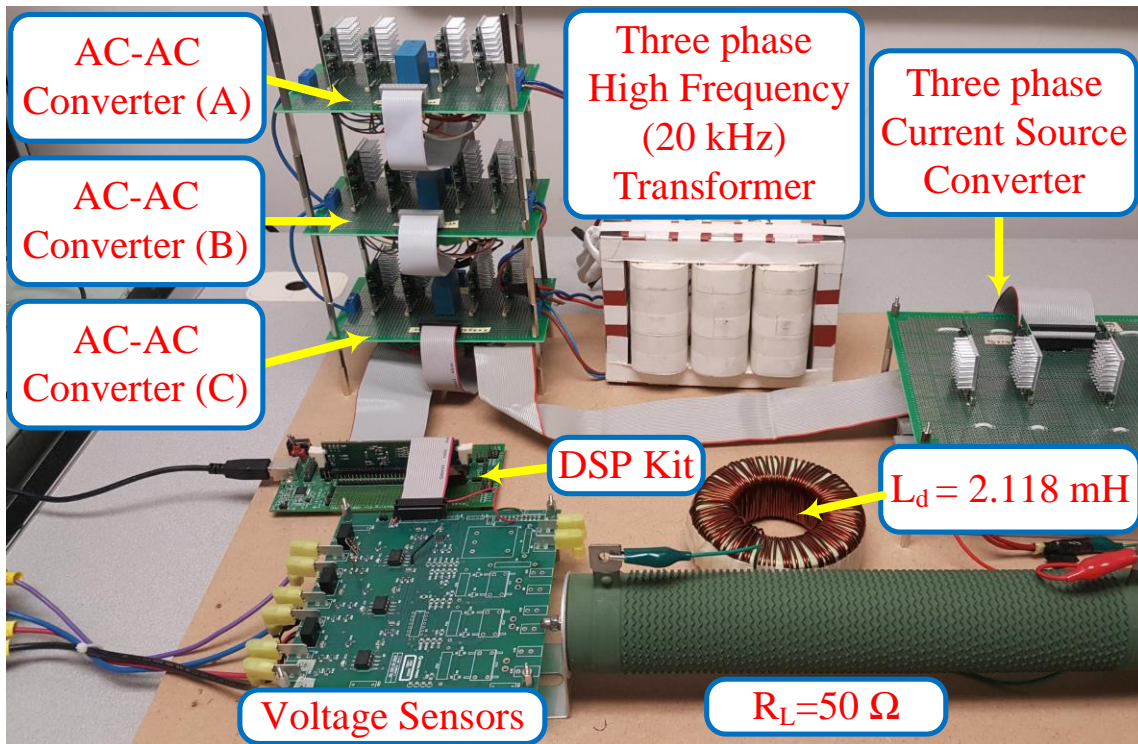
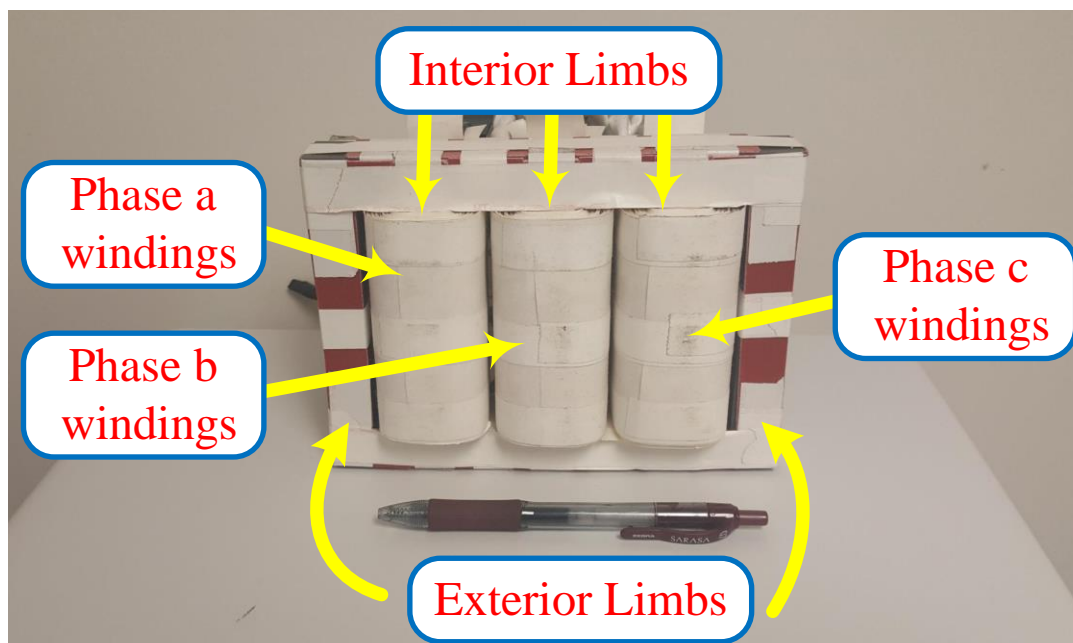


Figure 4-21 Experimental set up for the proposed topology in Figure 4-5.

The transformer has been connected in star to star with a unity turns ratio. It has five limbs in total, as shown in Figure 4-22. Three interior limbs use to carry the main flux lines, and two exterior limbs use to carry the unbalanced flux lines due to the switching to avoid any saturation case. Finally, the CSC has been constructed using Gan switch (LMG3410) [69] in series with the Silicon carbide diode type IXYS (fast recovery diode) [70]. The CSC is connected to the output of the high frequency transformer. Figure 4-23 shows phase “a” SHE signal that has been synchronized with the input utility line to neutral voltage  $V_{an}$ , and the phase “a” switching function AC-AC converter  $SW_{AC-AC}$ . In order to construct the gating signals for Leg<sub>A</sub> ( $Q_1, Q_4$ ), the SHE signal  $S_a$  has to be multiplied by  $SW_{AC-AC}$ . Figure 4-24 shows the gating signals of  $Q_1$ , and  $Q_4$ .



**Figure 4-22 Five limbs high frequency 20kHz transformer. Wire type Foil 22, 15 KVA, FERROXCUBE 3C94, core material used for the experimental set up.**

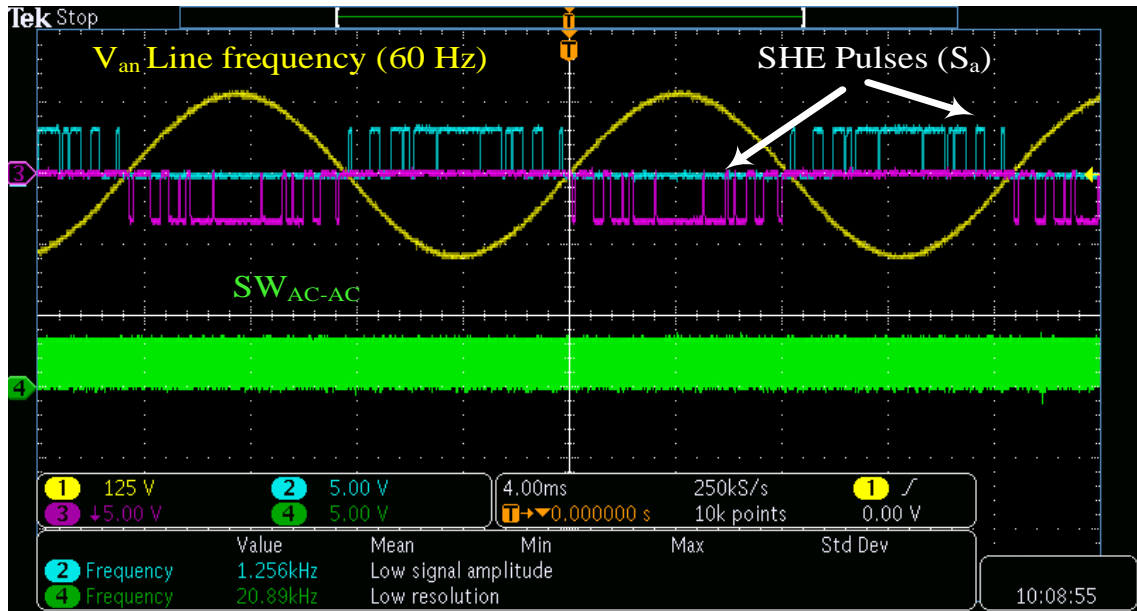


Figure 4-23 Experimental results of microcontroller signals. Ch1: Line to neutral input voltage  $V_{an}$ , (Ch2&Ch3): Phase “a” unipolar switching function  $S_a$ , Ch3: Phase “a” switching function for the AC-AC converter  $SW_{AC-AC}$ .

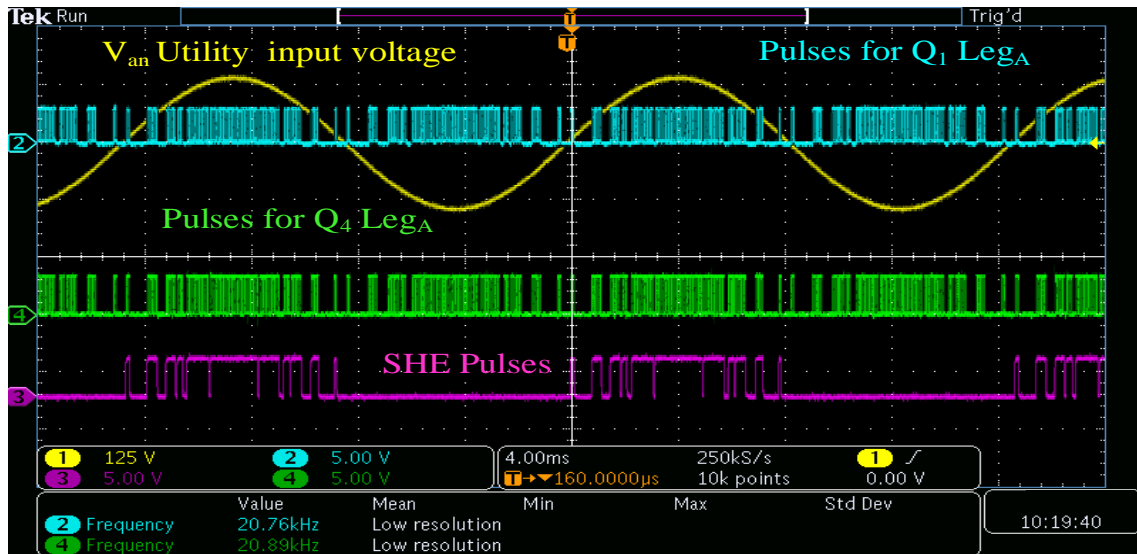


Figure 4-24 Experimental results of microcontroller signals. Ch1: Line to neutral input voltage  $V_{an}$ , Ch2: Pulses for  $Q_1$ , Ch4: Pulse for  $Q_4$ , Ch3: positive half cycle for unipolar switching function  $S_a$ .

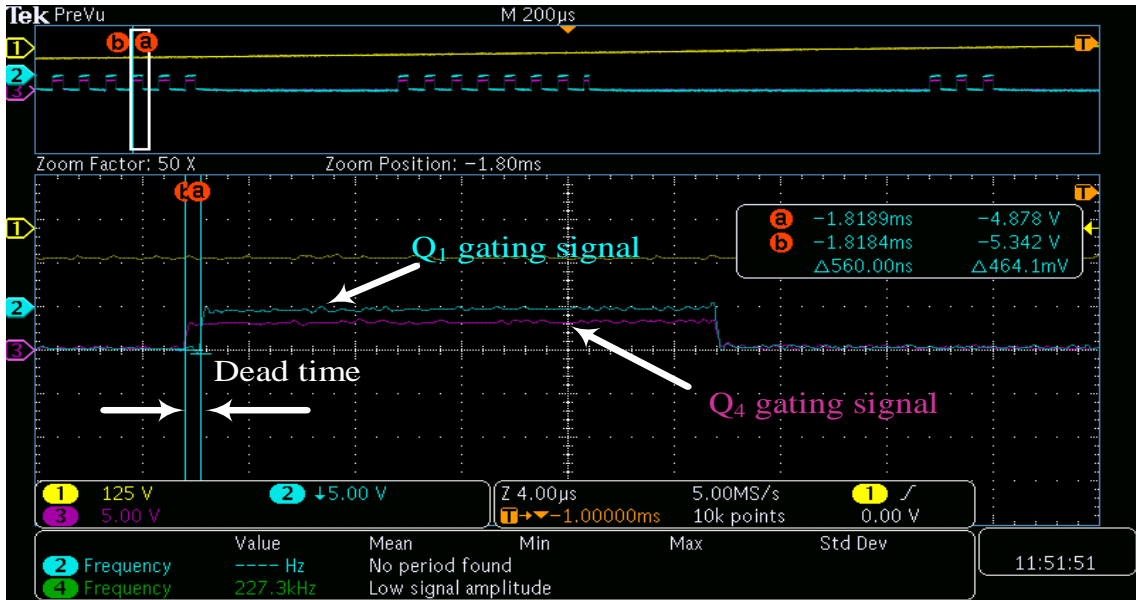


Figure 4-25 Experimental results for Physical dead time= (0.56 u sec). Ch.2: Gating signal for  $Q_1$ , Ch.3: Gating signal for  $Q_4$ .

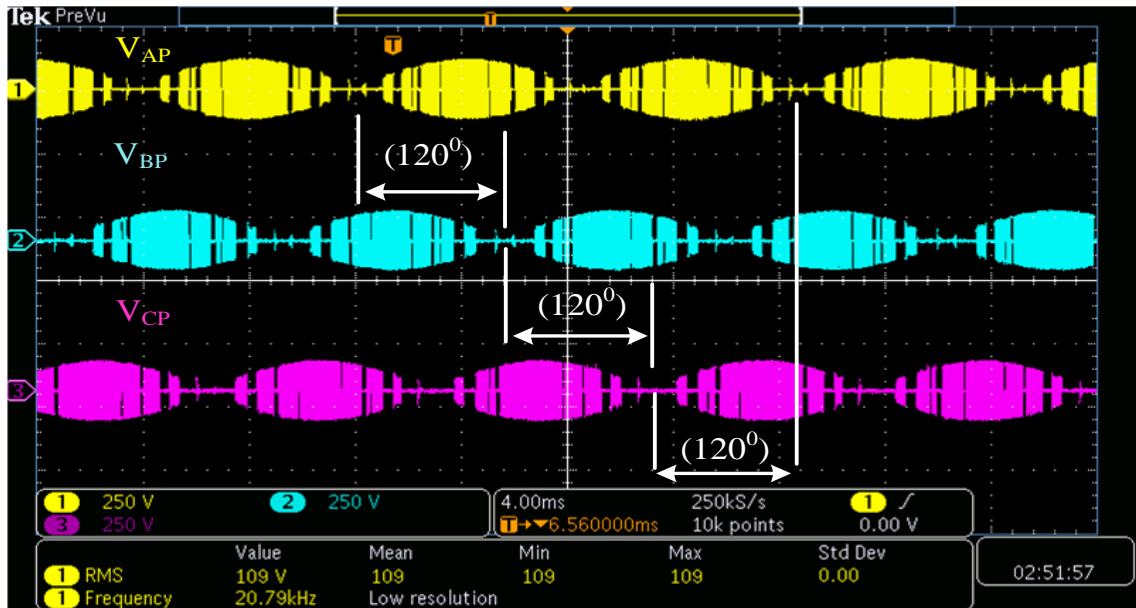


Figure 4-26 Experimental results for high frequency 20 kHz transformer input voltages. Ch.1:  $V_{AP}$ , Ch.2:  $V_{BP}$ , Ch.3:  $V_{CP}$ . Note that they are shifted by 120 degree for three phase operation.

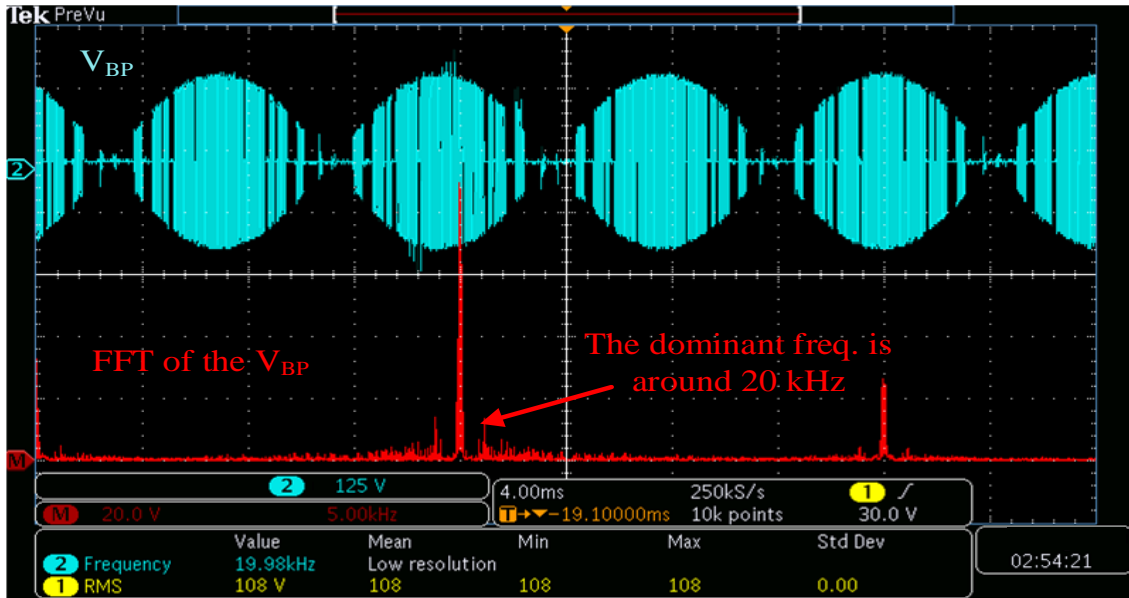


Figure 4-27 Experimental results. Ch.2: Phase “b” input primary voltage  $V_{BP}$ , Ch.M: Frequency spectrum analysis for  $V_{BP}$ . Note the dominant frequency is around 20 kHz.

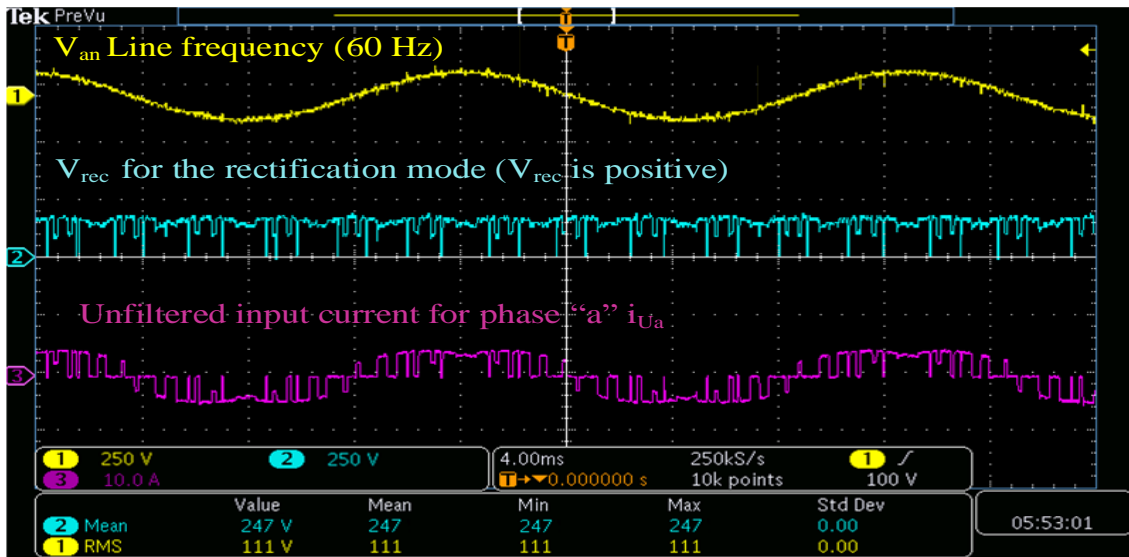
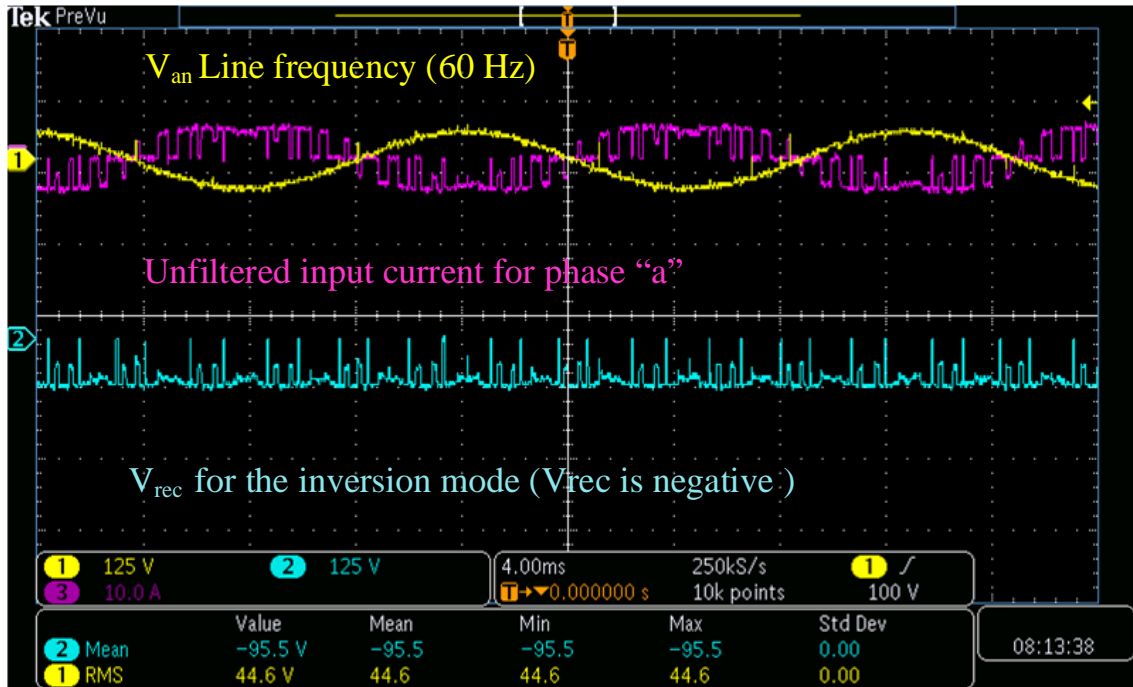


Figure 4-28 Experimental results for the rectification mode operation. Ch.1: Line to neutral input voltage  $V_{an}$ , Ch.2:  $V_{rec}$ , Ch. 3: Overall phase “a” unfiltered current  $i_{Ua}$ . Note that the power goes from the AC to the DC side.



**Figure 4-29** Experimental results for the inversion mode operation. Ch.1: Line to neutral input voltage  $V_{an}$ , Ch. 2:  $V_{rect}$ , Ch.3: Overall phase “a” unfiltered current  $i_{ua}$ ; Note that  $V_{rect}$  is negative and the power goes from the DC to the AC side.

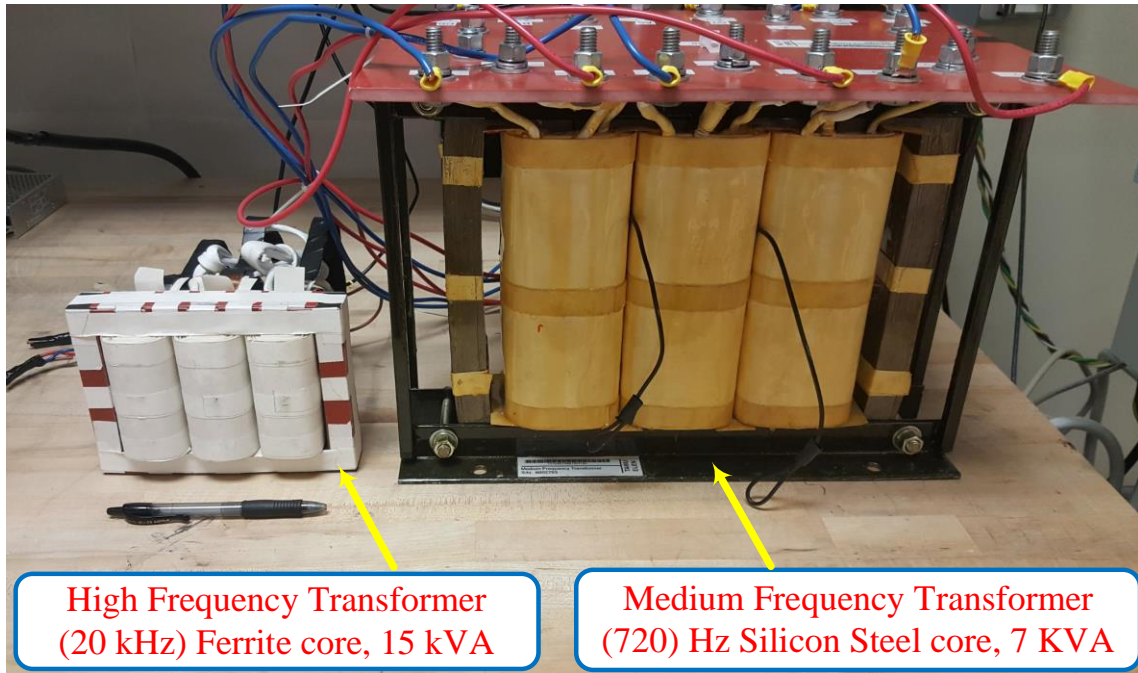
A physical dead time (0.56  $\mu$  sec) between  $Q_1$  and  $Q_4$  has been built, as shown in Figure 4-25, to avoid any short circuit case. It is clear that the experimental results and simulation results are identical. Figure 4-26 shows the output voltages of the AC-AC converter, which are the primary voltages of the high frequency transformer ( $V_{AP}$ ,  $V_{BP}$ ,  $V_{CP}$ ). They are shifted by 120 degree. Figure 3-27 shows the FFT analysis for the phase “b” high frequency transformer input voltage  $V_{BP}$ . Evidently, the dominant frequency of  $V_{BP}$  is around 20 kHz, confirming that the transformer works at high frequency. Figure 4-28 demonstrates the experimental results for the rectification mode of the proposed topology. In this mode, the CSC output voltage  $V_{rec}$  is positive, which means the power goes from the grid to the load confirming the rectification mode. For the inversion mode

operation, a DC voltage source ( $V_{DC} = 100 \text{ V}$ ) is connected at the output of the CSC to emulate the PV DC voltage source with an inductor  $L_d = 2.118 \text{ mH}$ . Figure 4-29 illustrates the experimental results for the inversion mode of the proposed topology. In this mode, the CSC output voltage  $V_{rec}$  is negative, which implies that the power goes from the DC side to the grid, confirming the inversion mode operation.

#### **4.8. Conclusion**

In this section, a high frequency integrated solid-state transformer SST for utility interface of solar PV / battery energy storage system has been proposed. The proposed approach demonstrates that a robust PWM current source converter operating at relatively low frequency with (5<sup>th</sup>, 7<sup>th</sup>, 11<sup>th</sup>, and 13<sup>th</sup>) harmonic elimination can be combined with a 20kHz integrated solid-state transformer to offer higher power density. Simulation results on 120 kW solar PV system employing 1500 V DC at various sun irradiance levels have been presented. A design example along with experimental results on a scale down 1 kW laboratory prototype has been shown to validate the concept. Figure 4-30 shows the difference between the medium frequency transformer 720 Hz that is used in the previous section and the high frequency transformer 20 kHz that is used in this section. The Figure demonstrates the difference in terms of size/weight, and the volt-ampere rating.





**Figure 4-30 Medium frequency transformer 720 Hz (M19 Silicon steel core material, 7 KVA), High Frequency transformer 20 kHz (FERROXCUBE 3C94 Ferrite core material, 15 KVA).**

## 5. SUMMARY

### 5.1. Conclusion

This dissertation mainly introduces approaches to interface renewable energy resources. e.g. (solar/ wind turbine) to a utility grid using a medium or high frequency integrated solid-state transformer. A brief introduction of high-power semiconductor switching devices is presented, focusing on the silicon control rectifier SCR characteristics. Then the section discussed the AC and DC collection grid followed by a large-scale PV plant. The concept of power density for a power electronics converter is discussed followed by how to improve the power density.

In section 2, a medium voltage DC collection grid for large-scale PV plant using 12-pulse SCR converter and line frequency transformer is discussed. A new hybrid step-up DC-DC converter is proposed to boost the 1.5 kV DC PV plant to the medium voltage scale 6 kV. The mathematical analysis, and simulation results with design example are discussed to validate the presented concept.

Section 3 presents a unique concept to improve the power density of the medium voltage DC collection grid using a 12-pulse line commutated SCR converter and medium frequency (720 Hz) integrated solid-state transformer. The mathematical analysis, including the phasor diagram for the medium frequency zig-zag phase-shift transformer, are discussed. The aim of this section is to have the SST operate at the medium frequency to reduce the transformer size/weight. A high-quality utility input current is achieved with the cancellation of 5<sup>th</sup> and 7<sup>th</sup> harmonic currents. The proposed approach is robust, has

higher power density, and is simple to control with an integrated solid-state transformer. Detailed design example 150 kW PV power plant, simulation results, experimental results for a scale down laboratory type 1kW system are discussed to validate the concept. Moreover, to improve the efficiency, reliability of the proposed concept, a new open delta phase-shift medium frequency solid-state transformer is presented. The two presented concepts show that they have the same quality as the conventional 12-pulse SCR converter. However, they replace the bulky line frequency transformer by a medium frequency one to improve the power density.

Section 4 presents a relatively new concept of current source converter using a selective harmonics elimination pulse width modulation along with a high frequency (20 kHz) integrated solid-state transformer. The results show that this topology has some advantages; a very good input current quality, bidirectional power flow, more power density. Detailed analysis, simulation results are discussed. In addition, a scale down experimental prototype is constructed to validate the presented concept.

To conclude, this dissertation presented several approaches employing a higher frequency transformer to interface the large-scale renewable energy resources to a utility grid. The simulation and scale down experimental results approve that the presented approaches have the same quality as the conventional approaches. However, the presented approaches replaced the bulky line frequency transformer with a higher frequency transformer, which implies higher power density is achieved and more reliable due to the elimination of the large DC-link (electrolytic capacitors). All the proposed approaches have the ability of bidirectional power flow, and the output voltage can be easily regulated.

## 5.2. Future Works

The presented approaches in this dissertation have several advantages regarding improving the power density and increasing the reliability of the proposed topologies. Therefore, further research opportunities can be investigated.

1. For the medium voltage DC collection grid using SCR converter and medium frequency (720 Hz) solid-state transformer:

- Soft-switching techniques may be applied to the medium frequency AC-AC converter to increase the efficiency further of the system.
- More than 12-pulse SCR converter with medium frequency transformer can be configured and constructed to achieve better input current quality.
- Silicon carbide SCR that manufactured by GeneSic company [71] could be considered for further investigation because using wide bandgap devices would benefit the system efficiency and allow the transformer to work at higher frequency. However, the cost factor should be considered.
- The medium frequency core material could be optimized to have less leakage inductance. Another core material can be considered. Amorphous can be investigated and tested to figure out which core material would give better performance to this approach. However, the cost factor of these materials should be taken into account.
- An economical and efficiency investigation that involves the system cable's length, size, medium frequency voltages, PV plant structure, and labor cost should be considered for future study.

2. For the current source converter that uses a high frequency (20 kHz) solid-state transformer:

- A soft-switching operation can be explored to improve system efficiency further.
- Another investigation area is the series of stack numbers for the AC-AC converters should be optimized to allow the topology to work with the medium voltage scale.
- The open delta concept can be constructed to increase system reliability and efficiency.
- For simplicity, a unidirectional AC-AC converter (bridge diode followed by bridge switches) can be used. However, this will lose the capability of bidirectional power flow.

## REFERENCES

- [1] B. Wu, *High-Power Converters and AC Drives*. New York/Piscataway, NJ: Wiley/IEEE Press, 2006.
- [2] N. Mohan, T. M. Undeland, and W. P. Robbins, *Power Electronics: Converters, Applications, and Design*. United States: John Wiley & Sons, Inc., 1989.
- [3] Dragan Jovcic and Khalid Ahmed, *High-Voltage Direct-Current Transmission Converter System and DC Grids*, John Wiley & Sons Ltd, 2015.
- [4] D. W. Hart, *Power Electronics*. New York, NY: McGraw-Hill, 2011.
- [5] W. Hu, B. Wu, N. R. Zargari and Z. Cheng, "A Novel Self-Powered Supply for GCT Gate Drivers," in *IEEE Transactions on Power Electronics*, vol. 24, no. 4, pp. 1093-1099, April 2009.
- [6] J. Afsharian, B. Wu and N. Zargari, "Self-powered supplies for SCR, IGBT, GTO and IGCT devices: A review of the state of the art," *2009 Canadian Conference on Electrical and Computer Engineering*, St. John's, NL, 2009, pp. 920-925.
- [7] M. R. Islam, A. M. Mahfuz-Ur-Rahman, M. M. Islam, Y. G. Guo and J. G. Zhu, "Modular Medium-Voltage Grid-Connected Converter With Improved Switching Techniques for Solar Photovoltaic Systems," in *IEEE Transactions on Industrial Electronics*, vol. 64, no. 11, pp. 8887-8896, Nov. 2017.
- [8] B. Hafez, P. Enjeti and S. Ahmed, "A robust controller for medium voltage AC collection grid for large scale Photovoltaic plants based on medium frequency transformers," *2016 IEEE Applied Power Electronics Conference and Exposition (APEC)*, Long Beach, CA, 2016, pp. 936-942.
- [9] H. Choi, M. Ciobotaru, M. Jang and V. G. Agelidis, "Performance of Medium-Voltage DC-Bus PV System Architecture Utilizing High-Gain DC-DC Converter," in *IEEE Transactions on Sustainable Energy*, vol. 6, no. 2, pp. 464-473, April 2015.
- [10] Advances in Utility-Scale PV Plants: Key Lessons Learned. 2017. First Solar [Online]. Available: <http://sites.ieee.org/scv-photovoltaic/files/slides/20171101-Advances-in-Utility-Scale-PV-Plants-Key-Lessons-Learned.pdf>

- [11] E. Gkoutioudi, P. Bakas and A. Marinopoulos, "Comparison of PV systems with maximum DC voltage 1000V and 1500V," *2013 IEEE 39th Photovoltaic Specialists Conference (PVSC)*, Tampa, FL, 2013, pp. 2873-2878.
- [12] E. Serban, M. Ordonez and C. Pondiche, "DC-Bus Voltage Range Extension in 1500 V Photovoltaic Inverters," in *IEEE Journal of Emerging and Selected Topics in Power Electronics*, vol. 3, no. 4, pp. 901-917, Dec. 2015.
- [13] The state of medium voltage DC architectures for utility scale PV. 2018.  
[Online]. Available: <https://www.pv-tech.org/editors-blog/the-state-of-medium-voltage-dc-architectures-for-utility-scale-pv>.
- [14] D. R. B. Ben Jose, N. A. Gounden and J. Ravishankar, "Simple power electronic controller for photovoltaic fed grid-tied systems using line commutated inverter with fixed firing angle," in *IET Power Electronics*, vol. 7, no. 6, pp. 1424-1434, June 2014.
- [15] Price unit/ MWh for both wind and solar according to Lazard Levelized cos of energy analysis [Online]. Available:  
<https://www.lazard.com/perspective/levelized-cost-of-energy-and-levelized-cost-of-storage-2018/>
- [16] R. M. Burkart and J. W. Kolar, "Comparative evaluation of SiC and Si PV inverter systems based on power density and efficiency as indicators of initial cost and operating revenue," in *2013 IEEE 14th Workshop on Control and Modeling for Power Electronics (COMPEL)*, Salt Lake City, UT, 2013, pp. 1-6.
- [17] G. Ortiz, J. Biela, and J. W. Kolar, "Optimized design of medium frequency transformers with high isolation requirements," in *IECON 2010 - 36th Annual Conference on IEEE Industrial Electronics Society, 2010*, pp. 631-638.
- [18] B. Hafez, H. S. Krishnamoorthy, P. Enjeti, U. Borup, and S. Ahmed, "Medium voltage AC collection grid for large scale photovoltaic plants based on medium frequency transformers," in *2014 IEEE Energy Conversion Congress and Exposition (ECCE)*, Pittsburgh, PA, 2014, pp. 5304-5311.
- [19] B. Hafez, P. Enjeti and S. Ahmed, "A robust controller for medium voltage AC collection grid for large scale Photovoltaic plants based on medium frequency transformers," *2016 IEEE Applied Power Electronics Conference and Exposition (APEC)*, Long Beach, CA, 2016, pp. 936-942.

- [20] K. Musasa, N. I. Nwulu, M. N. Gitau and R. C. Bansal, "Review on DC collection grids for offshore wind farms with high-voltage DC transmission system," in *IET Power Electronics*, vol. 10, no. 15, pp. 2104-2115, 12 15 2017.
- [21] A. M. El-Tamaly, P. N. Enjeti and H. H. El-Tamaly, "An improved approach to reduce harmonics in the utility interface of wind, photovoltaic and fuel cell power systems," *APEC 2000. Fifteenth Annual IEEE Applied Power Electronics Conference and Exposition (Cat. No.00CH37058)*, New Orleans, LA, USA, 2000, pp. 1059-1065 vol.2.
- [22] Z. Chen, "Compensation schemes for a SCR converter in variable speed wind power systems," in *IEEE Transactions on Power Delivery*, vol. 19, no. 2, pp. 813-821, April 2004.
- [23] M. H. Rashid, *Power electronics handbook: devices, circuits and applications*: Academic Press, 2010.
- [24] R. W. Erickson, D Maksimovic, *Fundamental of power electronics*, second edition: Kluwer Academic/ plenum publishes, New York, 2001.
- [25] Toshiba. (April 20). Toshiba MV Drives. Available: [http://www.toshiba.com/ind/data/tag\\_files/MTX\\_NEMA\\_3R\\_MV\\_Brochure\\_3002.pdf](http://www.toshiba.com/ind/data/tag_files/MTX_NEMA_3R_MV_Brochure_3002.pdf)
- [26] Global Energy Transformation Available: [https://www.irena.org//media/Files/IRENA/Agency/Publication/2018/Apr/IRENA\\_Report\\_GET\\_2018.pdf](https://www.irena.org//media/Files/IRENA/Agency/Publication/2018/Apr/IRENA_Report_GET_2018.pdf)
- [27] L.L. Brighenti, R.T. Hock, L.G. Kremer, A.L. Batschauer and M.Mezaroba, "Using MPPT in multi-pulse converters for photovoltaic cogeneration," *IEEE Energy Conversion Congress and Exposition (ECCE), Pittsburg, PA*, 2014, pp.24-31.
- [28] H. Krishnamoorthy, M. Daniel, J. Ramos-Ruiz, P. Enjeti, L. Liu and E. Aeloiza, "Isolated AC–DC Converter Using Medium Frequency Transformer for Off-Shore Wind Turbine DC Collection Grid," in *IEEE Transactions on Industrial Electronics*, vol. 64, no. 11, pp. 8939-8947, Nov. 2017.
- [29] Jaehong Hahn and P. N. Enjeti, "A wide input range active multi-pulse three-phase rectifier for utility interface of power electronic converters," *Conference Record of the 2002 IEEE Industry Applications Conference. 37th IAS Annual Meeting (Cat. No.02CH37344), Pittsburgh, PA, USA, 2002*, pp. 2514-2519 vol.4.



- [30] O. asynczuk, "Modeling and dynamic performance of a line- commutated photovoltaic inverter system," in *IEEE Transactions on Energy Conversion*, vol. 4, no. 3, pp. 337-343, Sept. 1989.
- [31] E. Veilleux and P. W. Lehn, "Interconnection of Direct-Drive Wind Turbines Using a Series-Connected DC Grid," in *IEEE Transactions on Sustainable Energy*, vol. 5, no. 1, pp. 139-147, Jan. 2014.
- [32] Nishikata, S., Tatsuta, F.: 'A new interconnecting method for wind turbine/ generators in a wind farm and basic performances of the integrated system', *IEEE Trans. Ind. Electron.*, 2010, 57, (2), pp. 468–475
- [33] T. H. Nguyen, Q. A. Le and D. Lee, "A novel HVDC-link based on hybrid voltage-source converters," *2015 IEEE Energy Conversion Congress and Exposition (ECCE)*, Montreal, QC, 2015, pp. 3338-3343.
- [34] L. L. Brighenti, L. G. Kremer, A. L. Batschauer and M. Mezaroba, "Phase-controlled inverters associated to a multi-pulse autotransformer applied to photovoltaic cogeneration," *2013 Brazilian Power Electronics Conference*, Gramado, 2013, pp. 501-508.
- [35] L. L. Brighenti, R. T. Hock, L. G. Kremer, A. L. Batschauer and M. Mezaroba, "Using MPPT in multi-pulse converters for photovoltaic cogeneration," *2014 IEEE Energy Conversion Congress and Exposition (ECCE)*, Pittsburgh, PA, 2014, pp. 24-31.
- [36] S. Sabry, E. I. Pool-Mazun and P. Enjeti, "A Medium Voltage DC Collection Grid for Large Scale PV Power Plant with SCR Converter and Integrated Solid-State Transformer (SST)," *2019 IEEE Energy Conversion Congress and Exposition (ECCE)*, Baltimore, MD, USA, 2019, pp. 5824-5831,
- [37] WESCODE Fast Turn-off Thyristor type PO128SH10 to PO128SH12 Datasheet Specification. Available: <http://www.westcode.com/p0273sc12x.pdf>
- [38] A. H. Wijenayake et al., "Next-generation MVDC architecture based on 6.5 kV / 200 A, 12.5 mΩ SiC H-bridge and 10 kV / 240 A, 20 mΩ SiC dual power modules," *2017 IEEE Electric Ship Technologies Symposium (ESTS)*, Arlington, VA, 2017, pp. 598-604.
- [39] Silicon control rectifier switch SCR for the experimental type 2N6399 Datasheet Specification. Available: <http://edg.uchicago.edu/~bogdan/pulsar/doc/parts/2n6394.pdf>

- [40] IGBT for the prototype AC-AC converter type IXXH50N60C3D1-ND Datasheet Specification. Available: [https://www.littelfuse.com/~media/electronics/datasheets/discrete\\_igbts/littelfuse\\_discrete\\_igbts\\_xpt\\_ixxh50n60c3d1\\_datasheet.pdf.pdf](https://www.littelfuse.com/~media/electronics/datasheets/discrete_igbts/littelfuse_discrete_igbts_xpt_ixxh50n60c3d1_datasheet.pdf.pdf)
- [41] T. Instruments. (2012), TMS320F28335, TMS320F28334, TMS320F28332, TMS320F28235, TMS320F28234, TMS320F28232 Digital Signal Controllers (DSCs) Data Manual [Online]. Available: <http://www.ti.com/lit/ds/symlink/tms320f28335.pdf>
- [42] PVTECH [Online]. Available: <https://www.pv-tech.org/editors-blog/the-state-of-medium-voltage-dc-architectures-for-utility-scale-pv>.
- [43] M. Glab, Z. Krzeminski and M. Wlas, "PWM current source inverter with IGBT transistors and multiscalar model control system," *2005 European Conference on Power Electronics and Applications*, Dresden, 2005, pp. 10 pp.-P.10
- [44] J. Millán, P. Godignon, X. Perpiñà, A. Pérez-Tomás and J. Rebollo, "A Survey of Wide Bandgap Power Semiconductor Devices," in *IEEE Transactions on Power Electronics*, vol. 29, no. 5, pp. 2155-2163, May 2014.
- [45] B. Wu, J. Pontt, J. Rodriguez, S. Bernet and S. Kouro, "Current-Source Converter and Cycloconverter Topologies for Industrial Medium-Voltage Drives," in *IEEE Transactions on Industrial Electronics*, vol. 55, no. 7, pp. 2786-2797, July 2008.
- [46] Bang Sup Lee, P. N. Enjeti and I. J. Pitel, "An optimized active interphase transformer for auto-connected 12-pulse rectifiers results in clean input power," *Proceedings of APEC 97 - Applied Power Electronics Conference*, Atlanta, GA, USA, 1997, pp. 666-671 vol.2.
- [47] P. N. Enjeti, P. D. Ziogas, and J. F. Lindsay, "Programmed PWM techniques to eliminate harmonics: a critical evaluation," *IEEE Transactions on Industry Applications*, vol. 26, pp. 302-316, 1990.
- [48] S. Sabry and P. Enjeti, "High Frequency Integrated Solid State Transformer (SST) for Utility Interface of Solar PV / Battery Energy Storage Systems," *2020 IEEE Applied Power Electronics Conference and Exposition (APEC)*, New Orleans, LA, USA, 2020, pp. 546-553,
- [49] P. N. Enjeti, P. D. Ziogas, and J. F. Lindsay, "A current source PWM inverter with instantaneous current control capability," *IEEE Transactions on Industry Applications*, vol. 27, pp. 582-588, 1991.

- [50] P. N. Enjeti, P. D. Ziogas, J. F. Lindsay, and M. H. Rashid, "A new PWM speed control system for high-performance AC motor drives," *IEEE Transactions on Industrial Electronics*, vol. 37, pp. 143-151, 1990.
- [51] J. Ge, Z. Zhao, L. Yuan and T. Lu, "Energy Feed-Forward and Direct Feed-Forward Control for Solid-State Transformer," in *IEEE Transactions on Power Electronics*, vol. 30, no. 8, pp. 4042-4047, Aug. 2015.
- [52] H. Chen and D. Divan, "Design of a 10-kV·A Soft-Switching Solid-State Transformer (S4T)," in *IEEE Transactions on Power Electronics*, vol. 33, no. 7, pp. 5724-5738, July 2018.
- [53] M. Kang, P. N. Enjeti and I. J. Pitel, "Analysis and design of electronic transformers for electric power distribution system," in *IEEE Transactions on Power Electronics*, vol. 14, no. 6, pp. 1133-1141, Nov. 1999.
- [54] Huber, Jonas E. and Johann Walter Kolar. "Solid-State Transformers: On the Origins and Evolution of Key Concepts." *IEEE Industrial Electronics Magazine* 10 (2016): 19-28.
- [55] J. E. Huber and J. W. Kolar, "Volume/weight/cost comparison of a 1MVA 10 kV/400 V solid-state against a conventional low-frequency distribution transformer," *2014 IEEE Energy Conversion Congress and Exposition (ECCE)*, Pittsburgh, PA, 2014, pp. 4545-4552.
- [56] D. Wang *et al.*, "A 10-kV/400-V 500-kVA Electronic Power Transformer," in *IEEE Transactions on Industrial Electronics*, vol. 63, no. 11, pp. 6653-6663, Nov. 2016.
- [57] C. Zhao *et al.*, "Power Electronic Traction Transformer—Medium Voltage Prototype," in *IEEE Transactions on Industrial Electronics*, vol. 61, no. 7, pp. 3257-3268, July 2014.
- [58] M. Kang, P. N. Enjeti and I. J. Pitel, "Analysis and design of electronic transformers for electric power distribution system," in *IEEE Transactions on Power Electronics*, vol. 14, no. 6, pp. 1133-1141, Nov. 1999.
- [59] Fan Zhang *et al.*, "Design and demonstration of a SiC-based 800-V/10-kV 1-MW solid-state transformer for grid-connected photovoltaic systems," *2017 IEEE 3rd International Future Energy Electronics Conference and ECCE Asia (IFEEC 2017 - ECCE Asia)*, Kaohsiung, 2017, pp. 1987-1990.
- [60] T. M. Parreiras, A. P. Machado, F. V. Amaral, G. C. Lobato, J. A. S. Brito and B. C. Filho, "Forward Dual-Active-Bridge Solid-State Transformer for a SiC-Based

- Cascaded Multilevel Converter Cell in Solar Applications," in *IEEE Transactions on Industry Applications*, vol. 54, no. 6, pp. 6353-6363, Nov.-Dec. 2018.
- [61] J. E. Huber, D. Rothmund, L. Wang and J. W. Kolar, "Full-ZVS modulation for all-SiC ISOP-type isolated front end (IFE) solid-state transformer," *2016 IEEE Energy Conversion Congress and Exposition (ECCE)*, Milwaukee, WI, 2016, pp. 1-8.
- [62] X. She, A. Q. Huang and R. Burgos, "Review of Solid-State Transformer Technologies and Their Application in Power Distribution Systems," in *IEEE Journal of Emerging and Selected Topics in Power Electronics*, vol. 1, no. 3, pp. 186-198, Sept. 2013.
- [63] G. Ortiz, M. Leibl, J. W. Kolar, and O. Apeldoorn, "Medium frequency transformers for solid-state-transformer applications: Design and experimental verification," in *2013 IEEE 10th International Conference on Power Electronics and Drive Systems (PEDS)*, pp. 1285-1290, 2013
- [64] W. M. Colonel and T. Mclyman, *Transformer and Inductor Design Handbook* vol. 3rd ed. Boca Raton, FL USA: CRC Press, 2004.
- [65] A. Van den Bossche, and V. Cekov Valchev "*Soft Magnetic Materials*," in *Inductors and Transformers for Power Electronics*, ed: CRC Press, 2005.
- [66] C. Leung, S. Dutta, S. Baek and S. Bhattacharya, "Design considerations of high voltage and high frequency three phase transformer for Solid State Transformer application," *2010 IEEE Energy Conversion Congress and Exposition*, Atlanta, GA, 2010, pp. 1551-1558.
- [67] Solarex [Online]. Available: <http://www.firstsolar.com/-/media/First-Solar/Technical-Documents/Series-4-Datasheets/Series-4V2-Datasheet.ashx>
- [68] First solar series 4TM PV module [Online]. Available: <http://www.firstsolar.com/-/media/First-Solar/Technical-Documents/Series-4-Datasheets/Series-4V2-Datasheet.ashx>
- [69] Texas Instrument LMG3410-HB-EVM half-bridge break out board EVM [Online]. Available: <http://www.ti.com/lit/ug/snou140a/snou140a.pdf>
- [70] IXYS three phase rectifier bridge with fast recovery epitaxial diodes [Online]. Available: <http://ixapps.ixys.com/DataSheet/1367.pdf>
- [71] GeneSic ultra-high voltage Silicon carbide Thyristor [Online]. Available:

[https://www.sandia.gov/ess-ssl/docs/other/Ultra-HiThyristor\\_SAND2011-2151P.pdf](https://www.sandia.gov/ess-ssl/docs/other/Ultra-HiThyristor_SAND2011-2151P.pdf)